Geodätisch-geophysikalische Arbeiten in der Schweiz

**Einhundertvierter Band
Volume 104**

GNSS receiver synchronisation and antenna calibration

Daniel Willi

2020

VORWORT

Die Cube-Satellitenmission CubETH des Instituts für Geodäsie und Photogrammetrie (IGP) der ETH Zürich in Zusammenarbeit mit verschiedenen Partnern aus Akademie und Industrie hat das Ziel, eine GNSS-Empfänger-Nutzlast im Weltraum zu fliegen, die aus fünf Antennen (vier auf der Zenitseite und eine seitwärtsgerichtet) besteht, wobei jede Antenne mit zwei kleinen Ein-Frequenz-Empfängern der Schweizer Firma u-blox verbunden ist. Der Cube-Satellit mit einer Grösse von 10 cm auf 10 cm auf 10 cm wurde entwickelt, um sowohl die Satellitenbahn als auch die -orientierung mit der GNSS-Nutzlast zu bestimmen. Da die drei Basislinien zwischen den vier GNSS-Antennen auf der Zenitseite des kleinen Satelliten extrem kurz sind, wird die Lagebestimmung zu einer richtigen Herausforderung. Diese Schwierigkeit wird noch vergrössert durch den Umstand, dass die durch die COTS GNSS-Empfänger aufgezeichneten Beobachtungen um bis zu 0.5 ms in der Zeit versetzt sein können, während der Satellit sich mit einer Geschwindigkeit von typischerweise 7 km/s bewegt. Eine weitere Fehlerquelle sind die grossen GNSS-Phasenzentrumsvariationen, die bei so kleinen Patch-Antennen zu erwarten sind und die Lagebestimmung stark verschlechtern.

Daniel Willi widmete sich sehr erfolgreich all diesen Problemen, indem er zuerst ein sehr detailliertes, genaues Korrekturmodell für die nicht-synchronisierten Beobachtungen erarbeitete und dieses Modell dann mit Simulationsrechnungen und mit einem Industrieroboter testete. Er erreichte dabei eine beachtliche Genauigkeit der Lagebestimmung von ein paar Grad mit den extrem kurzen Basislinien von 5-8 cm. Um die Bestimmung der Ausrichtung des Satelliten mit den sehr kurzen Basislinien weiter zu verbessern, war es notwendig, die Phasenzentrumsoffsets und -variationen der kleinen GNSS Patch-Antennen genau zu kalibrieren. Diese Kalibrieraktivitäten haben den Fokus in Richtung der Kalibrierung von GNSS-Empfängerantennenphasenzentren im Allgemeinen verschoben. Die Kalibrierung der Antennenphasenzentren der wichtigsten Antennentypen für alle GNSS und alle verfügbaren Frequenzen ist eine absolute Notwendigkeit für hochgenaue GNSS-Anwendungen, die Multi-GNSS-Antennen und -empfänger einsetzen. Insbesondere die Realisierung eines extrem stabilen und genauen Referenzrahmens als metrologische Basis für äusserst anspruchsvolle Anwendungen wie etwa das Erfassen des Meeresspiegelanstiegs, erfordert lange Zeitserien von mit höchster Genauigkeit und Zuverlässigkeit berechneten GNSS-Stationskoordinaten. Da kein konsistenter Satz von Phasenzentrumskalibrierungen für alle wesentlichen geodätischen Antennentypen verfügbar war, stellte sich Daniel Willi dieser schwierigen Herausforderung und konzentrierte sich auf die absolute Kalibrierung von GNSS-Antennenphasenzentrumsvariationen im Allgemeinen. In nur gerade zwei Jahren entwickelte Daniel Willi von Grund auf ein komplettes und völlig automatisiertes System für die Kalibrierung von GNSS-Antennen, wobei er dazu einen Industrieroboter, eine neue Datenanalysemethode mit Dreifach-Differenzen zur Unterdrückung von Mehrwegeffekten und eine optimierte Folge von Rotationen für die Orientierung der zu kalibrierenden Antenne verwendete. Zudem musste Daniel Willi auch den Industrieroboter selbst kalibrieren. Dies geschah mit Hilfe eines kinematischen Modells und einer geschickten Parametrisierung der Robotergeometrie und war eine Herausforderung an sich. Zusammengefasst hat Daniel Willi damit ein sehr effizientes System für die GNSS-Antennenkalibrierung entwickelt. Die hohe Genauigkeit dieses Systems wurde bereits durch Vergleiche mit anderen Kalibriermethoden und mit Resultaten auf kurzen Basislinien, die zusammen mit swisstopo durchgeführt wurden, eindrücklich demonstriert. Die SGK dankt sowohl dem Autor für den wertvollen Beitrag als auch der Schweizerischen Akademie für Naturwissenschaften (SCNAT) für die Übernahme der Druckkosten.

Prof. Dr. M. Rothacher

Institut für Geodäsie und Photogrammetrie   ETH Zürich
ETH Zürich   Präsident der SGK

PREFACE

La mission satellitaire CubETH, de l'institut de géodésie et photogrammétrie (IGP) de l'école polytechnique fédérale de Zurich, est un projet collaboratif de divers partenaires industriels et académiques et qui a pour but la mise en orbite terrestre d'un système global de navigation par satellite (GNSS) consistant en cinq antennes (quatre dirigées en direction du zénith et une dirigée sur le côté) ; chacune d'elles étant connectée à deux récepteurs miniatures à une fréquence, développés par la compagnie suisse u-blox. Le satellite porteur de la charge utile GNSS est de forme cubique de 10 cm de côté et a été développé pour accomplir des déterminations d'orbites et d'attitudes. Du fait que les trois lignes de base entre les quatre antennes GNSS de la face zénithale du petit satellite sont extrêmement courtes, la détermination de l'attitude est un réel défi. Cette difficulté est amplifiée par le fait que les observations collectées par les récepteurs GNSS à bas coût peuvent êtres décalées dans le temps jusqu'à 0.5 millisecondes alors que le satellite se déplace à une vitesse de 7 km/s. D'autres sources d'erreurs sont les variations des centres de phase auxquelles l'on peut s'attendre pour des antennes miniaturisées telles que celles utilisées. Ces variations dégradent significativement les valeurs des estimations d'attitudes. Monsieur Willi a résolu avec succès ces problèmes en développant un modèle très précis et très détaillé pour les observations asynchrones puis en testant ce modèle, en se basant sur des simulations et sur des donnée obtenues à l'aide d'un robot industriel, et a atteint une précision remarquable de quelques degrés sur une ligne de base de 5 à 8 centimètres. Afin d'améliorer les résultats d'attitude sur une ligne de base si courte, les variations des centres de phase des antennes miniaturisées ont dû être calibrées. Ces activités de calibrations ont déplacé la focalisation de la thèse de doctorat de Monsieur Willi, vers un but plus général qui est la calibration des variations des centres de phase des antennes GNSS. La calibration des variations des centres de phase des principaux modèles d'antennes pour toutes les fréquences et toutes les constellations GNSS est une nécessité absolue pour l'obtention d'une haute précision de positionnement lors d'applications multi-GNSS utilisant des récepteurs et des antennes multifréquences. Plus particulièrement, la réalisation d'un cadre de référence hautement stable et précis comme base métrologique pour des applications audacieuses comme par exemple la détermination de l'élévation du niveau des océans, nécessite de longues séries temporelles des coordonnées des stations GNSS, stables et calculées avec grande précision. Comme aucune calibration consistante des variations des centres de phase couvrait toutes les principales antennes, Monsieur Willi a relevé le défi en étendant son travail au problème plus général de la calibration absolue des variations des centres de phase des antennes GNSS. En seulement deux ans Monsieur Willi a développé un système complet, et hautement automatisé, de calibration des antennes GNSS en utilisant un robot industriel. Pour ceci il a développé une nouvelle méthode d'analyse des données GNSS par triple différences, ce qui réduit les erreurs dues à la propagation des signaux par chemins multiples, et une séquence optimisée des rotations pour les changements des orientations des antennes à calibrer. De plus il a dû lui-même calibrer le robot industriel en développant un système basé sur un modèle cinématique et un paramétrage de la géométrie du robot: un réel défi en soi. En résumée le système de calibration développé par Monsieur Willi est extrêmement performant ce qui a été démontré par des comparaisons avec d'autres méthodes at aussi avec des résultats sur de courtes lignes de bases poursuivies en collaboration avec swisstopo.

La Commission Géodésique Suisse (CGS) remercie chaleureusement l'auteur pour cette contribution d'une grande valeur, de même que l'Académie Suisse des Sciences Naturelles (SCNAT) pour avoir pris à sa charge les coûts de l'impression du présent fascicule.

Prof. Dr. M. Rothacher

Institut de Géodésie et Photogrammétrie   ETH Zürich
ETH Zürich   Président de la CGS

FOREWORD

The cube satellite mission CubETH of the Institute of Geodesy and Photogrammetry (IGP) at ETH Zurich, a project in collaboration with various partners from academia and industry, had the goal to fly a Global Navigation Satellite System (GNSS) payload consisting of five antennas (four on the zenith-pointing side and one pointing sidewise), each of them connected to two miniature 1-frequency receivers developed by the Swiss company u-blox. The cube satellite with a size of 10 cm by 10 cm by 10 cm was designed to perform orbit as well as attitude determination with the GNSS payload onboard. Due to the fact that the three baselines between the four GNSS antennas on the zenith-pointing side of the small satellite are extremely short, attitude determination becomes a real challenge. This difficulty is even deepened by the circumstance, that the observations collected by the low-cost of-the-shelf (COTS) GNSS receivers may be offset in time by up to 0.5 ms, while the satellite moves at a speed of typically 7 km/s. A further source of error are the large GNSS antenna phase center variations to be expected for the small patch antennas used, heavily degrading the attitude estimates.

Daniel Willi coped successfully with all these problems by, first, developing a very detailed and accurate correction model for the non-synchronized observations and by testing the model based on simulations as well as on an industry robot, reaching an remarkable accuracy of a few degrees on the extremely short baselines of 5-8 cm.

In order to further improve the attitude results on such short baselines, the phase center offsets and variations of the small GNSS patch antennas had to be calibrated. These calibration activities shifted the focus of the PhD thesis of Daniel Willi towards the more general goal of GNSS receiver antenna phase center calibrations.

The calibration of the phase centers of the most important antenna types for all GNSS constellations and for all frequencies used by these GNSS is an absolute necessity for high-accuracy GNSS positioning using multi-GNSS and multi-frequency antennas and receivers. Especially the realization of a highly stable and accurate reference frame, as the metrological basis for very challenging applications such as sea level rise, requires long time series of GNSS station coordinates computed with utmost accuracy and reliability. As a consistent set of antenna phase center calibrations for all major ground antenna types used in high-precision GNSS was still missing, Daniel Willi took up this challenge and extended his antenna calibration work from the relative calibration of the antennas on the CubETH satellite (or similar setups for attitude determination) to the more general issue of absolute antenna phase center calibration.

In just about two years, Daniel Willi developed a complete and highly automated system for GNSS antenna calibrations from scratch, using an industry robot, a new triple-difference GNSS data analysis approach to reduce multipath and an optimized sequence of rotations for changing the orientation of the antenna to be calibrated. In addition, Daniel Willi had to calibrate the industry robot itself based on a kinematic model and a parameterization of the robot geometry, a challenge in itself.

In summary, a very performing antenna calibration system has thus been established by Daniel Willi. Its high-accuracy performance has already been demonstrated by comparisons with other calibration methods and with results on short baselines achieved in collaboration with swisstopo.

The SGC thanks the author for his valuable contribution as well as the Swiss Academy of Sciences (SCNAT) for covering the printing costs of this volume.

Prof. Dr. M. Rothacher

Institute for Geodesy and Photogrammetry   ETH Zürich
ETH Zürich   President of SGC

Abstract

CubETH is a project of a scientific nano-satellite of 10 x 10 x 10 cm^3 size. Its destination is a Low Earth Orbit (LEO) at 450 km height above the Earth surface. The spacecraft is equipped with ten Global Navigation Satellite Systems (GNSS) receivers and five GNSS antennas. The employed GNSS receivers are manufactured by the Swiss company u-blox. They are called 'commercial off-the-shelf' chipsets, but are extremely well suited to be used in space: their power consumption, their weight and their size are very small.

As the satellite is equipped with four antennas on its upper size, GNSS attitude determination can be performed. The attitude is the orientation of the spacecraft relatively to a reference frame, for instance the terrestrial reference frame. In GNSS attitude determination, the relative position of the antennas with respect to each other is used.

In the first part of the present work, an algorithm for GNSS attitude determination was developed. Compared to the algorithms in the scientific literature, the GNSS measurements are extrapolated. The extrapolation term ranges approximately from -6 to +6 m. The need for extrapolation is a consequence of the non-synchronicity of the receivers. The measurement epoch lies within a window of 1 ms around the nominal measurement epoch. Because of the high velocity of the spacecraft in LEO (about 8 km/s), extrapolation of the measurements is crucial.

The new algorithm was tested throughout. A hardware in the loop signal simulator test campaign was conducted successfully. The algorithm was also proven to work in a static real data experiment on the ground.

From the first experiences with a model of the CubETH spacecraft, it became obvious that the limiting factor for the accuracy are the antennas. Mutual coupling of the antennas can theoretically not be excluded for baselines shorter than one wavelength. A relative field calibration was set up to obtain Phase Centre Corrections (PCC) for the antennas on the satellite model. PCC are correction values that depend on the frequency and on the direction of the incoming signals. PCC have been studied since the beginning of the US Global Positioning System (GPS) in the 80s, theoretically and experimentally. However, low-cost antennas in the vicinity of each other, as onboard CubETH, have never been in the scientific focus.

The results from the relative field calibration show that mutual coupling occurs. The magnitude of the PCC range up to several centimetres. It is shown that the application of PCC is crucial in order to estimate an unbiased attitude with GNSS. The experiments also showed the limitation of the relative field calibration. It is extremely prone to multipath errors.

The focus of the second part lies on absolute field calibration for GNSS antennas. A new GNSS antenna calibration system was developed from scratch. It uses a six-axis industrial robot to bring the antenna to be calibrated into various orientations. Reference data is collected on a station just a few metres away from the robot. The data is processed on the triple-difference level, i.e., on time-differences of classical double-differences.

The system is currently able to generate calibrations for any Code Division Multiple Access (CDMA) signal, if enough GNSS spacecraft are visible. Calibration of the Russian GLONASS Frequency Division Multiple Access (FDMA) signals is a matter of implementation.

Various analyses show that the repeatability of the calibrations is below the millimetre-level. A comparison with the de facto standard, PCC from the German company Geo++® GmbH, allowed to verify that the results are meaningful and that they are in the same accuracy range as the reference PCC. Calibrations of GNSS receiver antennas for signals of the European satellite navigation system Galileo were presented at the International GNSS Service (IGS) Workshop 2018 in Wuhan. Our new system is the first absolute field calibration that reportedly generated calibrations for Galileo signals. This is an important step towards a better combination of all available GNSS.

In contrast to the US GPS, Galileo satellites have calibrated emitter antennas. Eventually, PCC of receiver antennas for Galileo signals could be the key to obtain a scale of the terrestrial reference frame from GNSS measurements. This scale would be independent of other space geodetic techniques. This requires both, the transmitter and the receiver antennas to be accurately calibrated.

Zusammenfassung

CubETH ist ein Projekt für einen wissenschaftlichen Satelliten von 10 x 10 x 10 cm^3. Sein Ziel ist eine tiefe Erdumlaufbahn in ungefähr 450 km Höhe über der Erdoberfläche. Der Satellit ist mit zehn Global Navigation Satellite System (GNSS)-Empfängern und fünf GNSS-Antennen ausgerüstet. Die verwendeten Empfänger werden von der Schweizer Firma u-blox hergestellt. Es sind Chips aus der Serienproduktion, doch weisen sie Eigenschaften auf, die sie für einen Einsatz im Weltraum attraktiv machen: sie brauchen wenig Strom, sind leicht und kompakt.

Weil der Satellit vier Antennen auf seiner nach oben gerichteten Fläche aufweist, kann mittels GNSS die Attitude bestimmt werden. Die Attitude ist die Orientierung des Satelliten relativ zu einem Referenzrahmen, zum Beispiel dem terrestrischen Referenzrahmen. Für die GNSS-Attitude-Bestimmung wird das Prinzip der relativen Positionierung der Antennen gegenüber den anderen Antennen ausgenutzt.

Als erster Teil der vorliegenden Arbeit wurde ein Algorithmus für die Attitude-Bestimmung entwickelt. Entgegen den in der wissenschaftlichen Literatur erwähnten Algorithmen enthält der Algorithmus einen Extrapolationsterm. Der Extrapolationsterm beträgt zwischen –6 und +6 m. Die Ursache für den Extrapolationsterm liegt in den nicht synchronisierten Empfängern. Der Messzeitpunkt liegt innerhalb eines Zeitfensters von 1 ms um den nominalen Messzeitpunkt. Wegen der hohen Geschwindigkeit des Satelliten (ungefähr 8 km/s) ist eine Extrapolation der Messungen unabdingbar.

Der neue Algorithmus wurde intensiv getestet. Eine Studie mit einem Signalgenerator und den Empfängern wurde erfolgreich durchgeführt. Der Algorithmus wurde ebenfalls mit echten Daten aus einem statischen Experiment am Boden validiert.

Aus den ersten Experimenten liess sich schliessen, dass die Antennen den entscheidenden Faktor für die Genauigkeit darstellen. Gegenseitige Beeinflussung der Antennen kann theoretisch nicht ausgeschlossen werden, wenn die Basislinienlänge kürzer ist als eine Wellenlänge. Eine relative Feldkalibration wurde aufgesetzt um Phasenzentrumskalibrationen (PZK) für ein Modell des CubETH zu erhalten. PZK sind frequenz- und richtungsabhängige Korrekturwerte für die eintreffenden GNSS-Signale. PZK werden seit Beginn des amerikanischen Global Positioning System (GPS) untersucht, sowohl theoretisch wie auch experimentell. Dennoch war die Kalibration von preiswerten Antennen in direkter Nähe zueinander, wie sie auf CubETH vorkommen, nie im wissenschaftlichen Fokus.

Die Resultate der relativen Feldkalibration zeigen auf, dass gegenseitige Beeinflussung der Antennen untereinander stattfindet. Die ermittelten PZK betragen mehrere Zentimeter. Es wurde aufgezeigt, dass die Verwendung von PZK für die fehlerfreie Schätzung von Attitude unabdingbar ist. Gleichzeitig wurden die Grenzen der relativen Antennenkalibration aufgezeigt. Sie ist extrem empfänglich für Fehler aus Mehrwegausbreitung.

Der Fokus des zweiten Teils liegt bei absoluten Feldkalibrationen für GNSS-Antennen. Von Grund auf wurde ein operationelles Kalibrierungssystem für GNSS-Antennen entwickelt. Dieses

besteht aus einen Sechs-Achsen-Industrieroboter, der die Antenne in alle möglichen Orientierungen bringt. Referenzdaten werden von einer nur wenige Meter vom Roboter entfernten Station aufgenommen. Die Daten werden auf Dreifachdifferenz-Stufe ausgewertet. Dreifachdifferenzen sind Zeitdifferenzen von klassischen Doppeldifferenzen.

Das System kann im jetzigen Zustand Kalibrationen für alle Code Division Multiple Access (CDMA) Signale generieren, vorausgesetzt es sind genug Satelliten sichtbar. Kalibrationen für die russischen GLONASS Frequency Division Multiple Access (FDMA) Signale sind auch denkbar, sofern diese auch implementiert werden.

Diverse Analysen zeigen, dass die Wiederholbarkeit der Kalibrationen bei unter einem Millimeter liegt. Ein Vergleich mit dem de facto Standard, den PZK der deutschen Firma Geo++$^{®}$ GmbH, zeigen auf, dass die erhaltenen Resultate plausibel sind und im selben Genauigkeitsbereich liegen wie die Referenz. Kalibrationen von GNSS-Empfangsantenne für die Signale vom europäischen Satelliten-Navigationssystem Galileo wurden am International GNSS Service (IGS) Workshop 2018 in Wuhan vorgestellt. Unser System ist das erste absolute Feldkalibrationssystem, das nachweislich Galileo-Kalibrationen generiert hat. Dies ist ein wichtiger Schritt zur besseren Kombination aller verfügbaren GNSS.

Im Gegensatz zum amerikanischen GPS weisen Galileo-Satelliten kalibrierte Sendeantennen auf. Letzten Endes wird die Kalibration von Empfängerantennen für die Galileo-Signale der Schlüssel zur Bestimmung des Massstabs des terrestrischen Referenzrahmens aus GNSS sein. Dieser Massstab wäre unabhängig von demjenigen anderer weltraumgeodätischen Techniken. Dies erfordert jedoch, dass sowohl die Sendeantennen wie auch die Bodenantennen hochgenau kalibriert werden.

Résumé

CubETH est le projet d'un nano-satellite de 10 x 10 x 10 cm³. Il est destiné à une orbite basse à environ 450 km d'altitude au-dessus de la surface de la terre. Cet astronef est équipé de dix récepteurs de système de positionnement par satellites (Global Navigation Satellite System, GNSS) et cinq antennes GNSS. Les récepteurs GNSS utilisés sont fabriqués par l'entreprise suisse u-blox. Il s'agit d'équipement électronique standard, mais leurs performances les rendent parfaits pour une utilisation dans l'espace : ils sont peu énergivores, de petite taille et légers.

Le satellite étant équipé de quatre antennes sur sa face supérieure, la détermination de l'attitude devient possible. L'attitude est l'orientation du satellite par rapport à un cadre de référence, par exemple le cadre de référence terrestre. La détermination de l'attitude par GNSS est basée sur le positionnement relatif des antennes par rapport aux autres antennes.

Dans la première partie de ce travail, un algorithme pour la détermination de l'attitude par GNSS a été développé. Contrairement aux autres algorithmes présents dans la littérature scientifique, les données GNSS sont extrapolées. Le terme d'extrapolation mesure entre –6 et +6 mètres. La nécessité du terme d'extrapolation découle du non- synchronisme des récepteurs. L'instant de mesure se situe dans une plage de 1 ms autour de l'époque nominale. A cause de la grande vitesse du satellite en orbite basse (environ 8 km/s), l'extrapolation des mesures est indispensable.

Le nouvel algorithme a été soigneusement testé. Une simulation avec un générateur de signaux GNSS et les récepteurs a été menée avec succès. Le bon fonctionnement de l'algorithme a aussi été prouvé dans une expérience statique au sol et avec de vrais signaux GNSS.

Dès les premières expériences avec un modèle du satellite, il était évident que les antennes seraient le facteur limitant la précision. Une influence mutuelle des antennes ne peut pas être exclue pour des lignes de bases plus courtes qu'une longueur d'onde. Une calibration de terrain relative est mise en place afin d'obtenir les Corrections des Centres de Phases (CCP) pour les antennes du satellite. Les CCP sont des valeurs de correction qui dépendent de la fréquence et de la direction du signal reçu. Les CCP sont étudiées depuis les débuts du Global Positioning System (GPS) des États-Unis d'Amérique dans les années 80, tant à un niveau théorique qu'expérimental. Cependant, la calibration d'antennes à bas coût à proximité l'une de l'autre, comme sur CubETH, n'a jamais été au centre de l'attention scientifique.

Les résultats obtenus lors des calibrations relatives montrent qu'une influence mutuelle des antennes se produit. La magnitude des CCP est de plusieurs centimètres. Il est démontré que la prise en compte des CCP est cruciale afin d'estimer une attitude GNSS qui soit libre de biais. Les expériences ont aussi montré les limites de la calibration de terrain relative. Elle est susceptible aux erreurs dues aux propagation par trajets multiples.

Le focus de la deuxième partie sont les calibrations de terrain absolues pour les antennes GNSS. Un système opérationnel de calibrations d'antennes GNSS a été développé en partant

de zéro. Il utilise un robot industriel à six axes afin de tourner l'antenne GNSS dans tous les sens. Des données de références sont collectées par une station à quelques mètres du robot. Les mesures sont traitées sous forme de triple-différences. Les triples-différences sont des différences temporelles des doubles-différences classiques.

Le système est actuellement capable de générer des calibrations pour n'importe quel signal modulé par accès multiple par répartition en code (AMRC), tant que suffisamment de satellites sont visibles. Les calibrations pour les signaux modulés par accès multiple par répartition en fréquence (AMRF) du système russe GLONASS sont en principe également possible; il s'agit de les implémenter dans le logiciel.

Diverses analyses ont montré que la répétabilité des calibrations était meilleure que le millimètre. Une comparaison avec le standard de facto, les PCC de l'entreprise allemande Geo++® GmbH, ont permis de vérifier la vraisemblance des résultats. La précision des résultats est similaire à la précision des résultats de référence. La calibration d'antennes pour les signaux du système européen de navigation Galileo ont été présentés au Workshop 2018 du « International GNSS Service » (IGS) à Wuhan. Notre nouveau système est la première calibration de terrain absolue avérée à générer des calibrations pour les signaux Galileo. Ceci est une étape importante vers une meilleure combinaison de tous les GNSS disponibles.

Contrairement au GPS américain, les antennes d'émission des satellites Galileo sont calibrées. Un jour ou l'autre, les CCP des antennes de récepteurs pour les signaux Galileo pourraient être la clé pour déterminer l'échelle du système de référence terrestre à partir de mesures GNSS. Cette échelle serait indépendante des autres techniques de géodésie spatiale. Ceci requiert que les antennes de transmission ainsi que les antennes de réception soient précisément calibrées.

Contents

List of Figures

List of Tables

Abbreviations

ANTEX	**Ant**enna **Ex**hange Format
APC	**A**ctual **P**hase **C**entre
ARP	**A**ntenna **R**eference **P**oint
AWG	**A**ntenna **W**orking **G**roup
CDDIS	**C**rustal **D**ynamics **D**ata **I**nformation **S**ystem
CDMA	**C**ode **D**ivision Multiple **A**ccess
CODE	**C**entre for **O**rbit **D**etermination in **E**urope
COTS	**C**ommercial **o**ff-**t**he-**S**helf
DH	**D**enavit-**H**artenberg
DLR	**D**eutsches Zentrum für **L**uft- und **R**aumfahrt
EPN	**E**uropean **P**ermanent **N**etwork
ETH	**E**idgenössische **T**echnische **H**ochschule
FDMA	**F**requency **D**ivision Multiple **A**ccess
GNSS	**G**lobal **N**avigation **S**atellite **S**ystem
GPS	**G**lobal **P**ositioning **S**ystem
ICD	**I**nterface **C**ontrol **D**ocument
IERS	**I**nternational **E**arth **R**otation and Reference Systems **S**ervice
IGP	**I**nstitute of **G**eodesy and **P**hotogrammetry
IGS	**I**nternational **GNSS S**ervice
IGS AWG	**I**nternational **GNSS S**ervice **A**ntenna **W**orking **G**roup
INS	**I**nertial **N**avigation **S**ystem
ION	**I**nstitute **o**f **N**avigation
ITRF	**I**nternational **T**errestrial **R**eference **F**rame

LAMBDA	**L**east Squares **Amb**iguity **D**ecorrelation **A**djustment
LEO	**L**ow **E**arth **O**rbit
LLF	**L**ocal **L**evel **F**rame
LOS	**L**ine **of S**ight
MJD	**M**odified **J**ulian **D**ate
MPC	**M**ean **P**hase **C**entre
NASA	(US) **N**ational **A**eronautics and **S**pace **A**dministration
NEQ	**N**ormal **Eq**uation
PCC	**P**hase **C**entre **C**orrection
PCO	**P**hase **C**entre **O**ffset
PCV	**P**hase **C**entre **V**ariations
PPP	**P**recise **P**oint **P**ositioning
PVT	**P**osition, **V**elocity and **T**ime
RINEX	**R**eceiver **In**dependent **Ex**change Format
RMS	**R**oot **M**ean **S**quare
RMSE	**R**oot **M**ean **S**quare **E**rror
RSI	**R**obot**S**ensor**I**nterface
SDR	**S**oftware **D**efined **R**adio
SPP	**S**ingle **P**oint **P**ositioning
UAV	**U**nmanned **A**erial **V**ehicle
UBX	**U-b**lo**x** Binary Format
UDP	**U**ser **D**ata **P**rotocol
WGS84	**W**orld **G**lobal **S**ystem 1984
XML	**E**xtensible **M**arkup **L**anguage

Constants

Physical constants according to IS-GPS-200 (2015)

Speed of light	c	=	$2.997\ 924\ 58 \times 10^8$ m s^{-1}
Earth's gravitational constant	μ_e	=	$3.986\ 005\ \times 10^{14}$ m^3 s^{-2}

Physical constants according to IERS (Petit and Luzum, 2010)

Speed of light	c	=	$2.997\ 924\ 58 \times 10^8$ m s^{-1}
Earth's gravitational constant	μ_e	=	$3.986\ 004\ 418\ \times 10^{14}$ m^3 s^{-2}

GNSS centre frequencies

GPS

L1 signal	f_c	=	1 575.42 MHz
L2 signal	f_c	=	1 227.6 MHz
L5 signal	f_c	=	1 176.45 MHz

GLONASS

G1 signal, with $k \in [-7, -6, ..., 6]$	f_c	=	$1\ 602 + \frac{9}{16}\ k$ MHz
G2 signal, with $k \in [-7, -6, ..., 6]$	f_c	=	$1\ 246 + \frac{7}{16}\ k$ MHz
G3 signal	f_c	=	1 202.025 MHz

Galileo

E1 signal	f_c	=	1 575.42 MHz
E5a signal	f_c	=	1 176.45 MHz
E5b signal	f_c	=	1 207.14 MHz
E5 (E5a+E5b) signal	f_c	=	1 191.795 MHz
E6 signal	f_c	=	1 278.75 MHz

SBAS

L1 signal	f_c	=	1 575.42 MHz
L2 signal	f_c	=	1 176.45 MHz

BeiDou

B1 signal	f_c	=	1 561.098 MHz
B2 signal	f_c	=	1 207.14 MHz
B3 signal	f_c	=	1 268.52 MHz

QZSS

L1 signal	f_c	=	1 575.42 MHz
L2 signal	f_c	=	1 227.6 MHz
L5 signal	f_c	=	1 176.45 MHz
LEX signal	f_c	=	1 278.75 MHz

IRNSS

L5 signal	f_c	=	1 176.45 MHz
S signal	f_c	=	2 492.028 MHz

Symbols

General symbols

$\mathbf{X}$	a matrix
$\mathbf{x}$	a vector
$\underset{3\times3}{\mathbf{X}}$	size of $\mathbf{X}$
X_{ij}	element on line i and column j of $\mathbf{X}$
x_i	i^{th} element of $\mathbf{x}$
X	a scalar
$\mathbf{X}^{\text{T}}$	a transposed matrix
$\mathbf{x}^{\text{T}}\mathbf{y}$	a scalar product, equals $\langle\mathbf{x},\mathbf{y}\rangle$
$\widetilde{X}$	approximation of quantity X
$\widehat{X}$	estimation of quantity X
X^-	propagation of quantity X
$\dot{X}$	time derivative of quantity X

Spaces

$\mathbb{Z}$	Integer number

Attitude representation

$\mathbf{0}_{i\times j}$	a i times j matrix with zeros
$\mathbf{I}_i$	the i times i identity matrix
$\mathbf{R}$	orthogonal rotation or attitude matrix
$\mathbf{R}_i$	rotation around the ith coordinate axis
$\mathbf{T}$	quaternion rates matrix
$\mathbf{b}$	baseline vector (in the body fixed frame)
$\mathbf{n}$	rotation axis unit vector
$\mathbf{q}$	quaternion
$\alpha,\ \beta,\ \gamma$	yaw, pitch and roll angles
$\boldsymbol{\omega}$	rotation vector

GNSS symbolism

$\mathbf{D}$	Zero-difference to double-difference operator
$\mathbf{Q}_{ll}$	Variance-covariance of the observations
$\mathbf{e}$	line-of-sight unit vector
$\mathbf{v}$	velocity vector
$\mathbf{x}$	position vector
E	GNSS attitude extrapolation term
I	ionospheric delay
N	integer phase ambiguity (in cycles)
P	GNSS phase observation
T	tropospheric delay
W	GNSS phase wind-up
v	residual
z	zenith angle
α	azimuth
δt	receiver or satellite clock error
σ_p	standard deviation of a phase observation
λ	GNSS carrier phase wavelength

Kalman filter symbolism

$\mathbf{A}$	system model function Jacobian matrix
$\mathbf{F}$	state transition function Jacobian matrix
$\mathbf{G}$	noise shaping matrix
$\mathbf{H}$	observation function Jacobian matrix
$\mathbf{K}$	Kalman gain matrix
$\mathbf{P}$	state variance-covariance
$\mathbf{U}$	process variance-covariance
$\mathbf{V}$	observation variance-covariance
$\mathbf{a(x)}$	system model function
$\mathbf{f(x)}$	state transition function
$\mathbf{h(x)}$	observation function
$\mathbf{u}$	process noise
$\mathbf{v}$	observation residuals
$\mathbf{x}$	state vector
$\mathbf{z}$	observation vector

Robot kinematics symbolism

$\mathbf{R}_{r\leftarrow f}$	Rotation from flange coordinates to robot coordinates
$\mathbf{R}_{r\leftarrow t}$	Rotation from tool coordinates to robot coordinates
$\mathbf{R}_{f\leftarrow t}$	Rotation from tool coordinates to flange coordinates
$\mathbf{c}$	Coordinates of the intersection of the last three robot axis
$\mathbf{t}$	Robot tool coordinates
$\mathbf{u}$	Robot flange coordinates
θ_i	Angle of the ith axis of the robot
$t'_x,\ t'_y,\ t'_z$	Robot x- y- and z-coordinates in the world frame
$t''_x,\ t''_y,\ t''_z$	Tool x- y and z-offsets in the tool frame
$\alpha',\ \beta',\ \gamma'$	Robot yaw, pitch and roll angles in the world frame
$\alpha'',\ \beta'',\ \gamma''$	Tool yaw, pitch and roll angles in the flange frame

Geometrical robot model

a_i	Offset parameters
b	Alignment parameter
d_i	Length parameters

Denavit-Hartenberg model

$\mathbf{T}$	Homogeneous transformation matrix (of the flange)
$\mathbf{T}_i$	Homogeneous transformation matrix associated to joint and link pair i
Θ_i	Joint angular reading parameter
α_i	Joint torsion parameter
a_i	Link offset parameter
d_i	Link length parameter

Various

$N(\mu, \sigma^2)$	Normal distribution with mean μ and standard deviation σ
atan2	multi-valued inverse tangent

Chapter 1

Introduction

CubETH is a nano-satellite project under the lead of the Institute of Geodesy and Photogrammetry (IGP) at ETH Zurich. It is a collaboration between several universities, universities of applied sciences and companies in Switzerland. This work is part of the CubETH project and was supported by ETH Research Grant ETH-43 14-2.

The idea for CubETH was triggered by recent developments in Global Navigation Satellite System (GNSS) receiver technology. u-blox, a receiver manufacturer located in Thalwil (Switzerland), is a world leader in miniaturized multi-GNSS receivers. Because of their remarkable performance, the idea came up to use these commercial off-the-shelf (COTS) chipsets for a space mission. This would highly reduce the cost of GNSS positioning in space and make precise positioning affordable for small missions.

The design study foresees a spacecraft of 10 x 10 x 10 cm^3, equipped with five GNSS antennas and ten GNSS receivers (see Figure 1.0.1). The main mission goal is technology demonstration. It will be attempted to prove that the u-blox receivers can be used in space. The secondary mission goal is attitude determination. Attitude is a body's orientation in space. Attitude determination is possible because the tiny satellite is equipped with several antennas. Through the relative positioning of the antennas with respect to each other, the attitude can be estimated.

The first part of this work deals with the challenge of **attitude determination** with the u-blox receivers. The u-blox chips are not equipped with clock steering. Therefore, the different receivers are not synchronised with each other. The goal of the work presented in **Chapter 2** is to develop an algorithm for attitude determination with non-synchronised receivers.

The classical way to enhance the accuracy of GNSS attitude determination is to increase the length of the baselines between the antennas. On the small CubETH, the baseline lengths are limited by the size of the satellite. Because the accuracy cannot be increased by increasing the baseline length, special attention has to be put on the accuracy of the antennas. The shorter the baseline, the larger the influence of antenna errors onto the estimation of the attitude. A **general introduction to antenna calibration** is provided in **Chapter 3**.
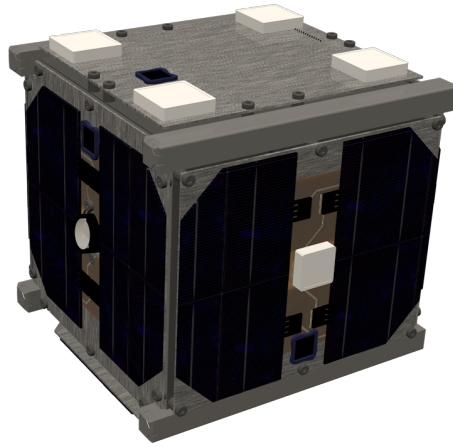
Figure 1.0.1 : Digital rendering of a CAD model of the 10 x 10 x 10 cm^3 CubETH spacecraft. The white patches are the GNSS antennas. Four antennas are placed on the zenith looking face, one antenna on the side serves experimental purposes.

An additional difficulty on very short baselines is the potential coupling of the antennas because of their proximity. This challenge was addressed in **Chapter 4**; a **relative field calibration** method was set up and a campaign was conducted with the goal to investigate the behaviour of the antennas on the CubETH model.

The subsequent chapters present the development of an absolute field calibration method for GNSS antennas. This method, using a robotic arm, is able to reduce the impact of multipath on the estimated antenna calibration. Thus, it is expected to deliver more reliable results than the relative field calibration.

In order to use the robotic arm for high-accuracy antenna calibration, its kinematics and its accuracy needed to be studied: all aspects related to the **kinematics of the robotic arm** are covered in **Chapter 5**. The **absolute field calibration** method using this robot is detailed in **Chapter 6**.

Chapter 2

GNSS Attitude Determination

GNSS attitude determination has been performed since the very beginning of the Global Positioning System (GPS). An excellent introduction on general attitude determination is provided in Giorgi (2017). On spacecraft in Low Earth Orbit (LEO), GNSS attitude determination is performed since the nineties (Cohen, 1992). GNSS attitude determination has some appreciable advantages over other techniques, as star trackers or inertial navigation systems (INS). It is autonomous in acquiring an initial solution, it needs only two visible GNSS satellites for a deterministic solution, it is resistant to high spin rates and it provides position, velocity and time (PVT; Arbinger and Enderle, 2000). Compared to INS, it is free of drift.

On the other hand, the amount of raw data to process is considerable and the system is very sensitive to multipath. And maybe more importantly, its accuracy is very modest compared to star trackers.

Nevertheless, GNSS attitude determination remains an attractive technique, especially if its availability is granted for free, as in the case of the satellite CubETH. The four antennas on the upper side of the spacecraft allow for GNSS attitude determination.

In the following chapter, the state of art of attitude determination onboard spacecraft in LEO is discussed, followed by a presentation of the governing equations and principles. The chapter is concluded by a summary of the first publication.

2.1   State of the Art

RADCAL was one of the first missions to perform attitude determination in space (Cohen et al., 1994). Dedicated Trimble TANS Quadrex receivers, specially adapted by Stanford University, were used. A receiver was connected to the four antennas, and a second receiver was carried as spare. The four antennas are evenly distributed on the upper face of the cylindrical spacecraft with a diameter of about 0.75 meters. The authors of the study compared the GPS attitude to the attitude obtained from the gravitational dynamics of the spacecraft. The estimated accuracy lies around 1 deg and is limited by uncertainties in the antenna Phase Centre Variations (PCV)

and in the electrical delays. The authors state that the accuracy inherent to the system lies around 0.3 deg.

In 2000, a modified Trimble Force-19 receiver was flown onboard the space shuttle Atlantis in order to perform an attitude determination experiment (Um and Lightsey, 2001). Again, dedicated space receivers were used. Attitude from a star tracker served as ground truth. Interestingly, the authors tried to model the multipath originating from the spacecraft with a spherical harmonics model. This approach was qualified unsuccessful. The lack of flight data and the complex geometry of the environment were given as explanations. The authors also compared two approaches for the combination with the INS, firstly using differentiated phase observables, secondly using quaternion observations previously generated from GPS. The first approach was clearly preferred, as the accuracy of the results increased. Additionally, phase measurements can enter the filter algorithm even if not enough satellites are visible for a quaternion solution. In the conclusions, the authors estimate that 90% of the error budget is due to multipath.

Other authors studied attitude determination (designed for space) in ground tests. All authors use carrier phase observables, but many differences are found in the way of processing the observations and in the parametrisation of the attitude.

Arbinger and Enderle (2000) tested a combination of GPS and a star tracker on a turn table on the ground. The GPS-based solution is obtained using an iterative solution to Wahba's problem and after solving the phase ambiguities. The comparison led to the conclusion that the GPS solution is affected by much more jitter than the star tracker solution. Furthermore, an offset between the GPS solution and the star tracker solution remains unexplained.

Kim and Langley (2007) studied a system based on the COTS receivers Novatel OEM4-G2L, aimed to operate on the small satellite CASSIOPE. The system consists of three receivers (and an additional spare). Ambiguities are solved epoch-wise using a wide-lane linear combination and adding the baseline lengths as pseudo-observations in the adjustment. The normalization of the attitude matrix is achieved by transforming the matrix into Euler angles and then computing an orthogonal matrix with these Euler angles. An experiment with a turning table demonstrated the ability to reach 5 deg accuracy with baseline lengths between 1 and 1.6 m.

A last group of authors studied the behaviour of algorithms in GNSS simulator studies. Ziebart and Cross (2003) used synthetic data and a very complete attitude determination algorithm. Euler angles were chosen as parametrisation. The initial ambiguity resolution is performed using a search in the attitude space. Under realistic observation noise, sub-degree accuracy was found to be achievable with 2 to 3 m baselines. Assuming a realistic stochastic model, the algorithm performs well in outlier detection.

Nadarajah et al. (2012) performed hardware-in-the-loop simulator tests with a Spirent GSS6560 signal generator. NamuruV2Rx receivers were used. The processing is achieved in two steps. First, an epoch-wise solution is generated with a modified version of the LAMBDA algorithm (see for instance Park and Teunissen, 2003; Teunissen, 1995; Teunissen, 2010), then this solution is filtered in an unscented Kalman filter. In conclusion, the angular error was found

to depend strongly on the geometry of the GPS constellation. Root Mean Square Errors (RMSE) in the order of one degree were obtained for a configuration with two baselines of one metre length.

GNSS attitude determination is also intensely studied for other applications than on spacecraft. This includes studies on Earth, for instance on ships (Giorgi et al., 2012), onboard planes (Van Graas and Braasch, 1991; Cannon and Sun, 1996), for UAV (Sabatini et al., 2012) or for terrestrial applications (Chen and Qin, 2012; Aghili and Salerno, 2013).

2.2 Research gap

The CubETH project aims at using COTS receivers of the type u-blox M8. The u-blox receiver clock is only partially steered, resulting in an actual measurement epoch within a time window of 1 ms around the nominal 1 Hz measurement epoch (u-blox, 2014). The velocity of an Earth's satellite in an circular orbit can be computed as:

$$v = \sqrt{\frac{\mu_e}{r}} \tag{2.1}$$

with μ_e being the Earth's gravitational constant and r the radius of the orbit. For a satellite in a 400 km orbit, this results in approximatively 8 km/s. At this speed, the spacecraft travels 8 m in one millisecond, which is the synchronisation error of the receivers. It is obvious, that under theses circumstances, an extrapolation of the measurements is of tremendous importance.

In previous studies, either dedicated receivers running on a common oscillator or receivers with well steered clocks were used.

Furthermore, no paper gave a fully satisfactory solution for the handling of the parametrisation of the attitude. The present chapter addresses both issues: a consistent mathematical formulation for the attitude parametrisation within a Kalman filter is derived on the observation level and a procedure for the extrapolation of the measurements is developed. The chosen extrapolation method works in real-time and is not dependent on any precise products, like precise orbits or precise clocks.

2.3 Parametrisation of attitude

The attitude describes the orientation of a body in space:

$$\mathbf{b}_{\text{world}} = \mathbf{R}_{\text{world}\leftarrow\text{body}} \ \mathbf{b}_{\text{body}} \tag{2.2}$$

where $\mathbf{b}_{\text{system}}$ is the baseline vector in the respective coordinate system and $\mathbf{R}$ is the rotation matrix between the two coordinate systems. The body coordinate system is usually attached to the rigid body. For example, a rigid body coordinate system attached to a plane could have its x-axis pointing in flight direction, its y-axis in wing direction, and the z-axis complementing

the right-hand system. The space of all rotations is the 3D special orthogonal group $SO(3)$. Because attitude is described by a rotation, $\mathbf{R} \in SO(3)$.

In consequence:

$$\mathbf{R}\,\mathbf{R}^{\mathrm{T}} = \mathbf{R}\,\mathbf{R}^{-1} = \mathbf{I}_3 \tag{2.3}$$

with $\mathbf{I}_3$ being the identity matrix. This condition expresses the orthogonality of the matrix. Within an adjustment process, rotation matrices are difficult to handle, as additional constraints are necessary in order to maintain the orthogonality.

The main alternatives to rotation matrices are Euler angle sequences and quaternions. Euler angle sequences suffer from singularities, the so-called 'gimbal lock'. Quaternions do not have this disadvantage, but an additional parameter is needed. Various conventions exist for both representation forms. The following section briefly presents the chosen convention. A complete overview of attitude parametrisations is provided in Diebel (2006). Attitude parametrisation is also discussed in the inertial navigation or GNSS literature, for instance in Jekeli (2001) respectively in Giorgi (2017).

2.3.1 Euler angle sequences

An Euler angle sequence is the combination of three different coordinate axis rotations. Coordinate axis rotations rotate a vector around one axis of the coordinate system and are defined as follows:

$$\mathbf{R}_1(\alpha) = \begin{pmatrix} 1 & 0 & 0 \\ 0 & \cos\alpha & \sin\alpha \\ 0 & -\sin\alpha & \cos\alpha \end{pmatrix} \tag{2.4}$$

$$\mathbf{R}_2(\alpha) = \begin{pmatrix} \cos\alpha & 0 & -\sin\alpha \\ 0 & 1 & 0 \\ \sin\alpha & 0 & \cos\alpha \end{pmatrix} \tag{2.5}$$

$$\mathbf{R}_3(\alpha) = \begin{pmatrix} \cos\alpha & \sin\alpha & 0 \\ -\sin\alpha & \cos\alpha & 0 \\ 0 & 0 & 1 \end{pmatrix} \tag{2.6}$$

where $\mathbf{R}_i$ is a rotation around the ith axis of the coordinate system and α is the angle of rotation. The 321 Euler sequence is defined as follows:

$$\mathbf{R}_{\mathrm{local \leftarrow global}} = \mathbf{R}_1(\gamma)\,\mathbf{R}_2(\beta)\,\mathbf{R}_3(\alpha) \tag{2.7}$$

Note that this rotation matrix would be the transpose of the attitude matrix as defined in Eq. 2.2. α, β and γ are the yaw, pitch and roll angles. If $\beta = \frac{\pi}{2} + n\,\pi, n \in \mathbb{Z}$, the system is in a singularity. In that case, the rotations $\mathbf{R}_1$ and $\mathbf{R}_3$ have the same derivatives and the system looses one degree of freedom. Mechanically spoken, if thinking of cardans, the first and the last

cardan would be parallel, thus being in gimbal lock.

The inverse function reads:

$$
\left.
\begin{aligned}
\alpha &= \text{atan2}\,(R_{12}, R_{11}) \\
\beta &= -\arcsin\,(R_{13}) \\
\gamma &= \text{atan2}\,(R_{23}, R_{33})
\end{aligned}
\right\} \quad \text{if } |R_{13}| \neq 1 \tag{2.8}
$$

$$
\left.
\begin{aligned}
\alpha &= \text{atan2}\,(-R_{21}, R_{22}) \\
\beta &= -\arcsin\,(R_{13}) \\
\gamma &= 0
\end{aligned}
\right\} \quad \text{if } |R_{13}| = 1 \tag{2.9}
$$

where $R_{i,j}$ is the element in line i and column j of the matrix $\mathbf{R}_{\text{local}\leftarrow\text{global}}$. In case of a singularity, an infinite number of solutions exists. One way to resolve this singularity is to set γ to zero.

The 323 Euler sequence consistently reads:

$$
\mathbf{R}_{\text{local}\leftarrow\text{global}} = \mathbf{R}_3(\gamma)\,\mathbf{R}_2(\beta)\,\mathbf{R}_3(\alpha) \tag{2.10}
$$

This parametrisation has a singularity at $\beta = 0 + n\,\pi, n \in \mathbb{Z}$ and would therefore be useless for the estimation of the attitude, but is convenient in other cases, for instance for the description of the position of a robot. To give an another example, for the Earth orientation, the sequence 313 is frequently used.

The inverse function of the 323 Euler sequence reads:

$$
\left.
\begin{aligned}
\alpha &= \text{atan2}\,(R_{32}, R_{31}) \\
\beta &= \arccos\,(R_{33}) \\
\gamma &= \text{atan2}\,(R_{23}, -R_{13})
\end{aligned}
\right\} \quad \text{if } |R_{33}| \neq 1 \tag{2.11}
$$

$$
\left.
\begin{aligned}
\alpha &= \text{atan2}\,(-R_{21}, R_{22}) \\
\beta &= \arccos\,(R_{33}) \\
\gamma &= 0
\end{aligned}
\right\} \quad \text{if } |R_{33}| = 1 \tag{2.12}
$$

2.3.2 Quaternions

Quaternions are four element vectors with a scalar part and a vector part:

$$\mathbf{q}_{\text{local}\leftarrow\text{global}} = \begin{pmatrix} q_0 \\ q_1 \\ q_2 \\ q_3 \end{pmatrix} = \begin{pmatrix} q_0 \\ \mathbf{q}_{1:3} \end{pmatrix} = \begin{pmatrix} \cos\left(\frac{\alpha}{2}\right) \\ \sin\left(\frac{\alpha}{2}\right)\mathbf{n} \end{pmatrix} \tag{2.13}$$

where $\mathbf{q}$ is a quaternion that represents a rotation by the angle α around the axis $\mathbf{n}$. The advantage of this parametrisation is its constant norm:

$$q = \sqrt{q_0^2 + q_1^2 + q_2^2 + q_3^2} = 1 \tag{2.14}$$

Quaternions not having a norm equal to one do not represent pure rotations. Within the adjustment, several techniques can be applied to guarantee a norm of one:

i. Only three quaternion elements are estimated and the fourth one is computed,

ii. All four elements are estimated and a constraint on the norm is applied or

iii. All four elements are estimated and the quaternion is normalised after each iteration in the estimation.

In the case of a Kalman filter, (iii) is largely sufficient, if the update rate of the filter is high compared to the dynamics of the system. In this case, the change of the norm of the quaternion is very small at every iteration step and can well be handled with normalisation.

Quaternions can be transformed to rotation matrices using following formula:

$$\mathbf{R} = \begin{pmatrix} q_0^2 + q_1^2 - q_2^2 - q_3^2 & 2\,q_1\,q_2 + 2\,q_0\,q_3 & 2\,q_1\,q_3 - 2\,q_0\,q_2 \\ 2\,q_1\,q_2 - 2\,q_0\,q_3 & q_0^2 - q_1^2 + q_2^2 - q_3^2 & 2\,q_2\,q_3 + 2\,q_0\,q_1 \\ 2\,q_1\,q_3 + 2\,q_0\,q_2 & 2\,q_2\,q_3 - 2\,q_0\,q_1 & q_0^2 - q_1^2 - q_2^2 + q_3^2 \end{pmatrix} \tag{2.15}$$

A quaternion can be obtained from a rotation matrix using following relationship:

$$\left. \begin{aligned} \mathbf{q} &= \frac{1}{2\sqrt{k}}(k, R_{23} - R_{32}, R_{31} - R_{13}, R_{12} - R_{21})^{\mathrm{T}} \\ k &= 1 + R_{11} + R_{22} + R_{33} \end{aligned} \right\} \quad \begin{aligned} &\text{if } R_{22} \geq -R_{33},\ R_{11} \geq -R_{22}, \\ &\qquad R_{11} \geq -R_{33} \end{aligned}$$

$$\tag{2.16}$$

$$\left. \begin{aligned} \mathbf{q} &= \frac{1}{2\sqrt{k}}(R_{23} - R_{32}, k, R_{12} + R_{21}, R_{31} + R_{13})^{\mathrm{T}} \\ k &= 1 + R_{11} - R_{22} - R_{33} \end{aligned} \right\} \quad \begin{aligned} &\text{if } R_{22} < -R_{33},\ R_{11} \geq R_{22}, \\ &\qquad R_{11} \geq R_{33} \end{aligned}$$

$$\tag{2.17}$$

$$
\left.\begin{aligned}
\mathbf{q} &= \frac{1}{2\sqrt{k}}(R_{31} - R_{13}, R_{12} + R_{21}, k, R_{23} + R_{32})^{\mathrm{T}} \\
k &= 1 - R_{11} + R_{22} - R_{33}
\end{aligned}\right\} \quad
\begin{aligned}
&\text{if } R_{22} \geq R_{33},\ R_{11} < R_{22}, \\
&\qquad R_{11} < -R_{33}
\end{aligned}
$$

$$(2.18)$$

$$
\left.\begin{aligned}
\mathbf{q} &= \frac{1}{2\sqrt{k}}(R_{12} - R_{21}, R_{31} + R_{13}, R_{23} + R_{32}, k)^{\mathrm{T}} \\
k &= 1 - R_{11} - R_{22} + R_{33}
\end{aligned}\right\} \quad
\begin{aligned}
&\text{if } R_{22} < R_{33},\ R_{11} < -R_{22}, \\
&\qquad R_{11} < R_{33}
\end{aligned}
$$

$$(2.19)$$

The derivatives of the quaternions can be linked to angular velocities via the following function:

$$
\dot{\mathbf{q}}(\mathbf{q}, \boldsymbol{\omega}) = (\dot{q}_0, \dot{q}_1, \dot{q}_2, \dot{q}_3)^{\mathrm{T}} = \frac{1}{2}\mathbf{T}^{\mathrm{T}}(\mathbf{q})\,\boldsymbol{\omega} \tag{2.20}
$$

$$
\mathbf{T}(\mathbf{q}) = \begin{pmatrix} -q_1 & +q_0 & -q_3 & +q_2 \\ -q_2 & +q_3 & +q_0 & -q_1 \\ -q_3 & -q_2 & +q_1 & +q_0 \end{pmatrix} \tag{2.21}
$$

where $\boldsymbol{\omega}$ is the rotation vector in the global frame and $\mathbf{T}$ is the quaternion rate matrix. Alternative formulations allow to express the angular velocities in the local (or body) frame (see Diebel, 2006).

2.4 Principle of GNSS attitude determination

GNSS attitude determination is based on the following principle (see Figure 2.4.1): the baseline vectors are perfectly known in the body-fixed frame of the spacecraft, but observed in a world coordinate system, for instance WGS84:

$$
r = \mathbf{e}_{\text{world}}^{\mathrm{T}}\,\mathbf{R}_{\text{world}\leftarrow\text{body}}\,\mathbf{b}_{\text{body}} + v \tag{2.22}
$$

where r is a range difference, $\mathbf{e}_{\text{world}}^{\mathrm{T}}$ is the line-of-sight (LOS) in the world frame and v is the observation noise, which is assumed to be normally distributed. This last term makes obvious that Eq. 2.22 is an observation equation. The observable is typically a carrier phase observation. Eq. 2.22 is valid assuming that the baselines are shorter than a few meters and that the body is rigid.

If measurements are taken over several baselines and several satellites are seen by the antennas, the attitude is over-determined and can be estimated with least-squares:

$$
L(\mathbf{R}) = \sum_k \sum_i \frac{1}{\sigma_{ik}^2}\left(r_{ik} - \mathbf{e}^{i\,\mathrm{T}}\,\mathbf{R}\,\mathbf{b}_k\right)^2 \tag{2.23}
$$

where L is the cost function and σ_{ik} is the observation noise of the range difference on baseline

k to satellite i. The minimization of this function is well known as Wahba's problem (Farrell et al., 1966). Some analytical solutions exist to solve this problem, but are limited to the case of vector observations (Cohen, 1992). As processing speed is not critical nowadays, these methods are not of much interest anymore. Preferentially, raw GNSS phase observations are processed directly. The main advantage of a proper least-squares formulation is, that correlations between the observations are properly taken into account, which is not the case in Eq. 2.23.

A GNSS phase observation reads (Hauschild, 2017a):

$$P_A^i = {\mathbf{e}_A^i}^{\mathrm{T}} \left(\mathbf{x}^i(t_A - \tau_A) - \mathbf{x}_A(t_A) \right) + c\,\delta t_A - c\,\delta t^i + \lambda\,N_A^i + T_A^i + I_A^i + \mathrm{PCV}_A^i + v_A^i \qquad (2.24)$$

where

P_A^i	is the carrier phase observation between antenna A and satellite i,
$\mathbf{e}_A^i$	is the line-of-sight vector,
$\mathbf{x}^i$	is the GNSS satellite position at signal emission time,
t_A	is the measurement epoch,
τ_A	is the signal travel time,
$\mathbf{x}_A$	is the position of the receiver antenna at signal reception,
c	is the speed of light,
δt_A	is the receiver clock error,
δt^i	is the satellite clock error,
λ	is the carrier wavelength,
N_A^i	is the integer phase ambiguity,
T_A^i	is the tropospheric delay,
I_A^i	is ionospheric delay,
PCV_A^i	is the Phase Centre Variation (PCV) and
v_A^i	is the zero-difference observation noise.

The observations of two antennas can be subtracted from each other in order to obtain a single-difference observation:

$$P_{AB}^i = P_B^i - P_A^i = {\mathbf{e}_B^i}^{\mathrm{T}} \left(\mathbf{x}^i(t_B - \tau_B) - \mathbf{x}_B(t_B) \right) - {\mathbf{e}_A^i}^{\mathrm{T}} \left(\mathbf{x}^i(t_A - \tau_A) - \mathbf{x}_A(t_A) \right)$$
$$+ c\,\delta t_B - c\,\delta t_A + \lambda\,N_{AB}^i + v_{AB}^i \qquad (2.25)$$

where

P_{AB}^i	is a phase single-difference between antenna A and B,
N_{AB}^i	is the single-difference ambiguity term and
v_{AB}^i	is the single-difference observation noise.

The satellite clock error as well as the tropospheric and ionospheric delays vanish as the baseline is assumed to be short. The PCV vanish hypothetically, if identical antennas are used (the following chapter will show that this assumption does not hold).

The baseline between antenna A and B, $\mathbf{b}_{AB}$, is defined as follows:

$$\mathbf{b}_{AB} = \mathbf{R}^{\mathrm{T}} \left(\mathbf{x}_A - \mathbf{x}_B \right) \tag{2.26}$$

where $\mathbf{b}_{AB}$ is the baseline vector between antennas A and B in the body frame and $\mathbf{R}$ is the attitude matrix from Eqs. 2.2 and 2.23. Assuming that:

i. The baseline is short and therefore $\mathbf{e}_A^i = \mathbf{e}_B^i$,

ii. The baseline is short and therefore $\tau_A = \tau_B$ and

iii. The receivers are synchronised and therefore $t_A = t_B$.

Introducing Eq. 2.26 into Eq. 2.25 leads to the final expression for the single-difference observation equation:

$$P_{AB}^i = P_B^i - P_A^i = \mathbf{e}^{i\,\mathrm{T}} \mathbf{R}\, \mathbf{b}_{AB} + c\, \delta t_B - c\, \delta t_A + \lambda\, N_{AB}^i + v_{AB}^i \tag{2.27}$$

The error which is induced due to approximation (i) is about:

$$\epsilon = b \sin \left(\arctan \frac{b}{2d} \right) \tag{2.28}$$

where

ϵ is the range error due to the approximation,

b is the length of the baseline and

d is the distance to the GNSS satellite.

Assuming a baseline length of 1 m and a distance to the GNSS spacecraft of 20 000 km, the range error amounts to $2.5 \cdot 10^{-8}$ m and is therefore negligible. The error due to approximation (ii) is always smaller than the length of the baseline divided by the speed of light. For a baseline length of 1 m, the resulting timing error never exceeds $3.3 \cdot 10^{-9}$ seconds and thus, can be neglected as well.
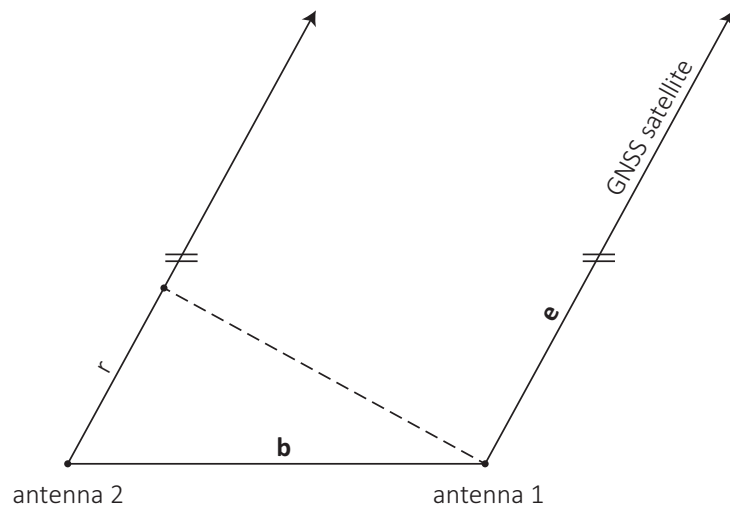
Figure 2.4.1 : Principle of GNSS attitude determination. **b** is the baseline, r is the range difference and **e** is the line-of-sight unit vector.

2.5 Extrapolation of the GNSS measurements

Eq. 2.27 is based on assumptions that are not valid onboard a fast vehicle equipped with non-synchronised receivers, for instance a spacecraft in LEO. As shown in Eq. 2.1, the velocity of such a spacecraft is approximately 8 km/s. Within a millisecond, which is the maximal synchronisation error, the spacecraft travels 8 m. That means that the receiver connected to antenna A performs the GNSS measurements up to 8 m further from the coordinates, where the receiver connected to antenna B performed its GNSS measurement. From this example, it is obvious that an extrapolation is necessary.

Assuming that $\mathbf{e}^i_A = \mathbf{e}^i_B = \mathbf{e}^i$, Eq. 2.25 can be simplified to lead to following expression.

$$P^i_{AB} = P^i_B - P^i_A = \mathbf{e}^{i\,\mathrm{T}} \left(\mathbf{x}^i(t_B - \tau_B) - \mathbf{x}_B(t_B) - \mathbf{x}^i(t_A - \tau_A) + \mathbf{x}_A(t_A) \right)$$
$$+ c\,\delta t_B - c\,\delta t_A + \lambda\,N^i_{AB} + v^i_{AB} \tag{2.29}$$

The attitude of the spacecraft does not appear explicitly in this last equation. Therefore, we introduce:

$$\mathbf{x}_A(t_A) = \mathbf{x}_A(t_A) + \mathbf{x}_A(t_{\mathrm{nom}}) - \mathbf{x}_A(t_{\mathrm{nom}}) \tag{2.30}$$

$$\mathbf{x}_B(t_B) = \mathbf{x}_B(t_B) + \mathbf{x}_B(t_{\mathrm{nom}}) - \mathbf{x}_B(t_{\mathrm{nom}}) \tag{2.31}$$

where t_{nom} is the nominal measurement epoch. Substitution of Eqs. 2.30 and 2.31 into Eq. 2.29 leads to:

$$P^i_{AB} = \mathbf{e}^{i\,\mathrm{T}} \left(\mathbf{x}^i(t_B - \tau_B) - \mathbf{x}_B(t_{\mathrm{nom}}) - \mathbf{x}^i(t_A - \tau_A) + \mathbf{x}_A(t_{\mathrm{nom}}) \right.$$
$$\left. - \mathbf{x}_B(t_B) + \mathbf{x}_B(t_{\mathrm{nom}}) + \mathbf{x}_A(t_A) - \mathbf{x}_A(t_{\mathrm{nom}}) \right)$$
$$+ c\,\delta t_B - c\,\delta t_A + \lambda\,N^i_{AB} + v^i_{AB} \tag{2.32}$$

At this state, the equation can be combined with Eq. 2.26 again, as $\mathbf{x}_A$ and $\mathbf{x}_B$ appear with the same time argument.

$$P^i_{AB} = \mathbf{e}^{i\,\mathrm{T}} \mathbf{R}(t_{\mathrm{nom}})\,\mathbf{b}_{AB} + E^i_{AB} + c\,\delta t_B - c\,\delta t_A + \lambda\,N^i_{AB} + v^i_{AB} \tag{2.33}$$

$$E^i_{AB} = \mathbf{e}^{i\,\mathrm{T}} \left(\mathbf{x}^i(t_B - \tau_B) - \mathbf{x}^i(t_A - \tau_A) - \mathbf{x}_B(t_B) + \mathbf{x}_B(t_{\mathrm{nom}}) + \mathbf{x}_A(t_A) - \mathbf{x}_A(t_{\mathrm{nom}}) \right) \tag{2.34}$$

where E^i_{AB} is the extrapolation term.

The coordinates of an antenna can be expressed relatively to the coordinates of the centre of mass of the spacecraft and the attitude of the spacecraft:

$$\mathbf{x}_A(t) = \mathbf{x}_{\mathrm{cm}}(t) + \mathbf{R}(t)\,\mathbf{b}_{\mathrm{cm},A} \tag{2.35}$$

where

$\mathbf{x}_A(t)$ are the coordinates of the antenna A,

$\mathbf{x}_{\mathrm{cm}}(t)$ are the coordinates of the centre of mass of the spacecraft,

$\mathbf{R}(t)$ is the attitude matrix of the spacecraft and

$\mathbf{b}_{\mathrm{cm},A}$ is the vector from the centre of mass of the spacecraft to antenna A.

Therefore:

$$\mathbf{x}_A(t_A) = \mathbf{x}_{\mathrm{cm}}(t_A) + \mathbf{R}(t_A)\,\mathbf{b}_{\mathrm{cm},A} \tag{2.36}$$

$$\mathbf{x}_A(t_{\mathrm{nom}}) = \mathbf{x}_{\mathrm{cm}}(t_{\mathrm{nom}}) + \mathbf{R}(t_{\mathrm{nom}})\,\mathbf{b}_{\mathrm{cm},A} \tag{2.37}$$

$$\mathbf{x}_B(t_B) = \mathbf{x}_{\mathrm{cm}}(t_B) + \mathbf{R}(t_B)\,\mathbf{b}_{\mathrm{cm},B} \tag{2.38}$$

$$\mathbf{x}_B(t_{\mathrm{nom}}) = \mathbf{x}_{\mathrm{cm}}(t_{\mathrm{nom}}) + \mathbf{R}(t_{\mathrm{nom}})\,\mathbf{b}_{\mathrm{cm},B} \tag{2.39}$$

Because the rotation rate of the satellite is small and the baselines are short, $\mathbf{R}(t_A) = \mathbf{R}(t_B) = \mathbf{R}(t_{\mathrm{nom}})$ can be assumed. The first order error introduced by this simplification is $\Delta\mathbf{x} = (t_B - t_A)\,\dot{\mathbf{R}}\,\mathbf{b}_{AB}$. For a baseline of 10 cm, the error is smaller than 2 μm for rates up to 1 degree per second.

Introducing this simplification and Eqs. 2.36 to 2.39 into Eq. 2.34 leads to the final expression for the extrapolation term:

$$E_{AB}^i = \mathbf{e}^{i\,\mathrm{T}}\left(\mathbf{x}^i(t_B - \tau_B) - \mathbf{x}^i(t_A - \tau_A) - \mathbf{x}_{\mathrm{cm}}(t_B) + \mathbf{x}_{\mathrm{cm}}(t_A)\right) \tag{2.40}$$

The first part of this expression can be calculated with the broadcast ephemeris (see for instance IS-GPS-200, 2015 for GPS broadcast ephemeris). The second half of this expression can be computed using the receiver navigation solution or any other PVT solution. The quality of the extrapolation will depend on the quality of the PVT estimation. The uncertainty in the line-of-sight propagates linearly with time. Assuming an accuracy of the velocity of 1 m/s and an extrapolation span of 1 ms, the accuracy of the extrapolation is 1 mm. In orbit, the accuracy of the u-blox velocity estimation is better than 10 cm/s, as reported in Hollenstein et al. (2014).

The velocity of a GNSS spacecraft can be computed using the broadcast ephemeris. The accuracy of GNSS spacecraft velocities derived in that way is around 1 mm/s for GPS (Zhang et al., 2006) and therefore negligible compared to the accuracy of the PVT solution.

2.6 Practical aspects of GNSS measurement extrapolation with Bernese

The Bernese GNSS Software V5.2 (Dach et al., 2015) was used to generate synthetic data. Bernese is a widely used and well established GNSS processing and analysis software. It has a more than 30 years long history. However, the processing of very fast stations with non-synchronised receivers was originally not foreseen. In order to obtain reliable results, some minor software

modifications had to be performed. These changes are documented here. The modifications were validated by performing a comparison in Matlab. After the software modifications, the synthetic observations are consistent to 10^{-6} m for LEO spacecraft.

In Bernese, `GTLEOCO.f` is the subroutine which allows to retrieve the coordinates of the centre of mass of a LEO spacecraft in different coordinate systems, `LEOSKY.f90` computes distance, azimuth and elevation to GNSS satellites as seen from a LEO spacecraft and `SMPRNG.f` is the actual range simulation routine. Table 2.6.1 holds a summary of the performed changes.

The main obstacle is the limited precision of the internal time representation. A Fortran double is used for the representation of epochs, thus providing 15 digits. Because the time is saved as a fractional Modified Julian Date (MJD), five digits are used for the integer part. Ten digits are left for the fractional part of a day (which counts $86\,400$ seconds), leading to a time resolution of only $86\,400 \text{ s} \cdot 10^{-10} = 8.64 \ \mu\text{s}$. This is insufficient to precisely position a spacecraft with a speed of 8 km/s. A workaround consists of using the receiver clock error in `SMPRNG.f`, which is in seconds, to hold the difference to the actual time and thus compensating the truncation error due to the time representation in MJD.

Another change is the addition of the second order term in the position computation of the LEO satellite in `LEOSKY.f90`. Finally, a new function is added in order to check whether a signal is obstructed by the Earth or not. This feature was not present, as it is not necessary when generating synthetic observations for stations with an antenna always pointing in zenith direction. This is the case for stations on Earth, but also for GNSS antennas onboard satellites with sophisticated attitude control.

Table 2.6.1 : Summary of modifications to the Bernese GNSS Software.

Subroutine	Performed changes
`GTLEOCO.f`	Modified call of `COOTRA`
`LEOSKY.f90`	Added second order term in the position computation of the LEO satellite
`SMPRNG.f`	Modified call of `XYZTIM`
	Modified call of `TRUEEARTH`
	Modified call of `LEOSKY`
	Correction of the rounding error due to the time representation in MJD
	Computation of Earth shadowing of signals and removal of those

2.7 Phase ambiguity resolution

Eq. 2.33 is still affected by an unknown integer phase ambiguity N_{AB}^i. In order to solve for phase ambiguities, a double-difference solution is computed. At this stage, phase ambiguities can most easily be resolved to integer numbers. Instantaneous methods are simple in the implementation, but provide lower ambiguity resolution success rates. Methods using several epochs show better success rates, but are sensitive to phase cycle slips. These must be detected and corrected or dealt with properly in order not to bias the ambiguity resolution process.

Ambiguity resolution has been extensively studied in the past. A general introduction to ambiguity resolution is provided in Teunissen (2017). The most prominent algorithm is the so-called LAMBDA algorithm (Teunissen, 1995). In the case of ambiguity resolution for attitude determination, prior information about the geometry of the antenna system can be provided to the adjustment as pseudo-observations or as constraints and help to reduce the ambiguity search space and do increase the ambiguity resolution success rate. Such algorithms were presented in Park and Teunissen (2003) or Teunissen (2010) and successfully employed in different use-cases (Teunissen et al., 2011). Ambiguity resolution for attitude determination is also presented in Giorgi (2017, pp. 793–798).

In the case of the CubETH spacecraft, the simplest implementation proved to be very efficient. An approximation for the carrier phase ambiguities was generated by setting the baseline length to zero at double-difference level. The double-difference can for instance be derived from Eq. 2.33:

$$P_{AB}^{ij} = \left(\mathbf{e}^j - \mathbf{e}^i \right)^{\mathrm{T}} \mathbf{R}\, \mathbf{b}_{AB} + E_{AB}^{ij} + \lambda\, N_{AB}^{ij} + v_{AB}^{ij} \tag{2.41}$$

where

$$\begin{aligned}
&P_{AB}^{ij} && \text{is the double-difference phase observation,} \\
&E_{AB}^{ij} && \text{is the double-difference extrapolation term,} \\
&N_{AB}^{ij} && \text{is the double-difference phase ambiguity and} \\
&v_{AB}^{ij} && \text{is the double-difference observation residual.}
\end{aligned}$$

The receiver clock vanishes, as every antenna observes two GNSS satellites at exactly the same time. The approximation for the phase ambiguity is:

$$\widetilde{N}_{AB}^{ij} = P_{AB}^{ij} - E_{AB}^{ij} \tag{2.42}$$

Strictly spoken, this approximation is only valid for baselines shorter than half a wavelength or approximatively 10 cm. The true ambiguity must then lie in the interval $[-1, 1]$ around $\widetilde{N}_{AB}^{ij}$ (Van Graas and Braasch, 1991). As this search space is very narrow, it can easily be fully searched through. The size of the search space for single-frequency receivers is:

$$n_{\text{candidates}} = 3^{\,n_{\text{satellites}} - 1} \tag{2.43}$$

where $n_{\text{candidates}}$ is the number of candidates in total and $n_{\text{satellites}}$ is the number of satellites. If the baseline length is significantly increased, other search strategies, as mentioned before, have to be used.

2.8 Filter formulation

In the absence of a strong attitude control, a spacecraft will have a very regular attitude and typically constant turn rates. This dynamics predestines the Kalman filter for the estimation of the attitude. Details on the Kalman filter can be found in Welch and Bishop (2006). Two successive states are linked by a process:

$$\mathbf{x}_s = \mathbf{f}(\mathbf{x}_{s-1}) + \mathbf{u}_{s-1} \tag{2.44}$$

$$\mathbf{u}_{s-1} \sim N(0, \mathbf{U}_{s-1}) \tag{2.45}$$

where

$$
\begin{array}{ll}
\mathbf{x}_s & \text{is the state at the epoch } s, \\
\mathbf{f} & \text{is the state transition function,} \\
\mathbf{x}_{s-1} & \text{is the state at the epoch } s-1, \\
\mathbf{u}_{s-1} & \text{is the process noise and} \\
\mathbf{U}_{s-1} & \text{is the process noise variance-covariance.}
\end{array}
$$

The observation equation reads as follows.

$$\mathbf{z}_s = \mathbf{h}(\mathbf{x}_s) + \mathbf{v}_s \tag{2.46}$$

$$\mathbf{v}_s \sim N(0, \mathbf{V}_s) \tag{2.47}$$

where

$$
\begin{array}{ll}
\mathbf{z} & \text{is the observation vector,} \\
\mathbf{h} & \text{is the observation function,} \\
\mathbf{v} & \text{is the observation noise and} \\
\mathbf{V} & \text{is the observation variance-covariance.}
\end{array}
$$

The filter update step is given by:

$$\widehat{\mathbf{x}}_s^- = \mathbf{f}(\widehat{\mathbf{x}}_{s-1}) \tag{2.48}$$

$$\mathbf{P}_{s-1}^- = \mathbf{F}_{s-1}\,\mathbf{P}_{s-1}\,\mathbf{F}_{s-1}^{\mathrm{T}} + \mathbf{U}_{s-1} \tag{2.49}$$

$$F_{ij} = \frac{\partial f_i(\mathbf{x})}{\partial x_j} \tag{2.50}$$

$\widehat{\mathbf{x}}_s^-$ is the propagated state, $\widehat{\mathbf{x}}_{s-1}$ is the state estimate of the previous epoch, $\mathbf{P}_{s-1}^-$ is the propagated state variance-covariance, $\mathbf{F}_{s-1}$ is the matrix of partial derivatives and $\mathbf{P}_{s-1}$ is the variance-covariance of the state estimate of epoch $s - 1$. The filter measurement update reads as:

$$\mathbf{K}_s = \mathbf{P}_s^- \, \mathbf{H}_s^{\mathrm{T}} \left(\mathbf{H}_s \, \mathbf{P}_s^- \, \mathbf{H}_s^{\mathrm{T}} + \mathbf{V}_s \right) \tag{2.51}$$

$$\widehat{\mathbf{x}}_s = \widehat{\mathbf{x}}_s^- + \mathbf{K}_s \left(\mathbf{z}_s - \mathbf{h}(\widehat{\mathbf{x}}_s^-) \right) \tag{2.52}$$

$$\mathbf{P}_s = (\mathbf{I} - \mathbf{K}_s \, \mathbf{H}_s) \, \mathbf{P}_s^- \tag{2.53}$$

$$H_{ij} = \frac{\partial h_i(\mathbf{x})}{\partial x_j} \tag{2.54}$$

where

$\mathbf{K}_s$ is the Kalman gain matrix,

$\mathbf{H}_s$ is the matrix of partial derivatives,

$\widehat{\mathbf{x}}_s$ is the estimated state and therefore the result of the Kalman filter and

$\mathbf{P}_s$ is the variance-covariance matrix of this state.

2.8.1   State propagation

The Kalman filter state vector is composed of the quaternion $\mathbf{q}$ and the turn rates $\boldsymbol{\omega}$ and reads as follows:

$$\underset{7 \times 1}{\mathbf{x}} = \begin{pmatrix} \mathbf{q} \\ \boldsymbol{\omega} \end{pmatrix} = \begin{pmatrix} q_0 & q_1 & q_2 & q_3 & \omega_1 & \omega_2 & \omega_3 \end{pmatrix}^{\mathrm{T}} \tag{2.55}$$

As the spacecraft is symmetrical, it is expected to have very regular turn rates. Furthermore, no information about the attitude control (e.g. torques) is available. Therefore, a very simple dynamical model has been chosen:

$$\mathbf{x}_s = \mathbf{x}_{s-1} + (t_s - t_{s-1}) \, \dot{\mathbf{x}}_{s-1} \tag{2.56}$$

$$= \begin{pmatrix} \mathbf{q} \\ \boldsymbol{\omega} \end{pmatrix}_{s-1} + (t_s - t_{s-1}) \begin{pmatrix} \dot{\mathbf{q}} \\ \mathbf{0} \end{pmatrix}_{s-1} \tag{2.57}$$

where $(t_s - t_{s-1})$ is the time between two successive epochs. This model assumes constant turn rates.

2.8.2 Stochastic model

The associated stochastic model can be derived starting from the state-space equation. It is assumed, that the process noise affects the system only depends on the rotation rates, leading to:

$$\dot{\mathbf{x}}(t) = \begin{pmatrix} \dot{\mathbf{q}}(t) \\ \dot{\boldsymbol{\omega}}(t) \end{pmatrix} = \mathbf{a}(\mathbf{x}(t)) + \mathbf{G}\,\mathbf{w}(t) \tag{2.58}$$

$$= \begin{pmatrix} \dot{\mathbf{q}}(\mathbf{q}(t), \boldsymbol{\omega}(t)) \\ \mathbf{0}_{3\mathrm{x}1} \end{pmatrix} + \begin{pmatrix} \mathbf{0}_{4\mathrm{x}3} \\ \mathbf{I}_3 \end{pmatrix} \begin{pmatrix} \mathrm{w}_1(t) \\ \mathrm{w}_2(t) \\ \mathrm{w}_3(t) \end{pmatrix} \tag{2.59}$$

where

$\dot{\mathbf{x}}$ is the time derivative of the state,

$\mathbf{a}(\mathrm{x})$ is the system model function,

$\mathbf{G}$ is the noise shaping matrix and

$\mathbf{w}$ is the white noise entering the system.

After linearisation, this function reads:

$$\delta\dot{\mathbf{x}} = \mathbf{A}\,\delta\mathbf{x} + \mathbf{G}\,\mathbf{w} \tag{2.60}$$

$$\delta\dot{\mathbf{x}} = \dot{\mathbf{x}} - \mathbf{g}(\mathbf{x}_0) \tag{2.61}$$

$$\delta\mathbf{x} = \mathbf{x} - \mathbf{x}_0 \tag{2.62}$$

$$A_{ij} = \frac{\partial a_i(\mathbf{x_0})}{x_j} \tag{2.63}$$

where $\mathbf{A}$ is the Jacobian matrix of the function $\mathbf{a}$ and $\mathbf{x}_0$ is the linearisation point. The solution to the differential equation 2.60 reads:

$$\delta\mathbf{x}(t) = e^{(t-t_0)\mathbf{A}}\,\delta\mathbf{x}(t_0) + \int_{t_0}^{t} e^{(t'-t_0)\mathbf{A}}\,\mathbf{G}\,\mathbf{w}(t')\,\mathrm{d}t'$$

$$= e^{(t-t_0)\mathbf{A}}\,\delta\mathbf{x}(t_0) + \mathbf{u} \tag{2.64}$$

Assuming that $\mathbf{w}$ is a stationary white noise process and that all three components have the same standard deviation, variance-covariance propagation can be applied to obtain the variance-covariance of the propagated state:

$$\mathbf{U} = \int_{t_0}^{t} e^{(t'-t_0)\mathbf{A}}\,\mathbf{G}\,\mathbf{I}_3\,\sigma_w^2\,\mathbf{I}_3\,\mathbf{G}^{\mathrm{T}}\left(e^{(t'-t_0)\mathbf{A}}\right)^{\mathrm{T}}\mathrm{d}t' \tag{2.65}$$

where $\mathbf{U}$ is the Kalman filter process noise (see Eq. 2.45) and σ_w^2 is the noise variance. Integration

of this equation leads to an analytical formula for $\mathbf{U}$:

$$\mathbf{U} = \sigma_w^2 \begin{pmatrix} \boldsymbol{\Theta} & \boldsymbol{\Omega} \\ \boldsymbol{\Theta}^{\mathrm{T}} & \Delta t\,\mathbf{I}_3 \end{pmatrix} \tag{2.66}$$

$$\boldsymbol{\Theta} = \frac{\Delta t^3}{12} \begin{pmatrix} q_1^2 + q_2^2 + q_3^2 & -q_0\,q_1 & -q_0\,q_2 & -q_0\,q_3 \\ -q_0\,q_1 & q_0^2 + q_2^2 + q_3^2 & -q_1\,q_2 & -q_1\,q_3 \\ -q_0\,q_2 & -q_1\,q_2 & q_0^2 + q_1^2 + q_3^2 & -q_2\,q_3 \\ -q_0\,q_3 & -q_1\,q_3 & -q_2\,q_3 & q_0^2 + q_1^2 + q_2^2 \end{pmatrix} \tag{2.67}$$

$$\boldsymbol{\Omega} = \frac{\Delta t^2}{4} \begin{pmatrix} -q_1 & -q_2 & -q_3 \\ q_0 & q_3 & -q_2 \\ -q_3 & q_0 & q_1 \\ q_2 & -q_1 & q_0 \end{pmatrix} \tag{2.68}$$

where Δt is the time interval between two epochs and q_i is the ith element of the quaternion. The stochastic model of the double-difference observations $\mathbf{V}$ is simply obtained after application of variance-covariance propagation:

$$\mathbf{V} = \mathbf{D}\,\mathbf{Q}_{ll}\,\mathbf{D}^{\mathrm{T}} \tag{2.69}$$

where $\mathbf{D}$ is the differencing operator leading to double-difference observations and $\mathbf{Q}_{ll}$ is the variance-covariance matrix of the zero-difference observations. If equal weighting of all observations is assumed, Eq. 2.69 becomes:

$$\mathbf{V} = \mathbf{D}\,\mathbf{I}_n\,\sigma_p^2\,\mathbf{I}_n\,\mathbf{D}^{\mathrm{T}} \tag{2.70}$$

where σ_p^2 is the zero-difference observation variance and n is the number of zero-difference observations.

2.9 Outlook

Unfortunately, the CubETH project was not continued, giving us no opportunity to pursue the development of the algorithm. The present work is a solid base. It could easily be enhanced with outlier detection, a robust initialization and a more powerful ambiguity resolution algorithm. These three topics were extensively studied in the past and do not represent novel scientific issues.

The next step after the synchronisation of the receivers is the modelling of the Phase Centre Calibrations (PCC). Because of the short baselines, any uncorrected PCV has a huge impact on the accuracy. This topic is addressed in the next chapters.

Chapter 3

GNSS Antenna Calibration

GNSS antennas are a key factor in GNSS measurements. Antennas transform incoming electromagnetic signals into voltage. They are an essential part of any Satellite Navigation System, as they are the interface between the GNSS signals and the receiver. A very good introduction to GNSS antennas is provided in Maqsood et al. (2017) and in Rao et al. (2013).

Antennas are not perfect and are therefore subject to errors. When measuring coordinates with a GNSS antenna, the coordinates refer to a mechanical point on the antenna, the Antenna Reference Point (ARP). Usually, the intersection of the lowest horizontal surface of the antenna with the vertical symmetry axis is defined as ARP. An updated list of the ARP for the most common antennas including technical drawings is provided by the antenna working group (AGW) of the International GNSS Service (IGS).[1]

The electronic centre of the antenna is not located in the ARP. Therefore, Phase Centre Offsets (PCO) were introduced. The PCO is the vector from the ARP to the so-called Mean Phase Centre (MPC). The MPC is a purely conventional point, as the measurement locations of the incoming electromagnetic waves never meet in a single point. First theoretical considerations for interferometric baseline measurements were made already at the end of the seventies (Counselman and Shapiro, 1979). Very soon, phase centre calibrations were studied, attempted and achieved (Sims, 1985; Geiger, 1988; Tranquilla and Colpitts, 1989).

The result of a successful calibration is a map of the so-called Phase Centre Variations (PCV), which are corrections that are added on top of the PCO. PCV are typically in the range of several millimetres (Rothacher, 2001), but can reach centimetre level for miniaturized low-cost antennas. Although this nomenclature is a bit confusing, as the MPC is arbitrary and the PCV directly depends on the chosen PCO, this convention is still widely used in the antenna calibration community after its introduction in the early nineties (Geiger, 1990). Nowadays, the term Phase Centre Correction (PCC) should be used to designate calibrations that include PCO and PCV.

---

[1]Antenna information file of the IGS AWG, `ftp://igs.org/pub/station/general/antenna.gra`.

The present chapter describes antenna calibration in general, the parametrisation of PCC and the underlying estimation theory. Chapter 4 presents the relative field calibration approach tailored to the calibration of attitude determination systems. Robot specific questions are addressed in Chapter 5, followed by Chapter 6 on absolute field calibrations using a robot.

3.1 Definitions

Within the present document, following nomenclature is adopted.

> **Phase Centre Correction (PCC)** is the total correction to be applied to the measured range in order to obtain the coordinates of the Antenna Reference Point (ARP). The PCC is divided into:
>
>   i. The **Phase Centre Offset (PCO)**, which is the vector from the ARP to the Mean Phase Centre (MPC), an arbitrary point and
> ii. The **Phase Centre Variation (PCV)**, which is the actual direction dependent correction function.

Generally, the MPC is chosen in such a way that the PCV is minimized. However, various different conventions exist (see for instance in Dach et al. 2015, pp. 404–405). The obtained MPC is dependent on the weighing of the observations and on the elevation cut-off angle. Therefore, the PCC is the only meaningful quantity. The comparison of two or several antenna calibrations should always be based on a comparison of the PCC. Figure 3.1.1 illustrates the relationship between the different quantities.

3.2 State of the art

Antenna calibration procedures can be divided into three categories: (Görres et al., 2006; Rothacher, 2001)

  i. Relative field calibration.
 ii. Absolute calibration:

    a. Anechoic chamber calibration.

    b. Absolute field calibration using a robot.

Antenna calibrations are performed routinely worldwide by a dozen of groups. German institutions were particularly active in GNSS antenna calibration. A GNSS antenna calibration workshop was held annually in Germany from 1999 to 2009.[2] Nowadays, German institutions

---

[2]GNSS antenna workshops, University of Bonn, 10.03.2019, `https://www.gib.uni-bonn.de/team/lehrbeauftragte/bgoerres/antennen-workshops`
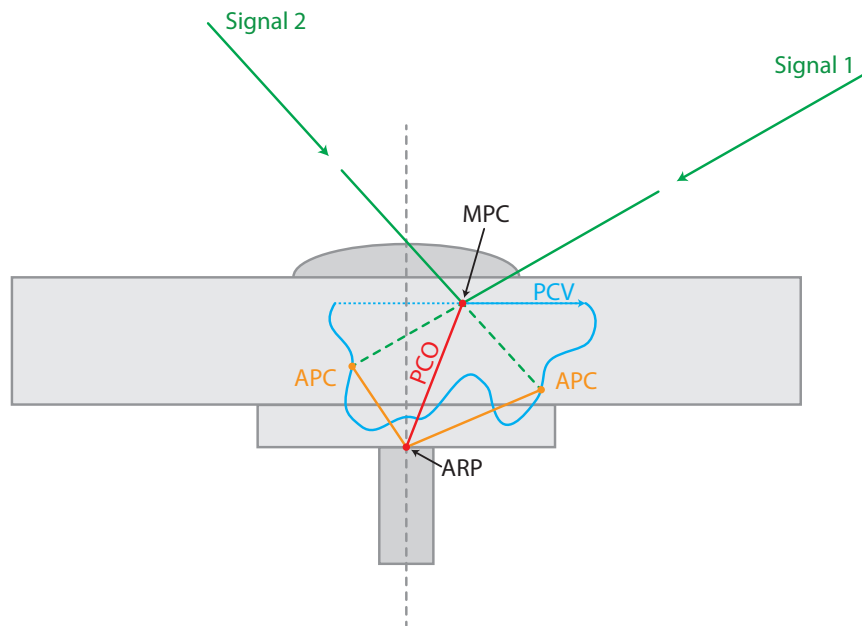
Figure 3.1.1 : Illustration of the relevant quantities in antenna calibration. The Antenna Reference Point (ARP) is the mechanical reference of the antenna. The Phase Centre Offset (PCO) is the vector from the ARP to the Mean Phase Centre (MPC). The MPC is purely conventional and can be arbitrarily chosen. The actual direction dependent correction, the Phase Centre Variation (PCV), is added on top of the PCO, leading to the Apparent Phase Centre (APC). The Phase Centre Correction is the projection of the vector from the ARP to the APC (drawn in orange) onto the line-of-sight.

are still leading in this field, as is shown in the following sections. German speaking practitioner can find general information on antenna calibrations in Görres et al. (2018).

Various studies show that the results from different techniques agree well for the first GPS frequency (L1), typically below the millimetre level, but some improvements are possible for GPS L2 (Görres et al., 2006; Bilich et al., 2012).

The repeatability within each technique is very well documented for robot calibrations (Schmitz et al., 2002; Wübbena et al., 2003) and for anechoic chamber measurements (Zeimetz and Kuhlmann, 2008).

3.2.1 Relative field calibration

In relative field calibration (Rothacher et al., 1995), a short baseline is set up and data is collected over a period of at least one day. The first antenna of the baseline is the reference antenna. It can either have perfectly known PCC or arbitrarily been set to zero. The second antenna of the baseline is the uncalibrated antenna. During the estimation, a PCC function is fit through the residuals, resulting in estimates of the station coordinates and of the PCC.

In order to decorrelate the PCO from the station coordinates, the antenna can be rotated around its vertical axis of symmetry. Typically, four sessions with four different azimuths are recorded, every session lasting for one hour. The vertical component of the PCO will still correlate to 100% with the station height and needs to be constrained to a known value. This value can be determined with terrestrial surveying methods (levelling). Alternatively, all three components of the station position can be surveyed and fixed. In this case, only the PCC are set up as parameters. The antenna still needs to be rotated, in order to probe the entire antenna hemisphere and thus filling the north or the south hole respectively. These are the sections of the sky which are never occupied by any GNSS satellite due to the inclination of the GNSS orbits.

The relative field calibration method is illustrated in Chapter 4 based on the very specific use-case of a GNSS attitude determination system.

3.2.2 Anechoic chamber calibration

In anechoic chamber measurements (Sims, 1985; Tranquilla and Colpitts, 1989; Schupler et al., 1994; Zeimetz, 2010), the GNSS antenna is set up in an anechoic chamber together with a signal source. The signal is received by the antenna and interfered with the original signal, leading to a measurement of the phase shifts. Either the antenna is rotated or the sender is moved in order to scan the antenna hemisphere. This will produce a map of phase shifts. Anechoic chamber measurements are not affected by multipath and realise a very pure form of antenna calibration. In return, the infrastructure is very demanding and the synchronisation of all the equipment is difficult to achieve.

Currently, the University of Bonn is the only institution having been approved by the IGS to deliver chamber calibrations.[3]

3.2.3 Absolute field calibration

Absolute field calibrations use a device to rotate the antenna around at least two axes. Calibrations currently being undertaken make use of 2-axis robots (Bilich and Mader, 2010) or robots with five or more axes (Wübbena et al., 2000; Menge, 2003; Kersten, 2014; Riddell et al., 2015; Hu et al., 2015). The actuator rotates the antenna into different orientations, and therefore decorrelates the PCC from the station coordinates.

Furthermore, the rotation allows to sample the antenna hemisphere much more efficiently. As a consequence, an elevation mask can be applied. All low-elevation signals, for instance below 20 degrees elevation, are removed. Because the antenna is inclined towards all possible directions by the robotic arm, reliable data can be collected even for low elevations in the antenna specific coordinate system. In other words, the entire antenna hemisphere is sampled. As the calibration procedure does not rely on low elevations anymore, multipath is mitigated.

The most sophisticated systems use a robot with five or more axes. The advantage is that the coordinates of the antenna can be kept fixed during the calibration. The first robotic calibration system was developed by the University of Hanover and the German company Geo++® GmbH (Wübbena et al., 2000; Menge, 2003; Dilßner, 2008; Kersten, 2014). These two institutions and the Landeskalibriereinrichtung of the Senatsverwaltung für Stadtentwicklung Berlin are the only institutions performing robot type calibrations and being currently approved by the IGS AWG.[3]

Other groups are currently setting up robotic calibration systems with six axes as well, namely Wuhan University (Hu et al., 2015), Geoscience Australia (Riddell et al., 2015) and the US American National Geodetic Survey (NGS; Bilich et al., 2018). The system developed at ETH Zurich and related scientific questions are discussed in Chapter 6.

---

[3]Readme file of the IGS AWG, 27.11.2018, `ftp://igs.org/pub/station/general/antenna_README.pdf`.

3.3 Phase Centre Correction Model

A GNSS phase observation reads (Hauschild, 2017a):

$$P_A^i = {\mathbf{e}_A^i}^{\mathrm{T}} \left(\mathbf{x}^i - \mathbf{x}_{A,\mathrm{MPC}} \right) + c\,\delta t_A - c\,\delta t^i + \lambda\,N_A^i + \mathrm{PCV}_A^i + v_A^i \tag{3.1}$$

where

P_A^i	is the carrier phase observation between antenna A and satellite i,
$\mathbf{e}_A^i$	is the line-of-sight vector,
$\mathbf{x}^i$	is the GNSS satellite position at signal emission,
$\mathbf{x}_{A,\mathrm{MPC}}$	is the position of the receiver antenna MPC at signal reception,
c	is the speed of light,
δt_A	is the receiver clock error,
δt^i	is the satellite clock error,
λ	is the carrier wavelength,
N_A^i	is the integer phase ambiguity,
PCV_A^i	is the PCV and
v_A^i	is the zero-difference observation noise.

Atmospheric delays (ionosphere and troposphere) and relativistic corrections were neglected in this latest equation. The PCV in Eq. 3.1 is modelled as an azimuth and zenith angle dependent correction as follows:

$$\mathrm{PCV}_A^i = \mathrm{PCV}_A(\alpha^i, z^i) \tag{3.2}$$

where α^i is the azimuth angle of the GNSS satellite in the antenna-fixed coordinate system and z^i is the zenith angle. The coordinates of the conventional MPC are obtained after application of the PCO to the geometrical reference of the antenna, the ARP, as follows:

$$\mathbf{x}_{\mathrm{MPC}} = \mathbf{x}_{\mathrm{ARP}} + \mathbf{PCO} \tag{3.3}$$

where $\mathbf{x}_{\mathrm{ARP}}$ is the position of the ARP and $\mathbf{PCO}$ is the PCO vector. Substitution of Eq. 3.3 into Eq. 3.1 and rearranging leads to:

$$P_A^i = {\mathbf{e}_A^i}^{\mathrm{T}} \left(\mathbf{x}^i - \mathbf{x}_{A,\mathrm{ARP}} \right) + c\,\delta t_A - c\,\delta t^i + \lambda\,N_A^i + \mathrm{PCV}_A^i - {\mathbf{e}^i}^{\mathrm{T}}\,\mathbf{PCO} + v_A^i \tag{3.4}$$

The PCV and the PCO term can be grouped into one term, the PCC. The total correction applied on top of the raw measurements is not affected:

$$\mathrm{PCC}_A^i = \mathrm{PCV}_A^i - {\mathbf{e}^i}^{\mathrm{T}}\,\mathbf{PCO} \tag{3.5}$$

where PCC_A^i is the total range correction or PCC and $\mathbf{e}^i$ is the line-of-sight (LOS; positively

pointing towards the GNSS spacecraft). The negative sign in Eq.3.5 emerges due to the ANTEX sign convention (Rothacher and Schmid, 2010) and the choice of the direction of $\mathbf{e}^i$. A PCV can always be transformed to any other PCO by the following relation:

$$\text{PCV}'_A(\alpha^i, z^i) = \text{PCV}_A(\alpha^i, z^i) + \mathbf{e}^{i\,\text{T}} \left(\mathbf{PCO}' - \mathbf{PCO} \right) \tag{3.6}$$

where $\text{PCV}'_A(\alpha^i, z^i)$ is the PCV belonging to the offsets $\mathbf{PCO}'$ and $\text{PCV}_A(\alpha^i, z^i)$ is the PCV belonging to the offsets $\mathbf{PCO}$. In both cases, the total PCC is identical. PCV and PCO must always be used consistently.

3.4 Phase Centre Parametrisations

Grid parametrisations with piecewise linear interpolation between the grid points and spherical harmonics are the two most common types of PCC parametrisations. The different methods will shortly be discussed hereafter.

3.4.1 Grid parametrisation

The PCC is represented as a regular grid covering the antenna hemisphere. A typical resolution for an antenna pattern is 5 times 5 degrees. PCC values are available in a look-up table for every point in the grid. The number of parameters equals:

$$n_{\text{parameters}} = \left(\frac{90}{\Delta z} + 1 \right) \frac{360}{\Delta \alpha} \qquad [\text{deg}] \tag{3.7}$$

where $n_{\text{parameters}}$ is the number of grid points, Δz is the vertical resolution in degrees and $\Delta \alpha$ is the azimuthal resolution in degrees.

In the estimation process, the grid has to be constrained, because its constant part correlates with the receiver clock (as can be seen for instance in Eq. 2.24). One way to make the system regular is to constrain the PCC values at zenith to zero. This is very convenient, as the zenith values have to be constrained in any case, as all points located in the zenith have the same value. This operation reduces the degree of freedom of the system, leading to a final degree of freedom of:

$$n_{\text{parameters}} = \frac{90}{\Delta z} \cdot \frac{360}{\Delta \alpha} \qquad [\text{deg}] \tag{3.8}$$

In the case of the standard resolution of 5 degrees times 5 degrees, this represents 1296 parameters. The PCC between the grid points are obtained after two linear interpolations, one in zenith

angle and one in azimuth. These two linear interpolations, combined into one equation, read:

$$\text{PCC}(\alpha_0, z_0) = w_1 \, \text{PCC}(\alpha_i, z_i) + w_2 \, \text{PCC}(\alpha_{i+1}, z_i)$$

$$+ w_3 \, \text{PCC}(\alpha_i, z_{i+1}) + w_4 \, \text{PCC}(\alpha_{i+1}, z_{i+1}) \tag{3.9}$$

$$w_1 = 1 - r_\alpha - r_z + r_\alpha \, r_z \tag{3.10}$$

$$w_2 = r_\alpha - r_\alpha \, r_z \tag{3.11}$$

$$w_3 = r_z - r_\alpha \, r_z \tag{3.12}$$

$$w_4 = r_\alpha \, r_z \tag{3.13}$$

$$r_\alpha = \frac{\alpha_0 - \alpha_i}{\alpha_{i+1} - \alpha_i} \tag{3.14}$$

$$r_z = \frac{z_0 - z_i}{z_{i+1} - z_i} \tag{3.15}$$

where $\text{PCC}(\alpha_0, z_0)$ is the interpolated PCC and α_i, z_i, α_{i+1} and z_{i+1} are the coordinates of the grid points (see Figure 3.4.1). This formulation is equivalent to performing two linear interpolations, one in azimuth and one in zenith angle.

The drawback of this approach is the large distortions that appear close to zenith. The grid parametrisation is inherently a representation of values on a plane. In contrast, spherical harmonics are perfectly suited to represent scalar values on a sphere and should therefore be preferred, if no evidence speaks against it.

3.4.2   Grid partial derivatives

After omission of the arguments α and z, Eq. 3.9 reads:

$$\text{PCC} = w_1 \, \text{PCC}_1 + w_2 \, \text{PCC}_2 + w_3 \, \text{PCC}_3 + w_4 \, \text{PCC}_4 \tag{3.16}$$

The partial derivatives are trivial:

$$\frac{\partial \text{PCC}}{\partial \text{PCC}_1} = w_1 \tag{3.17}$$

$$\frac{\partial \text{PCC}}{\partial \text{PCC}_2} = w_2 \tag{3.18}$$

$$\frac{\partial \text{PCC}}{\partial \text{PCC}_3} = w_3 \tag{3.19}$$

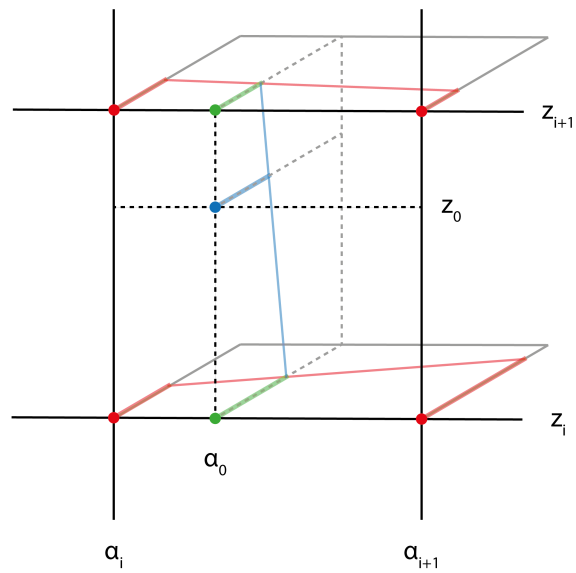$$\frac{\partial \text{PCC}}{\partial \text{PCC}_4} = w_4 \tag{3.20}$$

Figure 3.4.1 : Principle of the grid interpolation. The actual parameters are the values at the grid intersection points, marked in red. An interpolation along the azimuth (resulting in the green values) is followed by an interpolation along the zenith, resulting in the value at the requested azimuth and elevation (in blue). Source: Willi et al. (2018a).

3.4.3 Spherical harmonics parametrisation

The phase centre correction, expressed as spherical harmonics, read as:

$$\text{PCC}(\alpha^i, z^i) = \sum_{n=0}^{n_{max}} \sum_{m=0}^{n} \widetilde{P}_{nm}(\cos z^i) \left(a_{nm} \cos(m\,\alpha^i) + b_{nm} \sin(m\,\alpha^i) \right) \tag{3.21}$$

where

$$\begin{aligned}
&n && \text{is the degree and} \\
&m && \text{is the order of the spherical harmonics series,} \\
&\widetilde{P}_{nm} && \text{are the normalized associated Legendre polynomials,} \\
&a_{nm} && \text{are the spherical harmonics cosine coefficients and} \\
&b_{nm} && \text{are the spherical harmonics sine coefficients.}
\end{aligned}$$

The typical resolution for spherical harmonics PCC is degree and order 8 or degree and order 12. The total number of parameter equals:

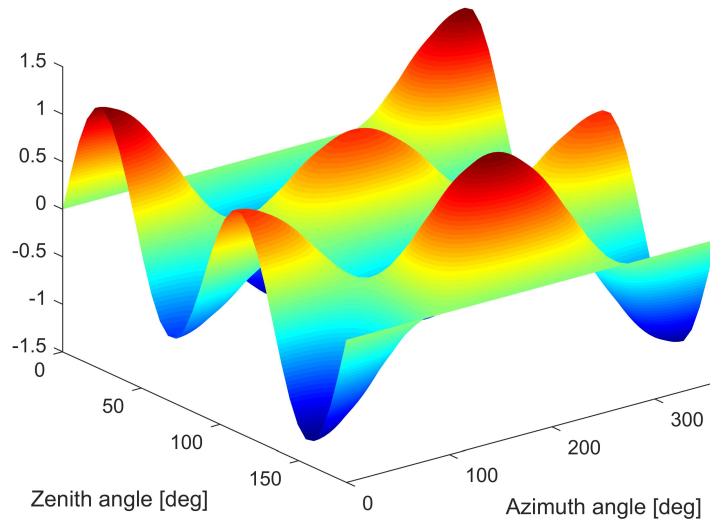$$n_{\text{parameters}} = (n+1)\,(m+1) \tag{3.22}$$

This count excludes all coefficients b_{n0}, because their contribution equals zero, as $\sin 0 = 0$. Exactly as in the case of the grid parametrisation, the inversion of the unconstrained system will lead to singularities. The absolute term a_{00} correlates with the receiver clock parameter and is constrained to zero (see Figure 3.4.2). The parameters a_{10}, a_{11} and b_{11} fully correlate with the PCO components. Therefore, no explicit PCO parameters are necessary in the PCC model.

Because no measurements are available for the lower hemisphere of the antenna, a symmetry assumption has to be made. If symmetry is assumed between the upper and the lower antenna hemisphere, all coefficients that represent a function with an odd number of zeros between $z = 0$ deg and $z = 180$ deg along z (called odd coefficients hereafter) have to be constrained to zero. This is the case if $n - m$ is odd (see Figure 3.4.2). Figure 3.4.3 illustrates odd and even coefficients of spherical harmonics.
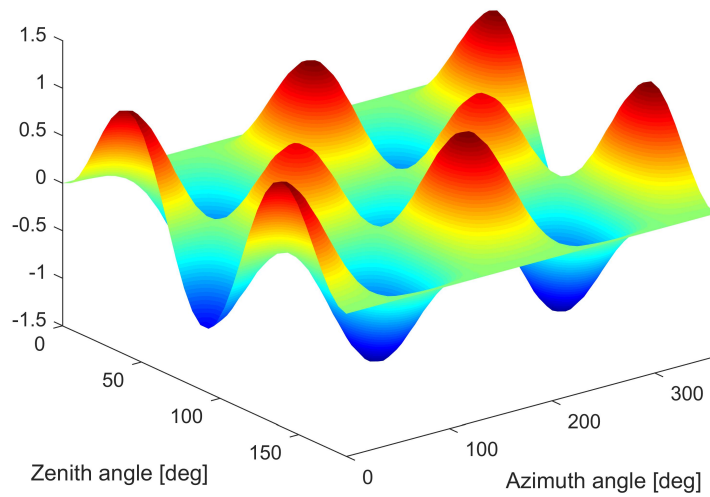
Assuming that $n = m$ and that all odd coefficients but a_{10}, a_{11} and b_{11} are constrained to zero, the total number of parameters reads (Willi et al., 2018a):

$$n_{\text{parameters}} = \frac{(n+2)\,(n+1)}{2} \tag{3.23}$$

This leads to 91 parameters for a degree and order 12 expansion and 45 parameters for a degree and order 8 spherical harmonics expansion. Compared to a grid parametrisation, the number of parameters is reduced. This reduction occurs at the cost of a lower resolution: A degree and order 12 spherical harmonics has a resolution of about 15 degrees, as $\widetilde{P}_{12,0}$ has twelve zeros along z, which ranges from 0 to 180 degrees and $\cos(m\,\alpha)$ and $\sin(m\,\alpha)$ have 24 zeros along α, which ranges from 0 t 360 degrees.

$$
\begin{array}{ccccc|cccccc}
 & & & & & \color{red}{a_{00}} & & & & & \\[4pt]
 & & & & \color{blue}{b_{11}} & \color{blue}{a_{10}} & \color{blue}{a_{11}} & & & & \\[4pt]
 & & & b_{22} & \color{green}{b_{21}} & a_{20} & \color{green}{a_{21}} & a_{22} & & & \\[4pt]
 & & b_{33} & \color{green}{b_{32}} & b_{31} & \color{green}{a_{30}} & a_{31} & \color{green}{a_{32}} & a_{33} & & \\[4pt]
 & b_{44} & \color{green}{b_{43}} & b_{42} & \color{green}{b_{41}} & a_{40} & \color{green}{a_{41}} & a_{42} & \color{green}{a_{43}} & a_{44} & \\[4pt]
b_{55} & \color{green}{b_{54}} & b_{53} & \color{green}{b_{52}} & b_{51} & \color{green}{a_{50}} & a_{51} & \color{green}{a_{52}} & a_{53} & \color{green}{a_{54}} & a_{55}
\end{array}
$$

Figure 3.4.2 : Spherical harmonics coefficients up to degree and order five. The coefficient in red is the absolute term, the coefficients in blue are fully correlated with the PCO and the green coefficients are the odd terms. Source: Willi et al. (2018a).

(a) coefficient $a_{41} = 1$

(b) coefficient $a_{42} = 1$

Figure 3.4.3 : Illustration of the contribution of an odd spherical harmonics coefficient (a) and an even coefficient (b). Odd functions create fields with no symmetry with respect to the equator (zenith angle of 90 deg), whereas even functions create equatorial symmetry.

3.4.4 Spherical harmonics partial derivatives

Since the spherical harmonics expansion is a linear function of the coefficients (see Eq. 3.21), the partial derivatives simply read:

$$\frac{\partial \text{PCC}(\alpha^i, z^i)}{\partial a_{nm}} = \widetilde{P}_{nm}(\cos z^i)\,\cos(m\,\alpha^i) \tag{3.24}$$

$$\frac{\partial \text{PCC}(\alpha^i, z^i)}{\partial b_{nm}} = \widetilde{P}_{nm}(\cos z^i)\,\sin(m\,\alpha^i) \tag{3.25}$$

3.5 Multi-GNSS requirements

PCC are frequency-dependent. All current GNSS transmit ranging signals at different frequencies. Thus, an independent calibration is generated for each frequency transmitted. The frequencies of the GNSS included in RINEX 3.03 (RINEX Working Group and RTCM-SC104, 2015) are presented in Table 3.5.1.

Traditionally, calibration institutes have generated calibrations for GPS L1, GPS L2, GLONASS G1 and GLONASS G2.[4]

Since the new GPS L5 and the Galileo E5a signals are in the vicinity of the GPS L2 signal (see Figure 3.5.1), a first approximation is to assume GPS L2 patterns for GPS L5 and for Galileo E5a measurements. Unfortunately, no L5/E5a robot calibrations are available yet, as no institution is providing those. However, Geo++® announced an upgrade to Galileo calibrations for 2019.[5] Individual chamber calibrations, which include all frequencies, are available for several antennas of the European Permanent Network[6] (EPN) and the IGS network[7].

FDMA signals are a particular challenge for PCC calibration, because every satellite in view has another frequency. As the PCC is modelled as frequency-dependent correction function, in principle each satellite has a different PCC.

Wübbena et al. (2006) present a method to deal with the frequency changes within the GLONASS signals. Basically, the PCC difference between GPS L1 and GLONASS G1 is used to linearly extrapolate the GLONASS PCC for slot number $k = 0$ to any other GLONASS frequency within the GLONASS G1 signal. The same procedure is applied for GPS L2 and GLONASS G2. Frequency dependent PCC within a GNSS signal is not foreseen in the ANTEX format version 1.4 (Rothacher and Schmid, 2010).

The frequency range within GLONASS G1 and GLONASS G2 are small compared to the

---

[4]As of November 2018, the official PCV file used by the IGS is igs14.atx available on `ftp://igs.org/pub/station/general`. For receiver antennas, solely GPS L1, GPS L2, GLONASS G1 and GLONASS G2 calibrations are available in this file.

[5]IGS AWG mail 508 from 15.11.2018 by Michael Moore, available at `www.igs.org/mail` for registered users.

[6]Which kind of antenna calibration is available for EPN stations can be checked under `http://epncb.oma.be/_networkdata/stationlist.php`.

[7]Oral communication during the AWG splinter meeting, 31.10.2018, IGS Workshop, Wuhan, China.

general spread of the GNSS frequencies. The difference between the highest and the lowest frequencies is approximately 7.3 MHz within the GLONASS G1 signal and 5.7 MHz within GLONASS G2, assuming slot numbers between $k = -7$ and $k = 6$. Therefore, the estimation of a unique PCC at the GLONASS centre frequency (slot number $k = 0$) seems to be a reasonable approximation.

3.6 Validation strategies

In order to verify the performance of any calibration system, validations are essential. In principle, relative and absolute field calibrations can be validated in a similar manner. The following methods require an important logistical effort. It would make no sense to carry out such ambitious validations for a relative antenna calibration.

These methods are:

i. A validation on very short baselines is conducted. The baselines are surveyed and therefore, a ground truth is available. The comparison is conducted either on the coordinate level or on the observation residual level. This kind of validation is documented in (Kallio et al., 2018).

ii. A so-called 'ring calibration' is conducted. This implies that the same antenna is shipped to several calibration institutions and the results are compared at the PCC level.

Strategy (i) is difficult to carry out and requires a test field with as many pillars as antennas and a sufficient number of multi-GNSS receivers. Antenna types should be mixed, in order to investigate the behaviour of antennas with mixed equipment. A ground truth not only for the height but also for the position of every pillar would strengthen the validation compared to the method presented in Kallio et al. (2018). However, a full 3D ground truth at a precision of 0.1 mm is cumbersome and difficult to achieve. Strategy (ii) is complementary to approach (i). As no ground truth is available, no absolute statement can be derived from a ring calibration. However, the consistency between different calibration facilities is of uppermost importance, especially, if PCC from different facilities are used together in a GNSS solution.

Table 3.5.1 : Centre frequencies of the current GNSS according to the RINEX 3.03 standard (RINEX Working Group and RTCM-SC104, 2015). [1] The frequencies of the GLONASS FDMA signals G1 and G2 are dependent on the satellite slot number k. The slot numbers range from $k = -7$ to $k = 6$; [2] E5 is the E5a+E5b AltBOC signal.

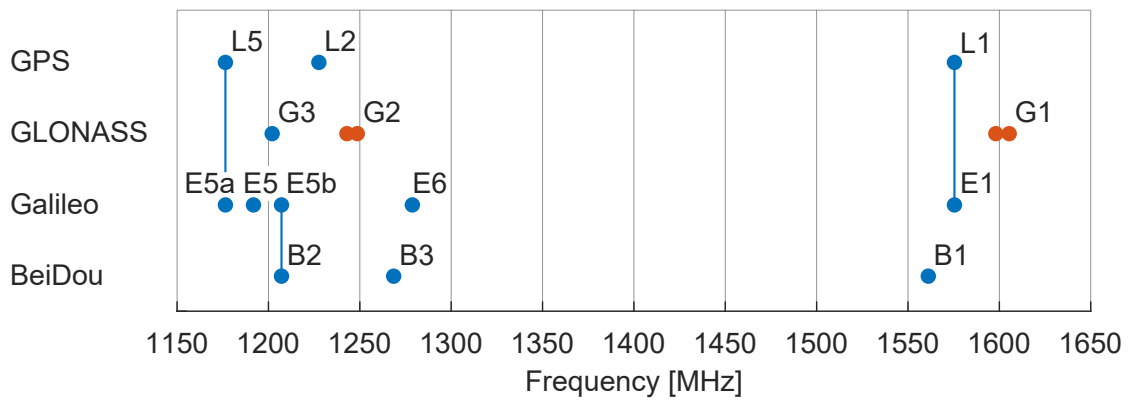|	Signal	RINEX 3 signal code	Frequency [MHz]
GPS	L1	1	1575.42
	L2	2	1227.6
	L5	5	1176.45
GLONASS	G1[1]	1	$1602 + \frac{9}{16}\,k$
	G2[1]	2	$1246 + \frac{7}{16}\,k$
	G3	3	1202.025
Galileo	E1	1	1575.42
	E5a	5	1176.45
	E5b	7	1207.14
	E5[2]	8	1191.795
	E6	6	1278.75
SBAS	L1	1	1575.42
	L2	5	1176.45
BeiDou	B1	2	1561.098
	B2	7	1207.14
	B3	6	1268.52
QZSS	L1	1	1575.42
	L2	2	1227.6
	L5	5	1176.45
	LEX	6	1278.75
IRNSS	L5	5	1176.45
	S	9	2492.028

Figure 3.5.1 : Graphical overview of the frequencies of the main four GNSS. FDMA signals are displayed in orange with two dots, marking the highest and the lowest frequency assigned. CDMA signals are displayed in blue. L1 and E1 are compatible, as well as L5 and E5a and E5b and B2 (see blue lines). The other signals do not match each other.

Chapter 4

Relative GNSS antennas field calibrations

In relative field calibration, a GNSS antenna is set up in the field together with a reference station. A PCC function can be estimated with the collected GNSS data. The result is a calibration relative to the reference antenna, thus the name 'relative calibration'. Depending on the latitude of the experimental site, some portions of the antenna hemisphere are not sampled by any data (this is the so-called north or south hole), preventing the estimation of azimuthal variations of the PCC. To solve this issue, data is acquired with several different antenna orientations. This rotation of the antenna has three effects:

    i. Enhanced sampling of the antenna hemisphere (filling of the north or south hole).

    ii. Multipath mitigation.

    iii. Separation of the horizontal PCO from the station coordinates, as illustrated in Figure 4.0.1.

The relative field calibration was extensively used in the past (Rothacher et al., 1995). However, its application decreased because of following limitations:

    i. The obtained calibration is dependent on the reference antenna (thus the name 'relative calibration').

    ii. Multipath is not prevented from affecting the results.

    iii. The method is not able to separate the height component of the PCO from the station height.

    iv. The method is not well suited to provide reliable PCC for low elevations.

Nowadays, the use of the relative field calibration is limited to validation campaigns, as for instance shown in Kallio et al. (2018).
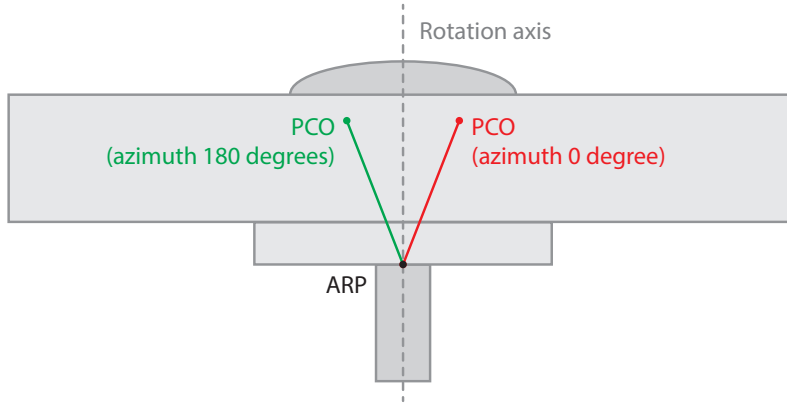
Figure 4.0.1 : The principle of PCO estimation in relative field calibration. The horizontal components of the coordinates can be decorrelated from the horizontal offset by rotating the antenna around its vertical axis. Measurement with more different azimuths (for instance, 0 deg, 90 deg, 180 deg and 270 deg) further enhance the PCO estimation.

4.1   Observation equation

A GNSS phase observation reads (Hauschild, 2017a):

$$P_A^i = \mathbf{e}_A^{i\,\mathrm{T}} \left(\mathbf{x}^i - \mathbf{x}_{A,ARP} \right) + c\,\delta t_A - c\,\delta t^i + \lambda\,N_A^i + T_A^i + I_A^i + \mathrm{PCC}_A^i + W_A^i + v_A^i \qquad (4.1)$$

where

P_A^i	is the carrier phase observation between antenna A and satellite i,
$\mathbf{e}_A^i$	is the line-of-sight vector,
$\mathbf{x}^i$	is the GNSS satellite position at signal emission,
$\mathbf{x}_{A,ARP}$	is the position of the receiver antenna ARP at signal reception,
c	is the speed of light,
δt_A	is the receiver clock error,
δt^i	is the satellite clock error,
λ	is the carrier wavelength,
N_A^i	is the integer phase ambiguity,
T_A^i	is the tropospheric delay,
I_A^i	is the ionospheric delay,
PCC_A^i	is the PCC,
W_A^i	is the phase wind-up and
v_A^i	is the zero-difference observation noise.

In so-called double-differences (Hauschild, 2017b), measurements from two stations to two satellites are differenced against each another:

$$
\begin{aligned}
P_{AB}^{ij} &= \left(P_B^j - P_A^j \right) - \left(P_B^i - P_A^i \right) \\
&= P_B^j - P_A^j - P_B^i + P_A^i
\end{aligned}
\tag{4.2}
$$

where P_{AB}^{ij} is the double-difference phase observation. In this differencing process, the receiver clock error as well as the satellite clock error is eliminated.[1] This can be seen by substitution of Eq. 4.1 into Eq. 4.2. On short baselines, the tropospheric and ionospheric delays are highly correlated between both stations. Therefore, it can be assumed that they vanish on double-difference level. Assuming antenna rotations only around the antenna vertical axis, the phase wind-up is identical to all observations of an antenna and therefore eliminated by the differencing process as well. After simplification, the double-difference reads:

$$
\begin{aligned}
P_{AB}^{ij} = \rho_{AB}^{ij} + \lambda\, N_{AB}^{ij} &+ \mathrm{PCC}_B(\alpha_B^j, z_B^j) - \mathrm{PCC}_B(\alpha_B^i, z_B^i) \\
&- \mathrm{PCC}_A(\alpha_A^j, z_A^j) + \mathrm{PCC}_A(\alpha_A^i, z_A^i) + v_{AB}^{ij}
\end{aligned}
\tag{4.3}
$$

where

ρ_{AB}^{ij}	is the double-difference geometry term,
N_{AB}^{ij}	is the double-difference phase ambiguity,
α	is the azimuth of a satellite as seen from the station,
z	is the zenith angle of a satellite as seen from the station and
v_{AB}^{ij}	is the double-difference observation noise.

As can easily be seen from Eq. 4.3, the PCC of the antenna to be calibrated (which is the parameter of interest) is fully correlated with the PCC of the reference antenna: any mismodelling of the reference PCC will lead to a bias in the PCC estimation. The conclusion is that the estimation of PCC on the double-difference level leads to relative PCC estimates.

4.2 Relative calibration of an attitude estimation platform

Although its limitations, relative antenna calibration has some appreciable advantages:

i. The set up is very easy.

ii. Virtually no infrastructure is needed.

---

[1] The satellite clock of satellite i is only completely eliminated, if the signal emission time of P_A^i is identical to the signal emission time of P_B^i. This is the case for synchronised receivers on short baselines. Otherwise, the double-difference is still affected by the differential satellite clock error. The differential satellite clock error is the difference in satellite clock between the two emission times. It is due to the drift of the satellite clock.

Therefore, the relative field calibration method is well suited for a first study of the PCC of the CubETH satellite model.

In the very specific case of an attitude determination platform, all antennas of the platform can be calibrated together in a unique field experiment. Figure 4.2.1 shows the implemented processing pipeline for a case with four antennas on a common platform. The Bernese GNSS Software V5.2 (Dach et al., 2015) was used for the processing.

The first step of the processing is to convert the RINEX data to Bernese observation files (see Figure 4.2.2). This step can be carried out individually for every file. One additional nearby antenna serves as common reference.

In a second step, baselines are formed and processed within every session (see Figure 4.2.3). Each antenna observation file is differenced against the reference antenna observation file. A standard processing pipeline leads to one normal equation system per antenna to be calibrated and per session.
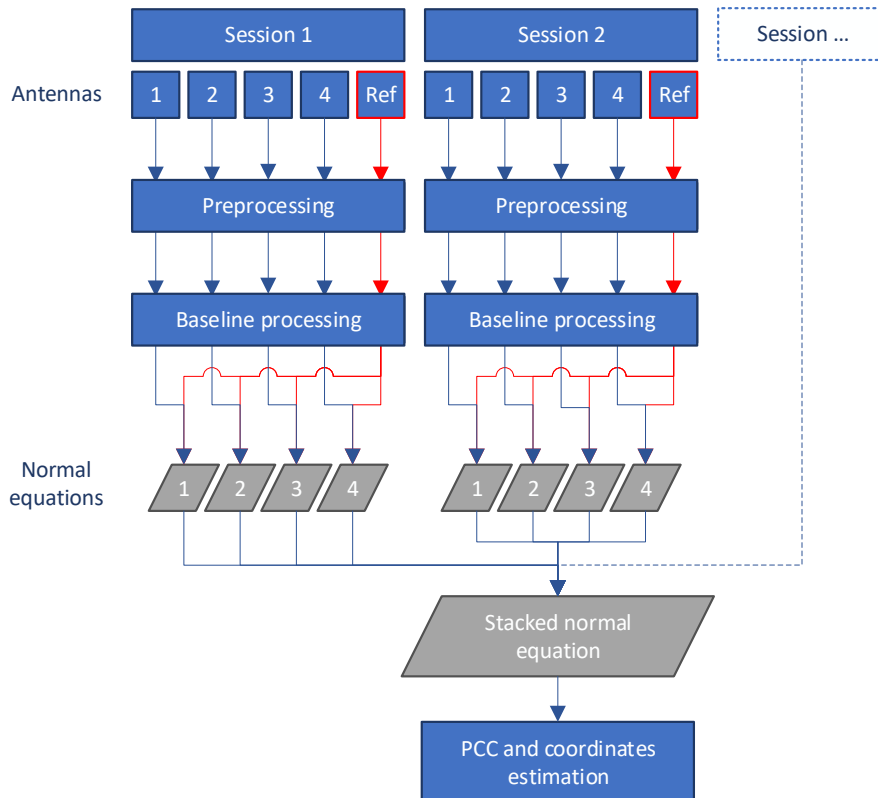

Figure 4.2.1 : Summary of the processing of relative field calibrations. Antennas 1 to 4 designate the antennas which are to calibrated and Ref designates the reference antenna. Every session results in one normal equation per antenna to be calibrated. The NEQ are stacked before inversion. The NEQ system parameters are summarized in Table 4.2.1.

The parameters present in the normal equation system after ambiguity resolution and after stacking are shown in Table 4.2.1. The number of parameters does not increase with increasing number of sessions. A unique set of station coordinates is set up for all sessions. The resulting PCO are relative to the centre of rotation, which is identical to the estimated common station coordinates. This principle is schematised for two antennas and two sessions in Figure 4.2.4. A session-wise estimation of station coordinates is not possible, as the PCO fully correlates with the station coordinates.

The rotation around a vertical axis decorrelates the horizontal station coordinates from the horizontal PCO. The station height in contrary is constrained to the average height of all four antennas, as it remains fully correlated with the PCO in up direction. Other rotations, for instance around the x- or y-axis are necessary to decorrelate the height components as well.
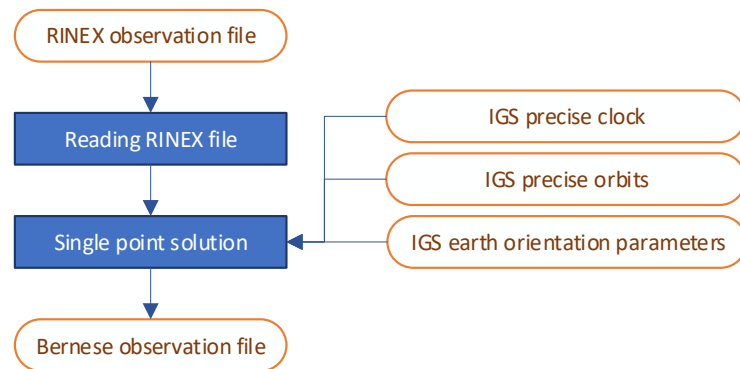
Figure 4.2.2 : Preprocessing of the observations. This step is carried out individually for every antenna and every session. The Single Point Positioning (SPP) is performed for receiver clock synchronisation.

Table 4.2.1 : Relative field calibration NEQ parameters after ambiguity resolution. The number of PCV parameters corresponds to a degree and order 8 spherical harmonics expansion. The receiver clock parameters have vanished on double-difference level.

Parameter	Number of parameters
Centre of rotation coordinates X, Y, Z	3
PCC antenna 1	3 PCO + 42 PCV
PCC antenna 2	3 PCO + 42 PCV
PCC antenna 3	3 PCO + 42 PCV
PCC antenna 4	3 PCO + 42 PCV

For implementation reasons (for instance the support of PCV in the NEQ handling program of Bernese) it is necessary to first estimate PCO and station coordinates. In a second iteration, the PCO and the station coordinates are constrained to the estimated values and only PCV are set up. This can be done separately for every baseline (but including all sessions). The results are equivalent to the results that are obtained if all parameters are set up in one estimation process. Differences might occur if the PCV is considered separately, but the PCC is identical in both cases.

4.3   Outlook

The Relative antenna calibration method gives a first insight into the expected magnitude of the PCC for a small satellite. However, according to experience, the relative field calibration method is prone to errors due to multipath. The implemented method does not allow a clean assessment of multipath, neither its mitigation.

For these reasons, an absolute field calibration using a robotic arm is targeted. Such an approach has the potential to significantly enhance the results. The implementation of an absolute field calibration is presented in the next chapters.
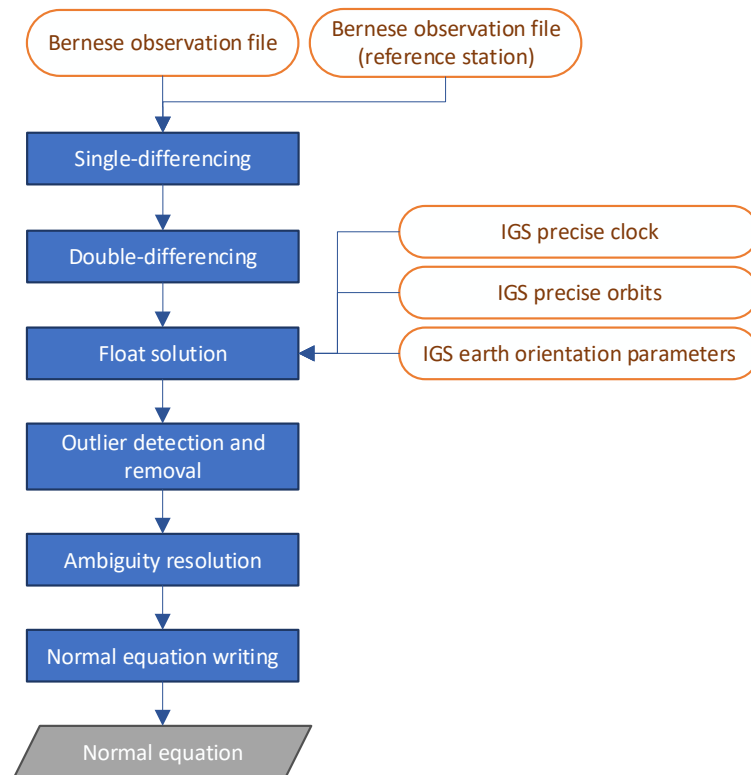
Figure 4.2.3 : Baseline processing of the observations. A baseline is formed between the reference antenna and every antenna of the attitude determination system. At the end, a normal equation is written for every baseline and every session.
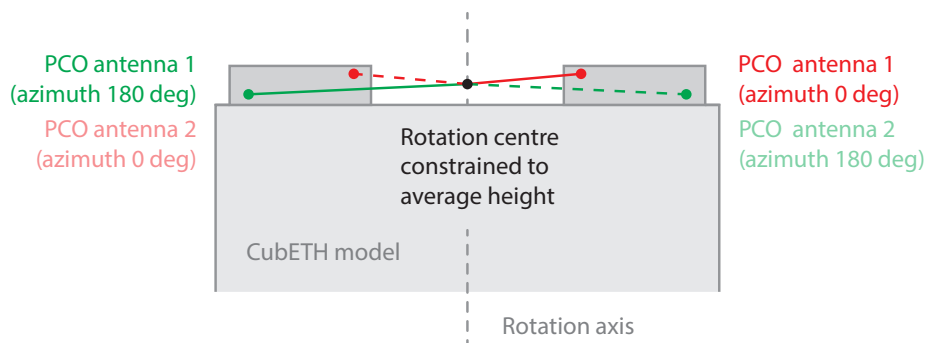

Figure 4.2.4 : Principle of PCO estimation on CubETH. The height component of the PCO cannot be separated from the height of the station coordinates solely with rotations around a vertical axis. To overcome this singularity, the height of the station is constrained to the average height of the antennas.

Chapter 5

Robot geometry

Six-axis robots have some appreciable advantages over robots with less axes in the context of antenna calibration. Five-axis robots lack one degree of freedom. Because the 6th axis is omitted compared to six-axis robots, rotations around the antenna vertical axis are not possible. Robots with two axes for instance do not allow to keep the antenna coordinates fixed while changing its orientation. Six-axis robots have six degrees of freedom and are therefore best suited for antenna calibration.

Among serial manipulator arms with six axes, the serial manipulator with an ortho-parallel basis and a spherical wrist is the most common one (Brandstötter et al., 2014). An example for such a robot is given in Figure 5.0.1. The underlying kinematic equations as well as an enhanced kinematic model, allowing for the calibration of the robot, are presented in this chapter.

5.1   Definitions

In this Chapter, following terminology is applied:

The **world coordinate system** is any global reference frame, for instance WGS84.

The **topocentric coordinate system** is the East, North, Up system with respect to the reference ellipsoid. This system is approximately parallel to the Local Level Frame (LLF), which is aligned to the local gravity field. The convention East, North, Up instead of North, East, Up is chosen in order to have a right-hand coordinate system.

The **robot (base or root) coordinate system** is a coordinate system attached to the base of the robot (see Figure 5.1.1).

The **flange coordinate system** is a coordinate system attached to the flange of the robot (see Figure 5.1.1).

The **tool coordinate system** is a coordinate system attached to the tool mounted on the robot flange. For instance, if a welding equipment is mounted on the robot flange, the tool coordinate system is centred at the welding flame and the x-axis of the coordinate system is aligned with the flame. This coordinate system is meant to facilitate the computation of

Figure 5.0.1 : KUKA Agilus KR 6 R900 sixx mounted on the roof of the Institute of Geodesy and Photogrammetry (IGP) at ETH Zurich. The robot is performing a GNSS antenna calibration. The aluminium plate serves as interface between the four bolts inserted into the concrete foundation and the robot base. The white antenna in the back is used as reference station.
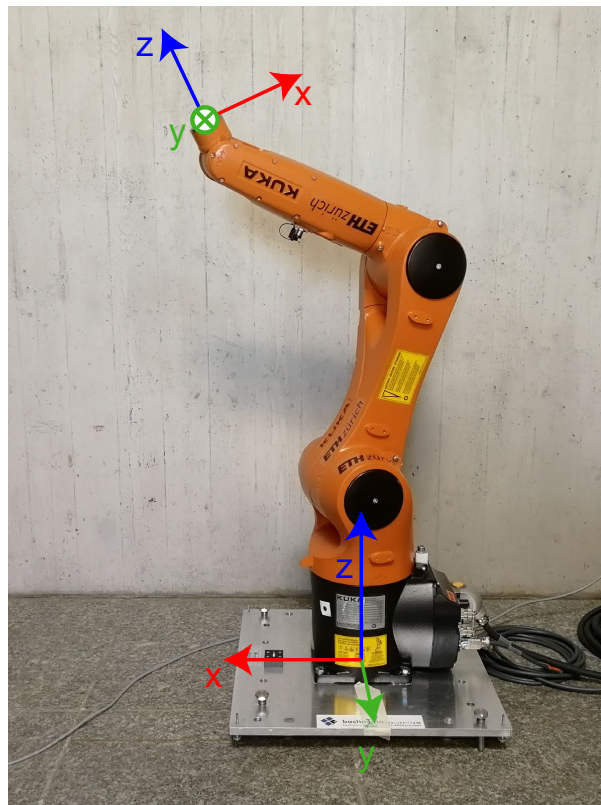
Figure 5.1.1 : Robot (base) coordinate system and flange coordinate system. The orientation of the flange coordinate system depends on the angular position of the last axis. Source: Willi and Guillaume (2019).

poses and trajectories if a tool is attached to the robot. The relationship between the different coordinate systems is shown in Figure 5.1.2.

The **robot flange** is the mechanical interface between the robot and any tool. Mathematically, if referred to it as a point, the robot flange is the intersection between the last axis and the surface of the flange.

The **pose** of the robot is the position and the orientation of the flange of the robot with respect to the robot base. The pose can be given either in X, Y, Z, A, B and C or in angular values for all axes. In the first case, KUKA applies the following convention:

$$\mathbf{R}_{t \leftarrow r} = (\mathbf{R}_{r \leftarrow t})^{\mathrm{T}} = \mathbf{R}_1(C)\,\mathbf{R}_2(B)\,\mathbf{R}_3(A) \tag{5.1}$$

where

$\mathbf{R}_{t \leftarrow r}$	is the rotation from the robot coordinate system to the tool coordinate system,
$\mathbf{R}_i$	are the rotation matrices according to Eqs. 2.4 to 2.6 and
$A,\,B,\,C$	are the three angles used by KUKA to describe the orientation of a point.

The **posture** is the topology of the robot, for instance shoulder up or shoulder down. Figure 5.1.3 shows two postures of the same pose. The same posture can be identified for different poses. For instance, if the robot goes to point A and then to a different point B without changing its topology, these are different poses but the same posture.

The **pose repeatability** is the ability of the robot to reach the same pose in the same posture several times (Willi and Guillaume, 2019) as precisely as possible. The standard deviation of the positions is a quantitative measure for this ability.

The **precision of the robot** is the ability to precisely reach given coordinates with varying orientations (Willi and Guillaume, 2019). The standard deviation is a quantitative indicator for this ability.

The **accuracy of the robot** designates its ability to reach any pose in any posture with the best accuracy. The Root Mean Square Error (RMSE) best quantifies this ability.

5.2 KUKA Agilus KR 6 R900 sixx

The KUKA Agilus KR 6 R900 sixx is a small six-axis serial manipulator. The main technical data are shown in Table 5.2.1. The whole set-up comprises:

 i. The robotic arm,
 ii. the robot controller (manufacturer provided),
iii. a SmartPad (manufacturer provided) which acts basically as control panel for the controller and
iv. an optional notebook computer to run custom software.
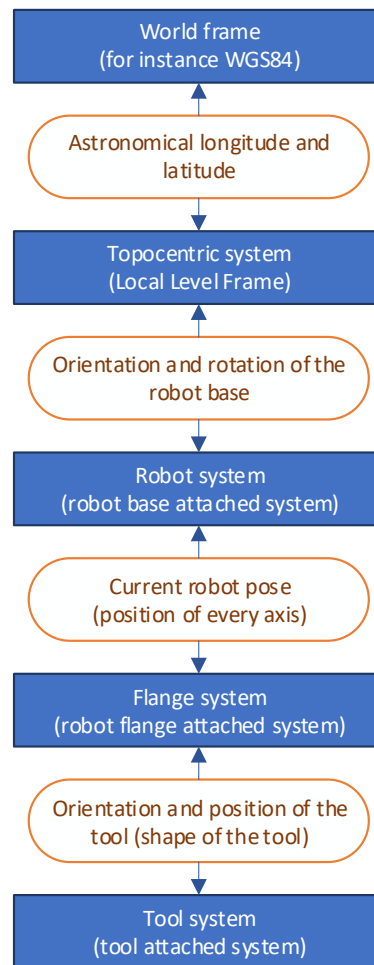
Figure 5.1.2 : Overview of the different coordinate systems and of the transformations between each of the coordinate systems.

Figure 5.1.3 : The KUKA robot in two different postures but in the same pose (position and orientation of the flange).

The components but the robotic arm are depicted in Figure 5.2.1. The interface which allows to interact with the controller by UDP and XML is called RobotSensorInterface (RSI). A custom software was developed for this specific task of interacting with the robot controller. It is called QKuka and is written in C++. The overall scheme is presented in Figure 5.2.2. Implementation details are given in the next section.

5.3 QKuka control software

A software called QKuka was developed to interact with the controller of the robotic arm. It is written in C++ and runs on a standard laptop. The communication with the controller is based on User Data Protocol (UDP) and Extensible Markup Language (XML). Figure 5.3.1 is an example for a file sent by the controller. The 'IPOC' integer which is contained in this message must be returned within a specified time frame, typically 100 milliseconds. If this is not the case, the robot executes an emergency stop. An example for an answer returning this 'IPOC' is displayed in Figure 5.3.2.

As soon as they are received, the XML files are interpreted within a program running on the robot controller (see Figure 5.3.3). A program running on the controller executes the required actions, for instance steering the tool of the robotic arm to a certain position.

5.4 Robot Kinematics

Forward kinematics is the task of computing the coordinates and the attitude of the flange (or of the tool) from angular values for every of the six axes whereas inverse kinematics is the inverse task. In general, no analytical solution to inverse kinematics is available. In some special cases, analytical solutions can be derived from geometrical thoughts.

Robots with a configuration similar to the KUKA Agilus KR 6 are said to have an ortho-parallel basis and a spherical wrist. The ortho-parallel basis consists of two parallel axes (axes 2 and 3) mounted on a first, perpendicular axis. In case of the spherical wrist, the last three axes

Table 5.2.1 : Size, weight, accuracy and operation temperature range of the KUKA KR 6 R900 sixx (Kuka, 2018).

Axes	6
Operation volume	2.85 m^2
Operation radius	901.5 mm
Maximum payload	6 kg
Weight	52 kg
Pose repeatability	0.03 mm
Operation temperature	+5℃ to +45℃

Figure 5.2.1 : KUKA control equipment consisting of a standard notebook computer (1), the KUKA controller (2) and the KUKA SmartPad (3). The notebook computer is used to run a custom software. The interface is based on a network protocol called UDP and uses XML files.
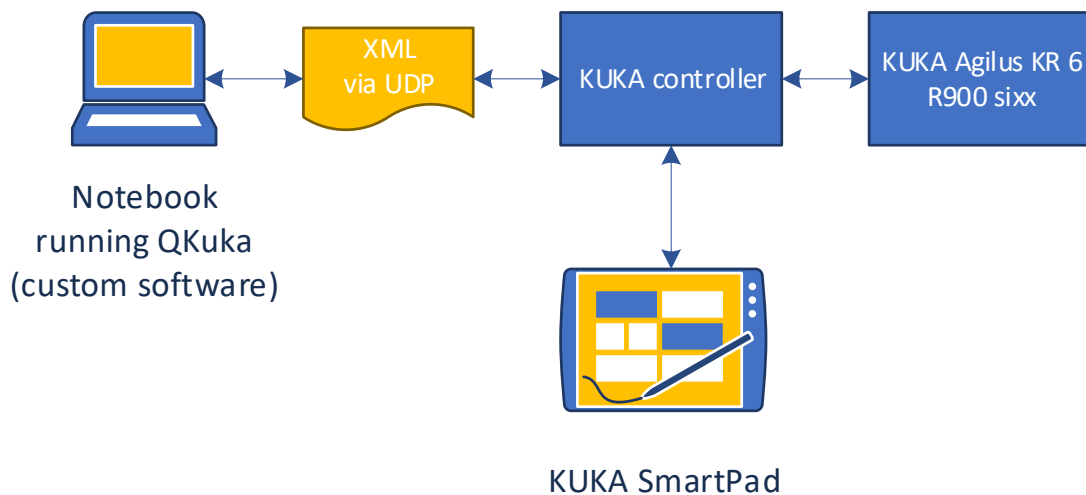

Figure 5.2.2 : Interface between the robotic arm, the controller, the SmartPad and QKuka.

```
<Rob Type="KUKA">                                                    1
    <RIst X="625.00043" Y="0.00000" Z="889.99976"                    2
          A="179.78603" B="89.99429" C="179.78603"/>                 3
    <AIPos A1="0.00000" A2="-77.16124" A3="75.60643"                 4
           A4="0.00000" A5="1.56052" A6="-0.00002"/>                 5
    <Delay D="1"/>                                                    6
    <IINA>1</IINA>                                                    7
    <IPOC>896032</IPOC>                                               8
</Rob>                                                                9
```

Figure 5.3.1 : Example for a message sent by the robot controller. It contains the current position of the tool (X, Y, Z), the Euler angles of the tool orientation (A, B, C) and the angular readings of axes A1 to A6 as well as the integer 'IPOC' and the current delay.

```
<Sen Type="ImFree">                                               1
        <EStr></EStr>                                             2
        <RKorr X="625.00" Y="0.00" Z="890.00"                     3
               A="0.00" B="90.00" C="0.00"/>                      4
        <TYPE>0</TYPE>                                            5
        <IOUT>1</IOUT>                                            6
        <IPOC>896032</IPOC>                                       7
</Sen>                                                            8
```

Figure 5.3.2 : Example for a message sent to the robot controller. It contains a position and orientation instruction for the tool (X, Y, Z, A, B and C) and two integers (TYPE and IOUT) as well as the mandatory 'IPOC'.
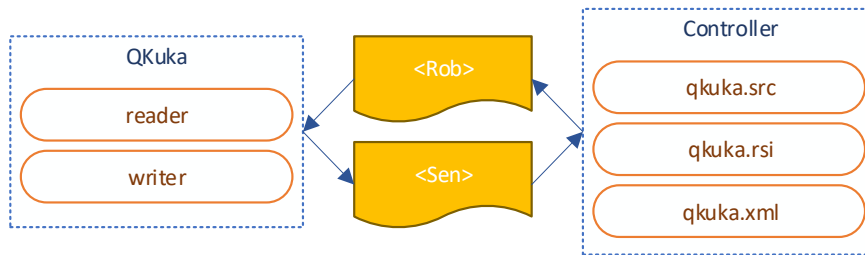

Figure 5.3.3 : Details of the exchange of XML messages. A program (*qkuka.src*) is running on the controller and executes predefined actions. The actual reading of the XML file is achieved in *qkuka.rsi*, based on the format description of the XML file, which is contained in *qkuka.xml*.

(axes 4 to 6) intersect in one point. The consequence is very pleasant, as this property allows to separate the coordinate computation part from the attitude determination part. The following developments are based on Brandstötter et al. (2014). As shown by the authors, this kind of robots can be parametrized by only seven parameters. The values of the parameters for the present case are given in Table 5.4.1. The six non-zero parameters are shown in Figure 5.4.1. Figure 5.4.2 should convince the reader that all links and joints are in one plane and that $b = 0$. The axes one to three control the coordinates, whereas the axes four to six control the attitude of the flange. The variables θ_1 to θ_6 are the angles of rotation of every axis and therefore our control variables.

5.4.1   Forward kinematics (Brandstötter et al., 2014)

The task of computing the position and the attitude of the flange of the robot or the tool mounted on the robot flange, given the angle of every axis, is called forward kinematics. The point C is the intersection of the last three axes (see also Figure 5.4.1). The coordinates **c** of the

Table 5.4.1 : The seven geometrical parameters of the KUKA Agilus KR 6 R900 sixx. b is equal to zero as all the links and joints are in one plane for this type of robot.

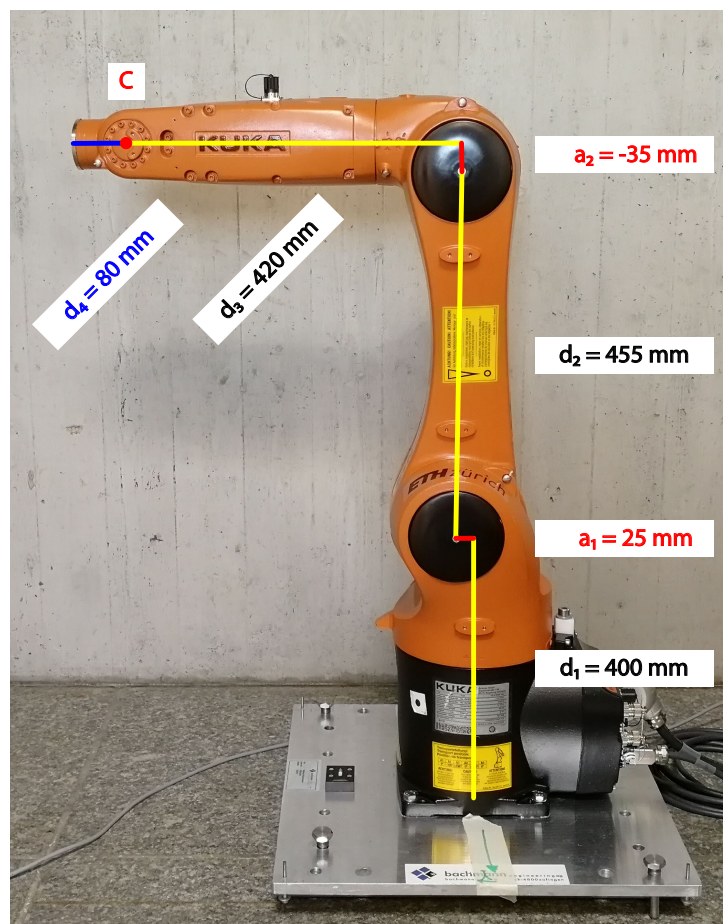| Parameter	Value [mm]
a_1	25
a_2	-35
b	0
d_1	400
d_2	455
d_3	420
d_4	80

Figure 5.4.1 : The six non-zero geometrical parameters of the KUKA Agilus KR 6 R900 sixx. The robot x-axis is on the left, the y-axis is pointing towards the reader. The red dot shows the point C, which is the intersection of the last three axes.

Figure 5.4.2 : Front view of the KUKA Agilus KR 6 R900 sixx. It can easily be seen that all links
and joints are in one plane.

point C in the robot coordinate system are given by:

$$\mathbf{c} = \begin{pmatrix} \cos\theta_1 & -\sin\theta_1 & 0 \\ \sin\theta_1 & \cos\theta_1 & 0 \\ 0 & 0 & 1 \end{pmatrix} \mathbf{c}' + \begin{pmatrix} 0 \\ 0 \\ d_1 \end{pmatrix} \tag{5.2}$$

with

$$\mathbf{c}' = \begin{pmatrix} d_2\,\sin\theta_2 + k\,\sin(\theta_2 + \theta_3 + \phi_3) + a_1 \\ b \\ d_2\,\cos\theta_2 + k\,\cos(\theta_2 + \theta_3 + \phi_3) \end{pmatrix} \tag{5.3}$$

and with

$$\phi_3 = \arctan\frac{a_2}{d_3} \tag{5.4}$$

$$k = \sqrt{a_2^2 + d_3^2} \tag{5.5}$$

where

$\mathbf{c}$ is the set of coordinates, given in the robot coordinate system, of the intersection of the last three axes,

θ_i is the angular reading of axis i,

$\mathbf{c}'$ is an auxiliary point,

ϕ_3 is an auxiliary variable and

k is an auxiliary variable as well.

The final coordinates of the flange are computed using the attitude of the flange and the length of the last articulation:

$$\mathbf{u} = \mathbf{c} + d_4\,\mathbf{R}_{r\leftarrow f} \begin{pmatrix} 0 \\ 0 \\ 1 \end{pmatrix} \tag{5.6}$$

with $\mathbf{u}$ being the coordinates of the flange. The angles four to six control the attitude of the flange. The final attitude is the product of the attitude up to the point C and the attitude of the last three axis.

$$\mathbf{R}_{r\leftarrow f} = \mathbf{R}_{r\leftarrow c}\,\mathbf{R}_{c\leftarrow f} \tag{5.7}$$

$$\mathbf{R}_{c\leftarrow f} = \begin{pmatrix} c_{\theta_4}c_{\theta_5}c_{\theta_6} - s_{\theta_4}s_{(\theta_6)} & -c_{\theta_4}c_{\theta_5}s_{\theta_6} - s_{\theta_4}c_{\theta_6} & c_{\theta_4}s_{\theta_5} \\ s_{\theta_4}c_{\theta_5}c_{\theta_6} + c_{\theta_4}s_{\theta_6} & -s_{\theta_4}c_{\theta_5}s_{\theta_6} + c_{\theta_4}c_{\theta_6} & s_{\theta_4}s_{\theta_5} \\ -s_{\theta_5}c_{\theta_6} & s_{\theta_5}s_{\theta_6} & c_{\theta_5} \end{pmatrix} \tag{5.8}$$

$$\mathbf{R}_{r \leftarrow c} = \begin{pmatrix} c_{\theta_1}c_{\theta_2}c_{\theta_3} - c_{\theta_1}s_{\theta_2}s_{\theta_3} & -s_{\theta_1} & c_{\theta_1}c_{\theta_2}s_{\theta_3} + c_{\theta_1}s_{\theta_2}c_{\theta_3} \\ s_{\theta_1}c_{\theta_2}c_{\theta_3} - s_{\theta_1}s_{\theta_2}s_{\theta_3} & c_{\theta_1} & s_{\theta_1}c_{\theta_2}s_{\theta_3} + s_{\theta_1}s_{\theta_2}c_{\theta_3} \\ -s_{\theta_2}c_{\theta_3} - c_{\theta_2}s_{\theta_3} & 0 & -s_{\theta_2}s_{\theta_3} + c_{\theta_2}c_{\theta_3} \end{pmatrix} \tag{5.9}$$

where

$\mathbf{R}_{r \leftarrow f}$ is the rotation from the flange attached system to the the robot system,

$\mathbf{R}_{r \leftarrow c}$ is the rotation from the system associated with the point C to the robot coordinate system,

$\mathbf{R}_{c \leftarrow f}$ is the rotation from the flange system to the system associated with point C,

s_{θ_i} is the sine of θ_i and

c_{θ_i} is the cosine of θ_i.

The separation, mentioned earlier, between the attitude computation and the coordinate computation is well reflected by the fact that $\mathbf{R}_{r \leftarrow c}$ only depends on θ_1 to θ_3 and $\mathbf{R}_{c \leftarrow f}$ only depends on θ_4 to θ_6.

In order to comply with the KUKA convention, following operations have to be performed:

$$\theta_1 = -\theta_1' \tag{5.10}$$

$$\theta_2 = \theta_2' + \frac{\pi}{2} \tag{5.11}$$

$$\theta_4 = -\theta_4' \tag{5.12}$$

$$\theta_6 = -\theta_6' \tag{5.13}$$

with θ_i' being the angles used by the KUKA controller (see also Figure 5.4.3).

If the tool is affected by an offset, an additional transformation leads to the coordinates of the tool in the robot coordinate system:

$$\mathbf{R}_{r \leftarrow t} = \mathbf{R}_{r \leftarrow f} \, \mathbf{R}_{f \leftarrow t} \tag{5.14}$$

$$\mathbf{t} = \mathbf{u} + t_z'' \, \mathbf{R}_{r \leftarrow t} \begin{pmatrix} 0 \\ 0 \\ 1 \end{pmatrix} + t_x'' \, \mathbf{R}_{r \leftarrow t} \begin{pmatrix} 1 \\ 0 \\ 0 \end{pmatrix} + t_y'' \, \mathbf{R}_{r \leftarrow t} \begin{pmatrix} 0 \\ 1 \\ 0 \end{pmatrix} \tag{5.15}$$

Where

$\mathbf{t}$ is the set of coordinates of the tool (in the robot coordinate system),

t_x'' is the tool offset in x (in the tool system),

t_y'' is the tool offset in y (in the tool system),

t_z'' is the tool offset in z (in the tool system) and

$\mathbf{R}_{f \leftarrow t}$ is the rotation from the tool system to the flange system.

Frequently, tools do have an offset in z- but not in x- and y-direction. This is the reason for
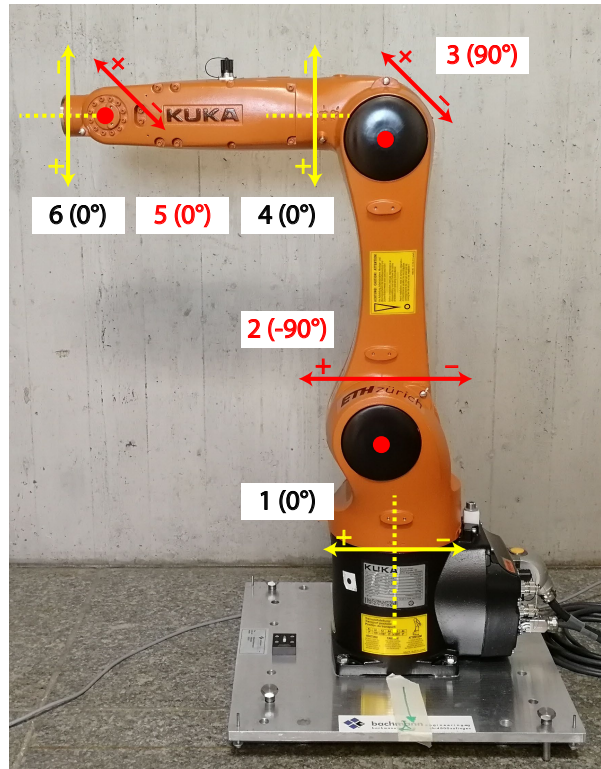
Figure 5.4.3 : The KUKA angle convention for θ_1 to θ_6. Axes shown in yellow are parallel to the image plane, red axes are out of plane. Source: Willi and Guillaume (2019).

the non-alphabetic order in Eq. 5.15. Typically, $\mathbf{R}_{f \leftarrow t}$ is either an identity matrix (as in the case of antenna calibrations) or its values are calibrated and therefore known. It can be expressed as an Euler sequence:

$$\mathbf{R}_{t \leftarrow f} = (\mathbf{R}_{f \leftarrow t})^{\mathrm{T}} = \mathbf{R}_1(\gamma'')\,\mathbf{R}_2(\beta'')\,\mathbf{R}_3(\alpha'') \tag{5.16}$$

where α'', β'' and γ'' are the tool yaw, pitch and roll angles. The final results of the algorithm are the coordinates of the tool $\mathbf{t}$ and its orientation $\mathbf{R}_{r \leftarrow t}$ in the robot coordinate system.

5.4.2 Inverse kinematics (Brandstötter et al., 2014)

Unsurprisingly, inverse kinematics is more complicated than forward kinematics. This tasks consist of computing the angles θ_1 to θ_6 given the position and attitude of the tool. Again, the problem can be solved in two parts. The coordinates of the tool $\mathbf{t}$ and its orientation $\mathbf{R}_{r \leftarrow t}$ are the input variables:

$$\mathbf{u} = \mathbf{t} - t_z''\,\mathbf{R}_{r \leftarrow t} \begin{pmatrix} 0 \\ 0 \\ 1 \end{pmatrix} - t_x''\,\mathbf{R}_{r \leftarrow t} \begin{pmatrix} 1 \\ 0 \\ 0 \end{pmatrix} - t_y''\,\mathbf{R}_{r \leftarrow t} \begin{pmatrix} 0 \\ 1 \\ 0 \end{pmatrix} \tag{5.17}$$

$$\mathbf{R}_{r \leftarrow f} = \mathbf{R}_{r \leftarrow t}\,\mathbf{R}_{t \leftarrow f} = \mathbf{R}_{r \leftarrow t}\,(\mathbf{R}_{f \leftarrow t})^{\mathrm{T}} \tag{5.18}$$

$$\mathbf{c} = \mathbf{u} - d_4 \, \mathbf{R}_{r \leftarrow f} \begin{pmatrix} 0 \\ 0 \\ 1 \end{pmatrix} \tag{5.19}$$

where

$\mathbf{u}$	is the set of coordinates of the flange in the robot system,
$\mathbf{t}$	is the set of coordinates of the tool in the robot system,
t''_x	is the tool offset in x in the tool system,
t''_y	is the tool offset in y in the tool system,
t''_z	is the tool offset in z in the tool system,
$\mathbf{R}_{r \leftarrow t}$	is the rotation from the tool system to the robot system,
$\mathbf{R}_{r \leftarrow f}$	is the rotation from the flange system to the robot system and
$\mathbf{c}$	is the set of coordinates of the intersection of the last tree axis.

Once the coordinates $\mathbf{c}$ of the point C have been computed, they can be used to retrieve the angular values of the first three axes. Eight different solutions exist. The eight possible postures for a given pose are displayed in Figures 5.4.4 and 5.4.5. The solutions one to four for θ_1 to θ_3 read:

$$\theta_{1,1} = \operatorname{atan2}(c_2, c_1) - \operatorname{atan2}(b, h_1 + a_1) \tag{5.20}$$

$$\theta_{1,2} = \theta_{1,1} \tag{5.21}$$

$$\theta_{1,3} = \operatorname{atan2}(c_2, c_1) + \operatorname{atan2}(b, h_1 + a_1) - \pi \tag{5.22}$$

$$\theta_{1,4} = \theta_{1,3} \tag{5.23}$$

$$\theta_{2,1} = -\arccos \frac{s_1^2 + d_2^2 - k^2}{2 \, s_1 \, d_2} + \operatorname{atan2}(h_1, c_3 - d_1) \tag{5.24}$$

$$\theta_{2,2} = \arccos \frac{s_1^2 + d_2^2 - k^2}{2 \, s_1 \, d_2} + \operatorname{atan2}(h_1, c_3 - d_1) \tag{5.25}$$

$$\theta_{2,3} = -\arccos \frac{s_2^2 + d_2^2 - k^2}{2 \, s_2 \, d_2} - \operatorname{atan2}(h_1 + 2 \, a_1, c_3 - d_1) \tag{5.26}$$

$$\theta_{2,4} = \arccos \frac{s_2^2 + d_2^2 - k^2}{2 \, s_2 \, d_2} - \operatorname{atan2}(h_1 + 2 \, a_1, c_3 - d_1) \tag{5.27}$$

$$\theta_{3,1} = \arccos \frac{s_1^2 - d_2^2 - k^2}{2 \, d_2 \, k} - \operatorname{atan2}(a_2, d_3) \tag{5.28}$$

$$\theta_{3,2} = -\arccos \frac{s_1^2 - d_2^2 - k^2}{2 \, d_2 \, k} - \operatorname{atan2}(a_2, d_3) \tag{5.29}$$

$$\theta_{3,3} = \arccos \frac{s_2^2 - d_2^2 - k^2}{2 \, d_2 \, k} - \operatorname{atan2}(a_2, d_3) \tag{5.30}$$

$$\theta_{3,4} = -\arccos \frac{s_2^2 - d_2^2 - k^2}{2 \, d_2 \, k} - \operatorname{atan2}(a_2, d_3) \tag{5.31}$$

where $\theta_{i,j}$ is the jth solution of θ_i and c_i is the ith component of $\mathbf{c}$. The additional variables h_1,

s_1, s_2 and k are defined as follows:

$$h_1 = \sqrt{c_1{}^2 + c_2{}^2 - b^2} - a_1 \tag{5.32}$$

$$s_1 = \sqrt{h_1^2 + (c_3 - d_1)^2} \tag{5.33}$$

$$s_2 = \sqrt{(h_1 + 2\,a_1)^2 + (c_3 - d_1)^2} \tag{5.34}$$

$$k = \sqrt{a_2^2 + d_3^2} \tag{5.35}$$

The solutions five to eight for θ_1 to θ_3 are identical to solutions one to four for these three angles:

$$\theta_{i,j} = \theta_{i,j+4} \qquad i \in [1,2,3]\,, j \in [1,2,3,4] \tag{5.36}$$

Eq. 5.36 can easily be verified by comparing Figure 5.4.4 to Figure 5.4.5. The solutions for the angles θ_4 to θ_6 read:

$$\theta_{4,j} = \operatorname{atan2}\left(R_{23}\,h_{3,j} - R_{13}\,h_{2,j},\, R_{13}\,h_{3,j}\,h_{5,j} + R_{23}\,h_{2,j}\,h_{5,j} - R_{33}\,h_{4,j}\right) \tag{5.37}$$

$$\theta_{4,j+4} = \theta_{4,j} + \pi \tag{5.38}$$

$$\theta_{5,j} = \operatorname{atan2}\left(\sqrt{1 - h_{6,j}^2},\, h_{6,j}\right) \tag{5.39}$$

$$\theta_{5,j+4} = -\theta_{5,j} \tag{5.40}$$

$$\theta_{6,j} = \operatorname{atan2}\big(R_{12}\,h_{3,j}\,h_{4,j} + R_{22}\,h_{2,j}\,h_{4,j} + R_{32}\,h_{5,j},$$
$$-R_{11}\,h_{3,j}\,h_{4,j} - R_{21}\,h_{2,j}\,h_{4,j} - R_{31}\,h_{5,j}\big) \tag{5.41}$$

$$\theta_{6,j+4} = \theta_{6,j} - \pi \tag{5.42}$$

where R_{mn} are the elements of $\mathbf{R}_{r\leftarrow f}$ from Eq. 5.18 and $j \in [1,2,3,4]$. The auxiliary variables $h_{2,j}$ to $h_{6,j}$ are defined as follows:

$$h_{2,j} = \sin\theta_{1,j} \tag{5.43}$$

$$h_{3,j} = \cos\theta_{1,j} \tag{5.44}$$

$$h_{4,j} = \sin(\theta_{2,j} + \theta_{3,j}) \tag{5.45}$$

$$h_{5,j} = \cos(\theta_{2,j} + \theta_{3,j}) \tag{5.46}$$

$$h_{6,j} = R_{13}\,h_{3,j}\,h_{4,j} + R_{23}\,h_{2,j}\,h_{4,j} + R_{33}\,h_{5,j} \tag{5.47}$$
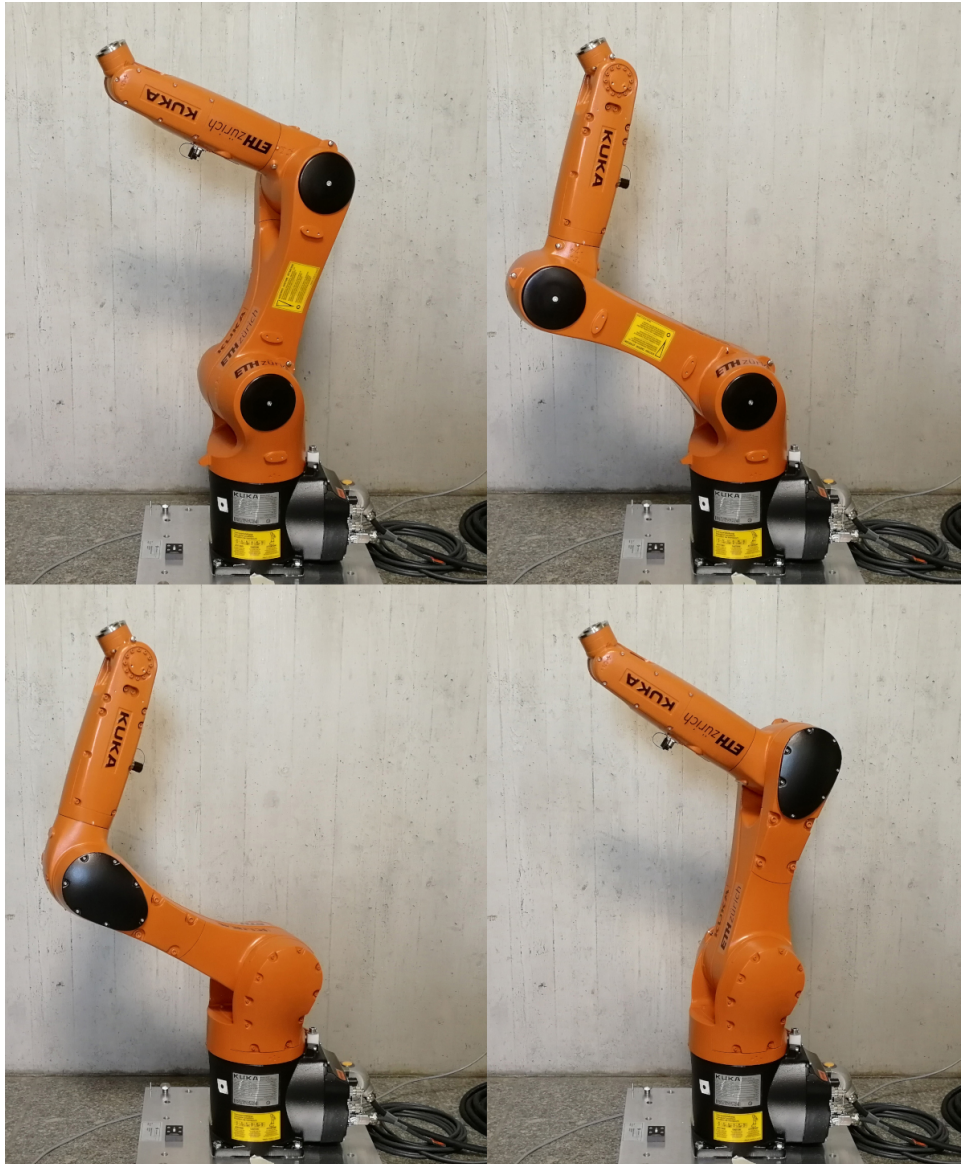
Figure 5.4.4 : View of the postures one to four ($j \in [1, 2, 3, 4]$), from left to right, for a given pose. Source: Willi and Guillaume (2019).

Figure 5.4.5 : View of the postures five to eight ($j \in [5, 6, 7, 8]$), from left to right, for a given pose.

In order to match the KUKA sign and offset conventions, following changes must be performed:

$$\theta'_1 = -\theta_1 \tag{5.48}$$

$$\theta'_2 = \theta_2 - \frac{\pi}{2} \tag{5.49}$$

$$\theta'_4 = -\theta_4 \tag{5.50}$$

$$\theta'_6 = -\theta_6 \tag{5.51}$$

where θ'_i denotes the KUKA angle convention and θ_i denotes the angles as computed by the present algorithm.

5.5 Enhanced kinematic model

Every robot is affected by errors, as the actual geometry does not perfectly fit the nominal geometry. In the same way as axis errors affect theodolites, axis errors also affect an industrial robot: orthogonal axes are not necessarily perfectly orthogonal and parallel axes are not necessarily perfectly parallel.

Furthermore, the dimensions do not necessarily fit the nominal values: the robot's arms can be slightly longer or shorter than indicated in the data-sheet. Finally, the axis angles can be affected by offsets. The first kind of errors cannot be modelled by the kinematic model presented in Section 5.4.1. Therefore, the so-called Denavit-Hartenberg (DH) convention is used (Corke, 2017; Hollerbach et al., 2016).

5.5.1 State of the art

Kinematic robot models based on DH parameters or a similar parametrisation are widely used (Schröer, 1999; Motta, 2006; Hollerbach et al., 2016). The different robot calibration models are very well discussed in (Schröer et al., 1997). Most typically, laser trackers are used for the calibration. Nubiola and Bonev (2013) and Allman et al. (2018) are good examples for robot calibrations using laser trackers. Typically, accuracies of 0.2 mm to 0.4 mm are obtained after calibration of the robot (Nubiola and Bonev, 2013; Allman et al., 2018).

Menge (2003) and Kersten (2014) present a calibration model for a robot with five axes. The subject of the calibration is a robot used for GNSS PCC estimation. The model comprises 20 parameters, including parameters for the joint elasticity. The accuracy of the calibrated robot is 0.2 to 0.3 mm. The measurements were performed with theodolites in the first case and with a laser tracker in the second case.

5.5.2 Denavit-Hartenberg parametrisation

The basic idea is to represent every axis of the robot as a coordinate transformation in 3 dimensions. In principle, this would require three translational parameters and three rotational

parameters. By adroitly attaching the coordinate systems to every axis, the number of parameters can be reduced to four: two rotation angles and two translation. The principle is schematised in Figure 5.5.1.

The first rotational parameter Θ is the angle between two subsequent x-axes. It is the control variable and therefore the final angle reading from the robot. The signs were chosen to match the KUKA convention. α is the angle between two successive y-axes and is 0 for parallel axes. The length of a link is denoted by a and the lateral offset of a joint is denoted by d. The DH parameters for the KUKA Agilus KR 6 R900 sixx are given in Table 5.5.1 and the non-zero parameters are depicted in Figure 5.5.2. The addition of $\delta\Theta$ is necessary to comply with the KUKA convention.

Using DH parameters, the coordinates and the orientation of the flange read as a homogeneous transformation matrix:

$$\mathbf{T} = \prod_{i=0}^{6} \mathbf{T}_i = \left(\begin{array}{ccc|c} & \mathbf{R}_{r \leftarrow f} & & \mathbf{u} \\ \hline 0 & 0 & 0 & 1 \end{array} \right) \tag{5.52}$$

where

$\mathbf{T}$ is the homogeneous transformation matrix of the flange,

$\mathbf{T}_i$ is the transformation associated with joint and link i,

$\mathbf{R}_{r \leftarrow f}$ is the rotation from the flange system to the robot system and

$\mathbf{u}$ is the coordinates of the flange.

With $i \in [1, 2, 3, 4, 5, 6]$. The individual transformations are functions of the DH parameters:

$$\mathbf{T}_i = \begin{pmatrix} \cos(\Theta_i + \delta\Theta_i) & -\sin(\Theta_i + \delta\Theta_i)\cos\alpha_i & \sin(\Theta_i + \delta\Theta_i)\sin\alpha_i & a_i\cos(\Theta_i + \delta\Theta_i) \\ \sin(\Theta_i + \delta\Theta_i) & \cos(\Theta_i + \delta\Theta_i)\cos\alpha_i & -\cos(\Theta_i + \delta\Theta_i)\sin\alpha_i & a_i\sin(\Theta_i + \delta\Theta_i) \\ 0 & \sin\alpha_i & \cos\alpha_i & d_i \\ 0 & 0 & 0 & 1 \end{pmatrix} \tag{5.53}$$

Table 5.5.1 : DH parameters for the KUKA Agilus KR 6 R900 sixx.

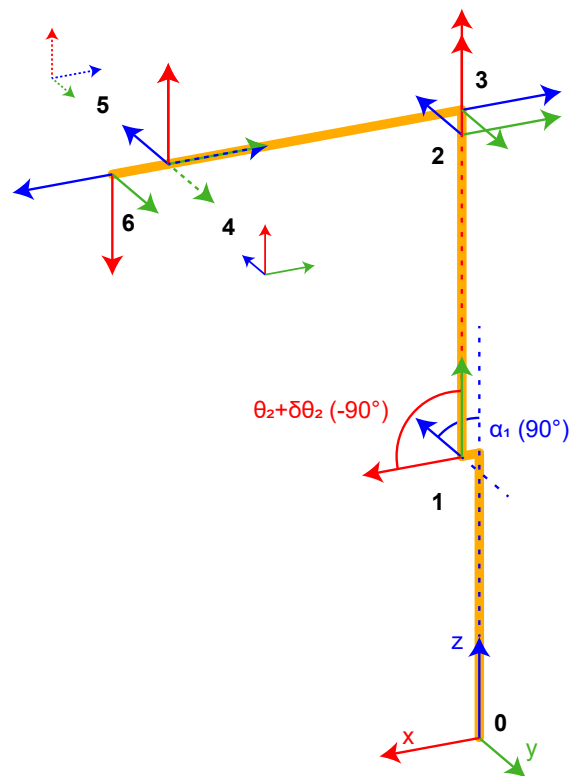|	Θ [rad]	$\delta\Theta$ [rad]	α [rad]	a [mm]	d [mm]
1	$-\theta_1$	0	$\pi/2$	25	400
2	$-\theta_2$	0	0	455	0
3	$-\theta_3$	$\pi/2$	$-\pi/2$	35	0
4	θ_4	0	$\pi/2$	0	-420
5	$-\theta_5$	0	$-\pi/2$	0	0
6	θ_6	π	π	0	-80

Figure 5.5.1 : Application of the DH convention to a robot with the same configuration as the KUKA Agilus KR 6 R900 sixx. A coordinate system is attached to every joint. Its z-axis is collinear with the joint axis. Each joint and link pair is represented by four parameters. The angle between two successive x-axes is called Θ and the angle between to successive z-axes is α. Source: Willi and Guillaume (2019).
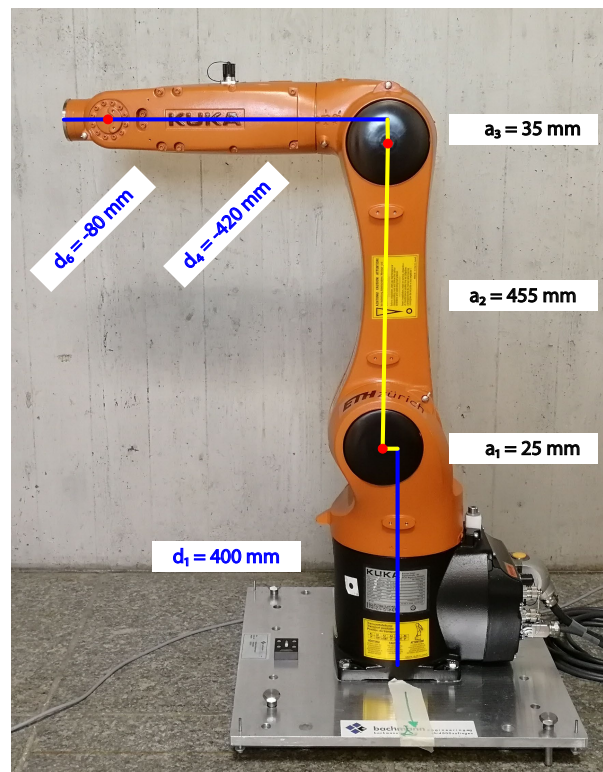
Figure 5.5.2 : The non-zero DH length parameters (a and d) of the KUKA Agilus KR 6 R900 sixx.
Source: Willi and Guillaume (2019).

If $\mathbf{T}_0$ is equal to the identity matrix, the obtained coordinates are in the robot coordinate system. To obtain coordinates in an other frame, $\mathbf{T}_0$ can be initialized as follows:

$$\mathbf{T}_0 = \left(\begin{array}{ccc|c} & & & t'_x \\ & \mathbf{R}_{w \leftarrow r} & & t'_y \\ & & & t'_z \\ \hline 0 & 0 & 0 & 1 \end{array} \right) \tag{5.54}$$

where $\mathbf{R}_{w \leftarrow r}$ is the rotation matrix from the robot system to the world system (e.g. a topocentric system) and t'_x, t'_y and t'_z are the offsets and therefore equal to the coordinates of the robot in the world frame. This rotation can be expressed as Euler sequence:

$$\mathbf{R}_{r \leftarrow w} = (\mathbf{R}_{w \leftarrow r})^{\mathrm{T}} = \mathbf{R}_1(\gamma') \, \mathbf{R}_2(\beta') \, \mathbf{R}_3(\alpha') \tag{5.55}$$

where α', β' and γ' are the yaw, pitch and roll angles of the robot in the world coordinate system[1]. The convention for the rotation matrices is the same as in Eqs. 2.4 to 2.6. If desired, the tool orientation and the tool offsets can be applied on top of this transformation exactly as shown in Eqs. 5.14 and 5.15

5.5.3 Calibration model

Based on the developments of the previous chapter, a model with 36 parameters was defined. The parameters are listed in Table 5.5.3. In order to decorrelate all parameters from each other, measurements well distributed in the whole operation space of the robot would be needed. The tool orientation can only be estimated if the attitude of the tool is observed. This is for instance the case, if three or more targets are mount on the robot flange.

In general, it is not necessary to fully decorrelate the parameters. If a calibration is meant to be used only over a confined part of the robot operation space, a reduced calibration can be conducted. In general, the calibration will be valid at least in the vicinity of the measurement points. In the specific case of GNSS antenna calibrations, a reduced sequence was found to work well.

5.5.4 Model limitations

The current implementation has several limitations, namely:

  i. Temperature dependency is not modelled,

 ii. joint elasticity is not modelled and

iii. the non-linearity of axis six is not modelled.

---

[1]Note that in the software QKuka the opposite convention is used: $\mathbf{R}_{w \leftarrow r} = \mathbf{R}_1(\gamma') \, \mathbf{R}_2(\beta') \, \mathbf{R}_3(\alpha')$.

Table 5.5.3 : KUKA DH calibration model parameters. Source: Willi and Guillaume (2019).

1 to 6	$\delta\Theta_1$ to $\delta\Theta_6$	Axis angle offsets
7 to 12	α_1 to α_6	DH parameters α
13 to 18	a_1 to a_6	DH parameters a
19 to 24	d_1 to d_6	DH parameters d
25 to 27	t''_x, t''_y, t''_z	Tool offsets in x, y and z
28 to 30	α'', β'', γ''	Tool orientation as Euler sequence
31 to 33	t'_x, t'_y, t'_z	Robot coordinates in the world frame
34 to 36	α', β', γ'	Robot orientation in the world frame as Euler sequence

The latter two effects are well studied and presented in the literature. Nubiola and Bonev (2013) included a stiffness model and a non-linearity model for axis six and obtained excellent results. Inclusion of these two models is expected to enhance the accuracy of the calibrated robot. The non-linearity model parameters can be estimated only if the orientation of the tool is observed as well. This requires a laser tracker with a probe for six degrees of freedom.

The temperature dependence is more difficult to model. Theoretical considerations and simulations lead to the conclusion that the temperature dependence can be neglected if using a small robot and if high precision and not high accuracy is targeted (Willi and Guillaume, 2019). However, further experiments are necessary to verify this assumption. A possible approach to deal with temperature changes is to include temperature dependent DH parameters, as suggested by Bilich et al. (2018).

5.6   Outlook

With the successful calibration, the robot is ready to be used for absolute antenna calibrations (see Chapter 6). The use of the robot in the field, together with periodic recalibration, will help to answer the open research questions. Namely:

   i. How is the long-term stability of the calibration?

   ii. How do temperature variations influence the DH parameters?

Further data will help to improve the understanding of the underlying processes and finally improve the kinematic robot models.

Chapter 6

Absolute GNSS antenna field calibration

Absolute field calibrations represent an enhancement of relative field calibration. Introducing rotations around axes other than the antenna vertical axis allows to decorrelate all three components of the PCO from the station coordinates. The other main advantages of absolute field calibration over relative field calibration are:

i. The probing of the antenna hemisphere can be controlled by choosing appropriate rotations, for instance by choosing a large inclination of the antenna,

ii. multipath can potentially be mitigated and

iii. the calibration result is independent from the calibration of the reference antenna.

Time-differenced GNSS observations fulfil requirement (ii) and (iii), unlike double-differenced or single-differenced observations. This approach is presented in the following section.

6.1   Time-differencing mode

In principle, two differencing modes in time are imaginable:

i. Differences over a sidereal day and

ii. Differences over only a few seconds.

The first absolute field calibrations were performed using differences over a sidereal day (Wübbena et al., 1997; Menge, 2003). As the GPS constellations repeats after a sidereal day, the same multipath is expected to repeat as well. This technique does not apply to other GNSS with other repeat periods. The drawback of this method is the very long calibration time of at least a sidereal day plus the duration of the measurements on the second day. However, the measurements on the first day do not necessarily need to cover 24 hours.

   In the second differencing mode, a robotic manipulator is used to perform very fast rotations. Multipath is a time varying quantity. Differencing epochs that are very close to each other

eliminates the multipath fraction which is common to both epochs. In order to have a reasonable correlation, the time between epochs should not exceed a few seconds. Multipath from the ground has a rate of $1.73\,h \cdot 10^{-4}$ m/s, where h is the antenna height over ground (Braasch, 2017, p. 447); The multipath change (and thus the error in time-differences) already exceeds a millimetre after five seconds. Objects located closer to the antenna (for instance the measurement pillar) will have faster multipath rates and thus, their multipath contribution will not be eliminated in the time-differencing process.

6.2 Triple-difference observation equation

A GNSS phase observation reads (Hauschild, 2017a):

$$P_A^i = \mathbf{e}_A^{i\,\mathrm{T}} \left(\mathbf{x}^i - \mathbf{x}_{A,ARP} \right) + c\,\delta t_A - c\,\delta t^i + \lambda\,N_A^i + T_A^i + I_A^i + PCC_A^i + W_A^i + v_A^i \qquad (6.1)$$

where

P_A^i	is the carrier phase observation between antenna A and satellite i,
$\mathbf{e}_A^i$	is the line-of-sight vector,
$\mathbf{x}^i$	is the GNSS satellite position at signal emission,
$\mathbf{x}_{A,ARP}$	is the position of the receiver antenna ARP at signal reception,
c	is the speed of light,
δt_A	is the receiver clock error,
δt^i	is the satellite clock error,
λ	is the carrier wavelength,
N_A^i	is the integer phase ambiguity,
T_A^i	is the tropospheric delay,
I_A^i	is ionospheric delay,
PCC_A^i	is the PCC,
W_A^i	is the phase wind-up and
v_A^i	is zero-difference observation noise.

The phase wind-up is modelled according to Wu et al. (1993). Triple-differences involve eight measurements, as two satellites are observed from two stations at two epochs (Hauschild, 2017b):

$$\begin{aligned} P_{AB,t_1 t_2}^{ij} &= \left(\left(P_B^j - P_A^j \right) - \left(P_B^i - P_A^i \right) \right)_{t_2} - \left(\left(P_B^j - P_A^j \right) - \left(P_B^i - P_A^i \right) \right)_{t_1} \\ &= \left(P_B^j - P_A^j - P_B^i + P_A^i \right)_{t_2} - \left(P_B^j - P_A^j - P_B^i + P_A^i \right)_{t_1} \qquad (6.2) \end{aligned}$$

where $P_{AB,t_1 t_2}^{ij}$ is the triple-difference involving epochs t_1 and t_2. After substitution of Eq. 6.1

into Eq. 6.2 and simplification, the triple-difference reads:

$$
\begin{aligned}
P^{ij}_{AB,t_1t_2} =\ & \left(\rho^{j}_{B,t_2} - \rho^{j}_{A,t_2} - \rho^{i}_{B,t_2} + \rho^{i}_{A,t_2}\right) - \left(\rho^{j}_{B,t_1} - \rho^{j}_{A,t_1} - \rho^{i}_{B,t_1} + \rho^{i}_{A,t_1}\right) \\
& + \left(N^{j}_{B,t_2} - N^{j}_{A,t_2} - N^{i}_{B,t_2} + N^{i}_{A,t_2}\right) - \left(N^{j}_{B,t_1} - N^{j}_{A,t_1} - N^{i}_{B,t_1} + N^{i}_{A,t_1}\right) \\
& + \left(PCC_B(\alpha^{j}_{B,t_2}, z^{j}_{B,t_2}) - PCC_A(\alpha^{j}_{A,t_2}, z^{j}_{A,t_2})\right. \\
& \qquad \left. - PCC_B(\alpha^{i}_{B,t_2}, z^{i}_{B,t_2}) + PCC_A(\alpha^{i}_{A,t_2}, z^{i}_{A,t_2})\right) \\
& - \left(PCC_B(\alpha^{j}_{B,t_1}, z^{j}_{B,t_1}) - PCC_A(\alpha^{j}_{A,t_1}, z^{j}_{A,t_1})\right. \\
& \qquad \left. - PCC_B(\alpha^{i}_{B,t_1}, z^{i}_{B,t_1}) + PCC_A(\alpha^{i}_{A,t_1}, z^{i}_{A,t_1})\right) \\
& + \left(W^{j}_{B,t_2} - W^{j}_{A,t_2} - W^{i}_{B,t_2} + W^{i}_{A,t_2}\right) - \left(W^{j}_{B,t_1} - W^{j}_{A,t_1} - W^{i}_{B,t_1} + W^{i}_{A,t_1}\right) \\
& + v^{ij}_{AB,t_1t_2}
\end{aligned}
\tag{6.3}
$$

where

ρ	is the respective geometrical term,
v^{ij}_{AB,t_1t_2}	is the triple-difference observation noise,
α	is the azimuth of the GNSS satellite and
z	is the zenith angle of a GNSS satellite as seen from the station.

The triple-difference observation noise is $2\sqrt{2}$ times larger than the zero-difference observation noise (assuming that all observations have the same standard deviation and are uncorrelated). Assuming a short baseline, the ionospheric and the tropospheric delays are strongly reduced already on station single-difference level, together with the satellite clock error (Hauschild, 2017b, p. 594). Receiver clock errors vanish at double-difference level (Hauschild, 2017b, p. 597).

Assuming that the interval between the two epochs is very small, further simplifications can be introduced:

   i. In the absence of cycle slips, the ambiguity term is constant in time, thus:

     a. N^{j}_{B,t_1} equals N^{j}_{B,t_2},

     b. N^{j}_{A,t_1} equals N^{j}_{A,t_2},

     c. N^{i}_{B,t_1} equals N^{i}_{B,t_2} and

     d. N^{i}_{A,t_1} equals N^{i}_{A,t_2}.

  ii. Because the reference antenna B does not rotate, its phase wind-up is almost constant over short time intervals. Therefore:

     a. W^{i}_{B,t_1} equals W^{i}_{B,t_2} and

     b. W^{j}_{B,t_1} equals W^{j}_{B,t_2}.

 iii. The apparent positions of the GNSS satellites change very slowly. Therefore:

a. α_{B,t_1}^i equals α_{B,t_2}^i,

b. α_{B,t_1}^j equals α_{B,t_2}^j,

c. z_{B,t_1}^i equals z_{B,t_2}^i and

d. z_{B,t_1}^j equals z_{B,t_2}^j,

practically leading to the elimination of the PCC of the reference antenna.

Introducing these simplifications into Eq. 6.3 leads to the following, final expression:

$$
\begin{aligned}
P_{AB,t_1t_2}^{ij} = \rho_{AB,t_1t_2}^{ij} &- PCC_A(\alpha_{A,t_2}^j, z_{A,t_2}^j) + PCC_A(\alpha_{A,t_2}^i, z_{A,t_2}^i) \\
&- PCC_A(\alpha_{A,t_1}^j, z_{A,t_1}^j) + PCC_A(\alpha_{A,t_1}^i, z_{A,t_1}^i) \\
&- W_{A,t_2}^j + W_{A,t_2}^i - W_{A,t_1}^j + W_{A,t_1}^i + v_{AB,t_1t_2}^{ij}
\end{aligned}
\tag{6.4}
$$

where $\rho_{AB,t_1t_2}^{ij}$ is the triple-difference geometry term. The geometry term can easily be modelled using broadcast or precise satellite orbits and approximate station coordinates. The phase wind-up is modelled according to Wu et al. (1993). Even though the phase wind-up and the PCC of the reference antenna nearly vanish on triple-difference level, the modelled corrections are applied in the processing software.

6.3   Absolute character of triple-difference antenna calibration

The last remaining deterministic signal component in Eq. 6.4 is the PCC. The PCC of the reference antenna has vanished, leading to a truly absolute estimation of PCC. If the reference antenna PCC is still present in the observation equation, the calibration cannot be said to be truly 'absolute' (see also Bilich and Mader, 2010, p. 1371).

This independence on the reference PCC of the triple-differences is illustrated with the help of a use case. A sequence of 4042 orientations and a precise orbit file from 22.8.2018 have been used to generate synthetic observations. Biases were added on the reference station during the data generation process. The data was then processed with double-difference as well as triple-difference algorithms. As can be seen in Table 6.3.1, the triple-difference is much less sensitive to biases like the modelled PCC of the reference antenna. Even a very long calibration sequence of over 4000 orientations is not able to eliminate the bias which is due to the omission of the reference PCC, if double-differences are used. An error of up to 0.3 mm is the consequence. If a five times larger PCC bias is applied, the difference between double-differences and triple-differences becomes more obvious. In this case, the error on the estimated PCC amounts to over 1.5 mm for the double-difference approach, while the triple-difference approach leads to a PCC with only 0.16 mm maximal error.

Table 6.3.1 : Results from a study on PCC biases conducted with synthetic data. Biases were added to the data during the data generation process. During the estimation process, the biases were not modelled. The results show a different sensitivity of the processing based on triple-differences (TD) compared to the processing based on double-differences (DD). In the first case, a PCO bias of 10 cm was added to the reference station. In the second case, the PCC of the 'SEPCHOKE_B3E6 SPKE' antenna (IGS type mean value) was added to the reference station. In the last case, a bias corresponding to five times the PCC of the 'SEPCHOKE_B3E6 SPKE' antenna (IGS type mean value) was added to the reference. The table holds the Root Mean Square error (RMSE), the minimal error (Min.) and the maximal error (Max.) of the estimated PCC.

[mm]		RMSE	Min.	Max.
PCO bias (100 mm)	TD	0.03	-0.09	0.12
	DD	0.03	-0.06	0.15
PCC bias I (80 mm)	TD	0.03	-0.08	0.11
	DD	0.08	-0.32	0.26
PCC bias II (400 mm)	TD	0.03	-0.16	0.08
	DD	0.34	-1.61	1.13

Of course, the pure access to the PCC of the antenna to be calibrated has a cost, namely a higher noise level of triple-differences compared to double-differences. As eight observations are involved in a triple-difference, the standard deviation of one observation is $2\sqrt{2}$ times higher than the standard deviation of a zero-difference observation (in the case of uncorrelated observations with equal weight). Nevertheless, triple-differences should always be preferred if:

i. The goal is to obtain unbiased estimates of the PCC and if

ii. enough measurements are available to reduce the variance of the estimates to a reasonable level.

6.4 Rotation sequence

During the calibration, a point within the antenna, for instance the nominal GPS L1 phase centre, is kept fixed in space. The nominal coordinates of the chosen point do not change during the calibration. A fixed rotation point has following advantages:

i. The dynamics of the antenna is reduced. Therefore, dynamics induced tracking loop responses are reduced and

ii. beside the tilt, the antenna is stationary with respect to its environment. Thus, the change in the multipath pattern is reduced.

The algorithm for the generation of the rotation sequence is displayed in Figure 6.4.1. First, a regular grid in azimuth and elevation is formed. This grid describes in which direction and by which angle the antenna is tilted. This step and all subsequent steps are illustrated in Figure 6.4.2. In a second step, a common rotation is applied to all normal vectors. The goal of this additional rotation is to avoid pointing towards the north hole. In step three, the sequence is randomized. Finally, rotations around the inclined antenna z-axis are added.

The randomisation of the rotation sequence is the key to successful antenna calibration. Randomisation ensures that time correlated effects do not systematically bias the estimation of the PCC. Another key factor is a good mixture between rotations around the antenna z-axis and rotations around the two other axes.

Rotations around the antenna z-axis do not change the orientation of the antenna gain pattern with respect to the site, because the gain pattern of geodetic antennas is typically highly symmetrical. However, rotations around the z-axis do not add information about the zenithal behaviour of the PCC. They strengthen the observability of azimuth variations of the PCC. This is illustrated in Figure 6.4.3. Two or three different rotations of the antenna z-axis for each orientation is a reasonable choice.
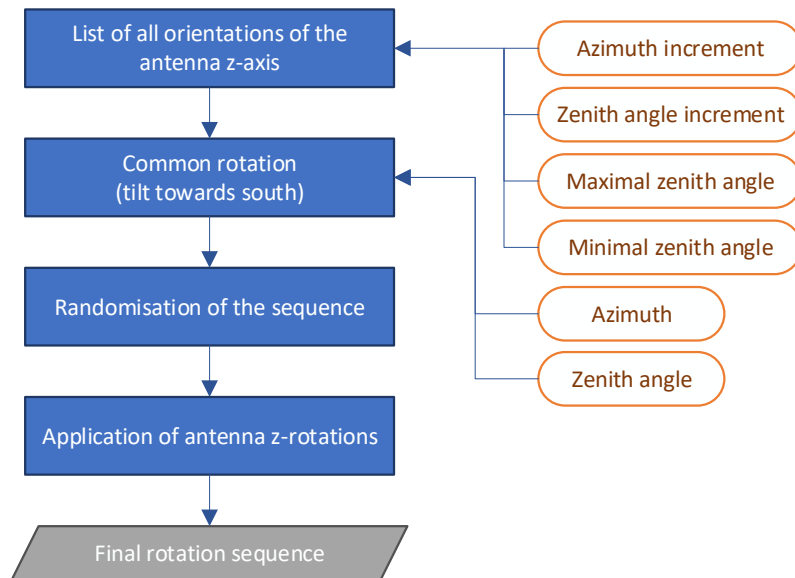
Figure 6.4.1 : Flowchart of the algorithm for the generation of the randomized rotation sequence.
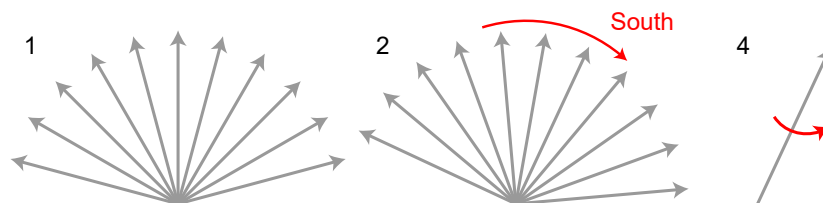

Figure 6.4.2 : Algorithm for the generation of the randomized rotation sequence. In 1, all orientations for the antenna z-axis are set up. In 2, the space of all rotations is tilted towards south, in order to avoid the north-hole. Pointing towards the north-hole unnecessarily reduces the number of observations. In 3 (not shown), the order of the sequence is randomized. Finally, in 4, rotations around the antenna z-axis are added.
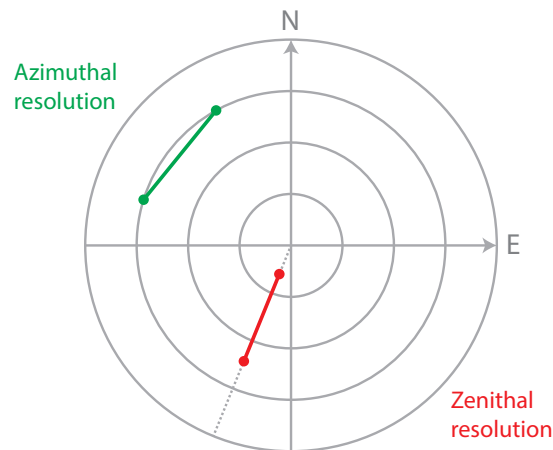
Figure 6.4.3 : Skyplot illustrating azimuthal and zenithal resolution. Azimuthal information is added by rotating the antenna around the antenna z-axis. In this case, only the azimuth satellite changes. Information on the zenithal variability of the PCC is obtained by applying rotations around the antenna x- or y-axis (or both), in order to change the elevation of the GNSS satellite.

6.5 Receiver dynamical stress

As pointed out in Häberling (2015), receiver suffer from dynamical stress in high dynamical situations. The rotation around the nominal phase centre theoretically reduces the dynamics during the change of orientation of the antenna. Only the PCC rate remains. However, the KUKA robot does not perform trajectory control between two stationary positions. In fact, all axes are driven linearly. This might induced a small dynamics. Within the frame of this thesis, receiver dynamical stress was not given particular attention. From the comparisons of the results obtained with various signals on the same frequency, it is obvious that the GPS L2W signals, which are derived from the encrypted P-code, lead to absurd results. These measurements have an inertia of several seconds and can therefore not be used for antenna calibration purposes.[1] More information on the signal structure is found in Teunissen and Montenbruck (2017), more information on GNSS receiver architecure is found in Kaplan and Hegarty (2017).

For most of the calibrations, Septentrio PolaRx 5 receivers with the default setting were used.

---

[1]Personal communication from Septentrio at the ION GNSS+ 2018 conference, 24–28 September 2018, Miami.

6.6   Differencing strategy

Two requirements drive the differencing strategy:

  i. The triple-difference observations should be algebraically uncorrelated. This allows a sequential parameter estimation process (normal equation stacking) and

 ii. the time interval between two epochs being differentiated against each other should be small.

A sequence fulfilling these requirements is displayed in Figure 6.6.1. Half of the measurements taken at orientation k are differentiated against half of the measurements taken at orientation $k+1$. The measurements acquired during the robot motion are discarded. Those measurements can be taken into account, provided that the robot motion is sufficiently well-known between to stationary positions and provided that the dynamics of the robot does not lead to dynamical stress tracking errors.

In case of an odd number of measurement epochs, one epoch is discarded. The number of epochs finally taken into account is dependent on:

  i. The sampling rate of the receiver,

 ii. the duration of the stationary position of the robot and

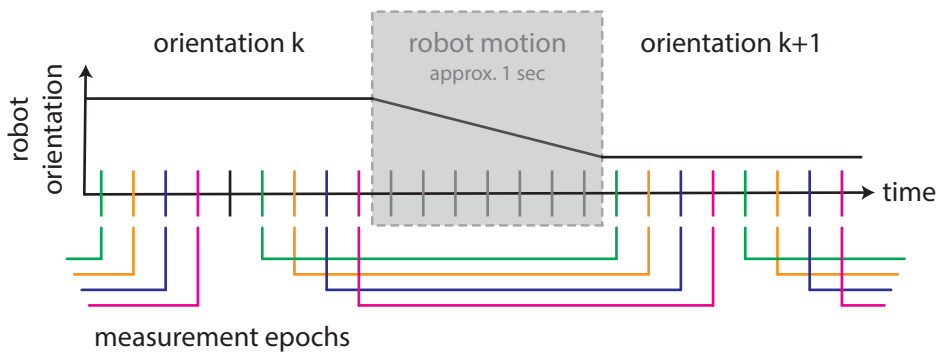iii. the timing accuracy of the robot, which is less accurate than the timing accuracy of the GNSS receivers.

Figure 6.6.1 : Differencing strategy avoiding algebraic correlation between the triple-differences. Source: (Willi et al., 2018a).

6.7 Processing pipeline

A summary of the processing pipeline, which is implemented in Matlab, is presented in Figure 6.7.1. The pipeline uses the following input data:

  i. GNSS observations:

    a. A RINEX observation file from the reference station and

    b. a RINEX observation file from the antenna to be calibrated.

 ii. A file with the start time and the end time of each orientation (robot attitude file),

iii. a configuration file (see Table 6.7.1) and

iv. precise GNSS products:

    a. Precise GNSS orbits,

    b. precise GNSS clocks and

    c. a RINEX navigation file for the ionospheric correction parameters.

The configuration file contains all options for the processing, for instance the signal for which to generate a calibration. Its content is shown in Table 6.7.1. After data reading and automatic download of precise products, a Single Point Positioning (SPP) solution is computed. The Centre for Orbit Determination in Europe (CODE; Prange et al., 2017) is one example for a facility offering precise orbits and clocks.[2] The SPP solution uses the GPS user algorithm from the GPS ICD 200 (2015) and the ionospheric model coefficients from a concatenated RINEX navigation file. This file is available, for instance, at NASA's Crustal Dynamics Data Information System (CCDIS).[3] The main goal of this processing step is to provide a receiver clock estimate with respect to GPS time, which is necessary for the alignment of the measurements.

The alignment part consists of a loop establishing the time correspondence between the GNSS observations from the reference station, the GNSS observations from the antenna to be calibrated and the robot orientations, according to the scheme presented in Section 6.6 and in Figure 6.6.1. The result is a list of simultaneous GNSS observations from both, the reference station and the antenna to be calibrated, labeled with the orientation of the robot at that exact moment.

The actual PCC estimation is achieved in the main computation loop, based on triple-differences generated according to Section 6.2. The observation equation is set up, the derivatives are computed and the normal equation matrix is populated. This operation is performed sequentially and all normal equations are summed up. The inversion of the accumulated normal equations leads to the final estimation of the PCC.

---

[2]`http://ftp.aiub.unibe.ch`

[3]`ftp://cddis.gsfc.nasa.gov/gnss/data/daily`. The daily concatenated navigation files containing the coefficients are named *brdcDOY0.YYn* with DOY being the day of the year and YY being the two digit year.
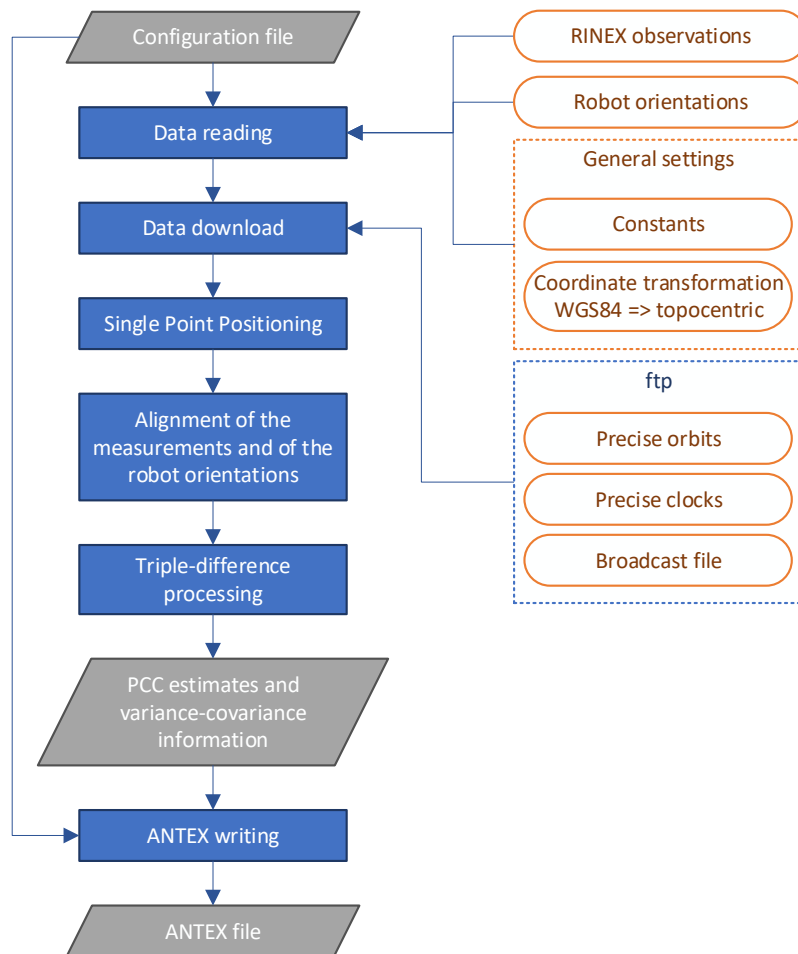
Figure 6.7.1 : Overview of the processing of the GNSS observations for PCC estimation.

Table 6.7.1 : Configuration options for PCC estimation. As suggested by the entry 'Reference PCC', the PCC of the reference antenna are applied, even though they nearly vanish on triple-difference-level.

Option	Description	E.g.
Folder	Path to data folder	
Campaign	Name of the campaign for file naming	
Save path	Path for all result files	
Date	Date of the processing	
RINEX	Input GNSS observation files	
Attitude	Input file of robot orientations	
Type	Type of the antenna to be calibrated	
Serial	Serial number of the antenna	
Offset to ARP	X, Y and Z Offset of the ARP in the robot tool system in mm	
System 1	GNSS used for Single Point Positioning	GPS
Signal 1	Signal used for Single Point Positioning	C1C
System 2	GNSS to be calibrated	Galileo
Signal 2	Signal to be calibrated	L5Q
Pseudorange 2	Pseudorange associated with the above signal	C5Q
Resolution	Degree and order of the spherical harmonics expansion	8
Reference PCC	Path to the ANTEX file of the reference antenna	
Reference type	Type of the reference antenna	
Reference serial	Serial number of the reference antenna	
Robot coordinates	Approximated coordinates (in the topocentric frame) which were kept fix during the calibration	
Reference station coordinates	Approximated coordinates of the reference station	
Coordinate weight	Standard deviation of the reference coordinates in metres. The coordinates are introduced as pseudo-observations	
Elevation mask	Minimum elevation in the topocentric reference frame	
Grid	Optional estimation of PCC with the grid parametrisation	
Grid resolution	Spacing of the grid in azimuth and elevation	
Simulation	Optional simulation ability	

All parameters are originally set up in the normal equation. The singular parameters, for instance the spherical harmonics coefficients representing anti-symmetry (see section 3.4.3) are hard-constrained to zero. The relative coordinates of the antenna to be calibrated (or more accurately, the coordinates of the rotation point) with respect to the reference antenna are introduced as pseudo-observation (soft-constrain). If a spherical harmonics parametrisation is chosen, the PCO is not explicitly set up, as it is implicitly already contained in the spherical harmonics series (see section 3.4.3).

The configuration file is needed a second time in order to generate the ANTEX file. In the case of PCC parametrisation as spherical harmonics, the spherical harmonics are evaluated at a regular spacing (typically 5 degrees). The best-fit PCO is estimated and subtracted from the grid. The resulting grid is written into the ANTEX file instead of spherical harmonics coefficients, as ANTEX does not support a spherical harmonics representation. If necessary for conventional reasons, a best-fit PCO can be estimated and subtracted from the PCV before the ANTEX file is written.

6.8 Outlook

The future effort will focus on further validation. The implementation of Frequency Division Multiple Access Signals (FDMA) is foreseen as well.

Multipath will remain a big challenge. Software Defined Radio (SDR) GNSS receivers (also called software receivers) are a very efficient way of quantifying and mitigating multipath propagation errors. Efforts should be put in utilizing SDR GNSS receivers for GNSS antenna calibration. SDR GNSS receivers allow to investigate dynamical stress errors and multipath on the receiver tracking loop level. This is the key for an efficient quantification and mitigation of multipath.

Chapter 7

Conclusions and outlook

This work initially dealt with the attitude onboard a spacecraft with baselines of less than 10 cm. In a first step, the synchronisation of the receivers on a software level was investigated. The result is an algorithm for the extrapolation of the measurements, which was published in GPS Solutions (Willi and Rothacher, 2017). The algorithm was validated with a synthetic data study and a signal simulator study.

The insights from the first studies led to further investigations on the Phase Centre Corrections (PCC) of antennas in the vicinity of each other. A relative field calibration was set up. It allowed to calibrate a model of the CubETH satellite and a GNSS attitude determination platform with low-cost geodetic antennas at 15 cm distance from each other. The final results were published in the ION GNSS proceedings 2017 (Willi et al., 2017) and in Navigation (Willi et al., 2018b). They included a synthetic data study and a validation with real data. We showed that the correction of the PCC is of tremendous importance on short baselines. Furthermore, we demonstrated that mutual coupling affects antennas and that this effect must be taken into account when performing PCC estimation.

Although the relative field calibration was suited to calibrate the GNSS attitude determination system, it has fundamental weaknesses. These weaknesses could be mitigated by focusing on absolute GNSS antenna calibration. Within a short time, an operational, absolute field calibration system for GNSS antennas was developed from scratch. This includes the commissioning and the calibration of the industrial KUKA robot, which is documented in Willi and Guillaume (2019).

Preliminary results obtained with the new calibration system were presented at the ION GNSS+ 2018 (Willi et al., 2018a). The system obtained the attention of the international community at the IGS Workshop 2018 in Wuhan, China, as being the first absolute field calibration system able to produce calibrations for the new Galileo signals.

The need for high-accuracy, multi-GNSS antenna calibration is going to increase in the future. Properly calibrated antennas are a central element of permanent station networks. The full strength of a multi-GNSS processing can only be exploited, if multi-GNSS antenna calibrations are available for ground antennas. Eventually, calibrated GNSS antennas will help to better

quantify and assess socially relevant changes in the environment, as see level rise.

The need for calibrated low-cost antennas might rapidly increase as well. The 21th century is already marked by the automation of transportation. Autonomous cars are the most prominent example. GNSS will be one of the technologies used for the positioning of autonomous vehicles. Due to significant advances in kinematic positioning, Phase Centre Corrections (PCC) of GNSS antennas already tend to become the limiting factor in low-cost GNSS positioning.

Finally, well-calibrated antennas might be a key to further advances in Precise Point Positioning (PPP). A remarkable progress was achieved in the convergence time of PPP and in PPP ambiguity resolution. PPP will sooner or later run into limitations due to the PCC of the receiver antenna. Here again, precise muti-GNSS and multi-frequency calibrations will help to reach the accuracy, which is inherent to PPP.

Bibliography

REMARK: if not stated otherwise, the links in the bibliography were checked on 12 December 2018.

Aghili F and Salerno A (2013) Driftless 3-D Attitude Determination and Positioning of Mobile Robots By Integration of IMU With Two RTK GPSs. *IEEE/ASME Transactions on Mechatronics*, 18(1):21–31. URL `https://doi.org/10.1109/TMECH.2011.2161485`.

Allman M, Novotny D and Gordon J (2018) Calibration of a 6-Axis Serial Robotic Arm Mounted to a Moveable Base at the National Institute of Standards and Technology. In *Proceedings of the 35th Annual Coordinate Metrology Society Conference 2018*, p. 12. Orlando, FL, USA.

Arbinger C and Enderle W (2000) Spacecraft Attitude Determination using a Combination of GPS Attitude Sensor and Star Sensor Measurements. In *Proceedings of the 13th International Technical Meeting of the Satellite Division of The Institute of Navigation (ION GPS 2000)*, pp. 2634–2642. Salt Lake City, UT, USA. URL `https://www.ion.org/publications/abstract.cfm?articleID=1692`.

Bilich A and Mader GL (2010) GNSS absolute antenna calibration at the nationalgeodetic survey. In *Proceedings of the 23rd International Technical Meeting of The Satellite Division of the Institute of Navigation (ION GNSS 2010)*, pp. 1369 –1377. Portland, OR, USA. URL `https://www.ion.org/publications/abstract.cfm?articleID=9251`.

Bilich A, Schmitz M, Görres B, Zeimetz P, Mader G and Wübbena G (2012) Three-method absolute antenna calibration comparison (oral presentation). In *IGS Workshop 2012*. Olsztyn, Poland. URL `http://www.igs.org/assets/video/Poland%202012%20-%20P09%20Bilich%20PR59.mp4`.

Bilich A, Erickson B and Geoghegan C (2018) 6-axis robot for absolute antenna calibration at the US National Geodetic Survey (poster). In *IGS Workshop 2018*. Wuhan, Hubei, China.

Braasch MS (2017) Multipath. In Teunissen PJG and Montenbruck O (eds.) *Springer Handbook of Global Navigation Satellite Systems*, pp. 443–468. Springer International Publishing, Cham, Germany. ISBN 978-3-319-42928-1. URL `https://doi.org/10.1007/978-3-319-42928-1_15`.

Brandstötter M, Angerer A and Hofbaur M (2014) An analytical solution of the inverse kinematics problem of industrial serial manipulators with an ortho-parallel basis and a spherical wrist (Revised Version). In *Proceedings of the Austrian Robotics Workshop 2014*, pp. 7–11. Linz, Austria.

Cannon ME and Sun H (1996) Experimental assessment of a non-dedicated GPS receiver system for airborne attitude determination. *ISPRS Journal of Photogrammetry and Remote Sensing*, 51(2):99–108. URL `https://doi.org/10.1016/0924-2716(69)00011-6`.

Chen W and Qin H (2012) New method for single epoch, single frequency land vehicle attitude determination using low-end GPS receiver. *GPS Solutions*, 16(3):329–338. URL `https://doi.org/10.1007/s10291-011-0234-8`.

Cohen CE (1992) *Attitude Determination Using GPS, Development of an All Solid-State Guidance, Navigation, and Control Sensor for Air and Space Vehicles Based on the Global Positioning System*. Doctoral Thesis, Stanford University, Stanford, CA, USA. URL `https://web.stanford.edu/group/scpnt/gpslab/pubs/theses/ClarkCohenThesis92.pdf`.

Cohen CE, Lightsey EG, Parkinson BW and Feess WA (1994) Space flight tests of attitude determination using GPS. *International Journal of Satellite Communications*, 12(5):427–433. URL `https://doi.org/10.1002/sat.4600120504`.

Corke P (2017) Robot Arm Kinematics. In *Robotics, Vision and Control*, vol. 118 of *Springer Tracts in Advanced Robotics*, pp. 193–228. Springer International Publishing, Cham. ISBN 978-3-319-54413-7. URL `https://doi.org/10.1007/978-3-319-54413-7_7`.

Counselman CC and Shapiro II (1979) Miniature interferometer terminals for earth surveying. *Bulletin Géodésique*, 53(2):139–163. URL `https://doi.org/10.1007/BF02521086`.

Dach R, Lutz S, Walser P and Fridez P (eds.) (2015) *Bernese GNSS Software Version 5.2*. Astronomical Institute, University of Bern, Bern, Switzerland. URL `https://doi.org/10.7892/boris.72297`.

Diebel J (2006) Representing attitude: Euler angles, unit quaternions, and rotation vectors. *Tech. rep.*, Stanford University, Stanford, CA, USA.

Dilßner F (2008) *Zum Einfluss des Antennenumfeldes auf die hochpräzise GNSS-Positionsbestimmung*. Doctoral Thesis, Leibniz University Hanover, Hanover, Germany. URL `https://www.tib.eu/de/suchen/id/TIBKAT%3A583144810/Zum-Einfluss-des-Antennenumfeldes-auf-die-hochpr%C3%A4zise/`.

Farrell JL, Stuelpnagel JC, Wessner RH, Velman JR and Brook JE (1966) A least squares estimate of satellite attitude (Grace Wahba). *Siam Review*, 8(3):384–386. URL `https://doi.org/10.1137/1008080`.

Geiger A (1988) Modeling of Phase Center Variation and its Influence on GPS-Positioning. In Groten E and Strauss R (eds.) *GPS-Techniques Applied to Geodesy and Surveying*, pp. 210–222. Springer Berlin Heidelberg, Berlin, Heidelberg. ISBN 978-3-540-45962-0. URL `https://doi.org/10.1007/BFb0011339`.

Geiger A (1990) Influence of Phase Center Variations on the Combination of different Antenna Types. In *Proceedings of the Second International Symposium on Precise Positioning with the Global Positioning System*, pp. 466–476. The Canadian Institute of Surveying and Mapping, Ottawa, Canada. ISBN 0-919088-40-6.

Giorgi G (2017) Attitude Determination. In Teunissen PJG and Montenbruck O (eds.) *Springer Handbook of Global Navigation Satellite Systems*, pp. 781–809. Springer International Publishing, Cham, Germany. ISBN 978-3-319-42928-1. URL `https://doi.org/10.1007/978-3-319-42928-1_27`.

Giorgi G, Teunissen PJG and Gourlay TP (2012) Instantaneous Global Navigation Satellite System (GNSS)-Based Attitude Determination for Maritime Applications. *IEEE Journal of Oceanic Engineering*, 37(3):348–362. URL `https://doi.org/10.1109/JOE.2012.2191996`.

Görres B, Campbell J, Becker M and Siemes M (2006) Absolute calibration of GPS antennas: laboratory results and comparison with field and robot techniques. *GPS Solutions*, 10(2):136–145. URL `https://doi.org/10.1007/s10291-005-0015-3`.

Görres B, Kersten T, Schön S, Zimmermann F and Wanninger L (2018) Berücksichtigung von Antennenkorrekturen bei GNSS-Anwendungen. *DVW-Merkblatt 1-2018*, Gesellschaft für Geodäsie, Geoinformation und Landmanagement e.V., Bühlertal, Germany. URL `https://www.dvw.de/sites/default/files/news_termine/dateianhang/2018/01_DVW-Merkblatt_Antennenkorrekturen-GNSS_2018.pdf`.

Häberling S (2015) *Theoretical and practical aspects of high-rate GNSS geodetic observations*. Doctoral Thesis, ETH Zurich, Zurich, Switzerland. URL `https://doi.org/10.3929/ethz-a-010592866`.

Hauschild A (2017a) Basic Observation Equations. In Teunissen PJG and Montenbruck O (eds.) *Springer Handbook of Global Navigation Satellite Systems*, pp. 561–582. Springer International Publishing, Cham, Germany. ISBN 978-3-319-42928-1. URL `https://doi.org/10.1007/978-3-319-42928-1_19`.

Hauschild A (2017b) Combinations of Observations. In Teunissen PJG and Montenbruck O (eds.) *Springer Handbook of Global Navigation Satellite Systems*, pp. 583–604. Springer International Publishing, Cham, Germany. ISBN 978-3-319-42928-1. URL `https://doi.org/10.1007/978-3-319-42928-1_20`.

Hollenstein C, Männel B, Serantoni E, Scherer L, Rothacher M, Kehl P and Ivanov A (2014) Concepts and Testing of Low-cost GNSS Receivers for CubeSat Orbit and Attitude Determination. In *Proceedings of the 7th European Navigation Conference (navitec 2014)*. Noordwijk, Netherlands.

Hollerbach J, Khalil W and Gautier M (2016) Model Identification. In Siciliano B and Khatib O (eds.) *Springer Handbook of Robotics*, pp. 113–138. Springer International Publishing, Cham. ISBN 978-3-319-32552-1. URL `https://doi.org/10.1007/978-3-319-32552-1_6`.

Hu Z, Zhao Q, Chen G, Wang G, Dai Z and Li T (2015) First Results of Field Absolute Calibration of the GPS Receiver Antenna at Wuhan University. *Sensors*, 15(11):28717–28731. URL `https://doi.org/10.3390/s151128717`.

IS-GPS-200 (2015) Global Positioning Systems Directorate, Systems Engineering & Integration Interface Specification IS-GPS-200. *Tech. rep.*, Global Positioning Systems Directorate, United States Air Force, USA. URL `https://www.gps.gov/technical/icwg/IRN-IS-200H-001+002+003_rollup.pdf`.

Jekeli C (2001) Coordinate Frames and Transformations. In *Inertial Navigation Systems with Geodetic Applications*. Walter de Gruyter, Berlin, Germany. ISBN 978-3-11-080023-4. URL `https://doi.org/10.1515/9783110800234.1`.

Kallio U, Koivula H, Lahtinen S, Nikkonen V and Poutanen M (2018) Validating and comparing GNSS antenna calibrations. *Journal of Geodesy*. URL `https://doi.org/10.1007/s00190-018-1134-2`.

Kaplan ED and Hegarty C (eds.) (2017) *Understanding GPS/GNSS: principles and applications*. GNSS Technology and Applications Series. Artech House, Boston, MA, USA, third edn. ISBN 978-1-63081-058-0.

Kersten T (2014) *Bestimmung von Codephasen-Variationen bei GNSS-Empfangsantennen und deren Einfluss auf Positionierung, Navigation und Zeitübertragung*. Doctoral Thesis, Leibniz University Hanover, Hanover, Germany. URL `https://doi.org/10.15488/4003`.

Kim D and Langley RB (2007) GPS RTK-based attitude determination for the e-POP platform onboard the Canadian CASSIOPE spacecraft in low earth orbit. In *Time Nav'07 (ENC GNSS 2007)*. Geneva, Switzerland.

Kuka (2018) KUKA KR AGILUS sixx Specification. *Tech. rep.*, KUKA Deutschland GmbH, Augsburg, Germany.

Maqsood M, Gao S and Montenbruck O (2017) Antennas. In Teunissen PJG and Montenbruck O (eds.) *Springer Handbook of Global Navigation Satellite Systems*, pp. 505–534. Springer

International Publishing, Cham, Germany. ISBN 978-3-319-42928-1. URL `https://doi.org/10.1007/978-3-319-42928-1_17`.

Menge F (2003) *Zur Kalibrierung der Phasenzentrumsvariationen von GPS Antennen für die hochpräzise Positionsbestimmung.* Doctoral Thesis, Leibniz University Hanover, Hanover, Germany. URL `https://www.tib.eu/de/suchen/id/TIBKAT%3A381885593/Zur-Kalibrierung-der-Phasenzentrumsvariationen/`.

Motta J (2006) Robot Calibration: Modeling Measurement and Applications. In Kin-Huat L (ed.) *Industrial Robotics: Programming, Simulation and Applications.* IntechOpen Limited, London, UK. ISBN 3-86611-286-6. URL `https://doi.org/10.5772/4894`.

Nadarajah N, Teunissen PJG and Buist PJ (2012) Attitude determination of LEO satellites using an array of GNSS sensors. In *15th International Conference on Information Fusion*, pp. 1066–1072. IEEE, Singapore, Singapore. ISBN 978-0-9824438-4-2. URL `http://ieeexplore.ieee.org/xpls/abs_all.jsp?arnumber=6289927`.

Nubiola A and Bonev IA (2013) Absolute calibration of an ABB IRB 1600 robot using a laser tracker. *Robotics and Computer-Integrated Manufacturing*, 29(1):236–245. URL `https://doi.org/10.1016/j.rcim.2012.06.004`.

Park C and Teunissen PJG (2003) A new carrier phase ambiguity estimation for GNSS attitude determination systems. In *Proceedings of international GPS/GNSS symposium.* Tokyo, Japan. URL `https://gnss.curtin.edu.au/wp-content/uploads/sites/21/2016/04/Park2003new.pdf`.

Petit G and Luzum B (eds.) (2010) *IERS Conventions*, vol. 36 of *IERS Technical Note.* Verlag des Bundesamts für Kartographie und Geodäsie, Frankfurt am Main, Germany. URL `http://www.iers.org/TN36`.

Prange L, Orliac E, Dach R, Arnold D, Beutler G, Schaer S and Jäggi A (2017) CODE's five-system orbit and clock solution—the challenges of multi-GNSS data analysis. *Journal of Geodesy*, 91(4):345–360. URL `https://doi.org/10.1007/s00190-016-0968-8`.

Rao BR, Kunysz W, Fante R and McDonald K (2013) *GPS/GNSS antennas.* GNSS technology and applications series. Artech House, Boston, MA, USA. ISBN 978-1-59693-150-3.

Riddell A, Moore M and Hu G (2015) Geoscience Australia's GNSS antenna calibration facility: Initial results. In *Proceedings of IGNSS Symposium 2015 (IGNSS2015).* Surfers Paradise, QLD, Australia.

RINEX Working Group and RTCM-SC104 (2015) RINEX, The Receiver Independent Exchange Format, Version 3.03. *Tech. rep.*, International GNSS Service (IGS) and Radio Technical

Commission for Maritime Services Special Committee 104 (RTCM-SC104), Pasadena, CA, USA. URL `ftp://igs.org/pub/data/format/rinex303.pdf`.

Rothacher M (2001) Comparison of absolute and relative antenna phase center variations. *GPS solutions*, 4(4):55–60. URL `https://doi.org/10.1007/PL00012867`.

Rothacher M and Schmid R (2010) ANTEX: The antenna exchange format version 1.4. *Tech. rep.*, International GNSS Service, Pasadena, CA, USA. URL `ftp://igs.org/pub/station/general/antex14.txt`.

Rothacher M, Schaer S, Mervart L and Beutler G (1995) Determination of antenna phase center variations using GPS data. In Gendt G and Dick G (eds.) *Special Topics and New Directions, Workshop Proceedings. IGS Workshop*, pp. 205–220. Potsdam, Germany.

Sabatini R, Rodríguez L, Kaharkar A, Bartel C and Shaid T (2012) Carrier-phase GNSS attitude determination and control system for unmanned aerial vehicle applications. *ARPN Journal of Systems and Software*, 2(11):297–322. ISSN 2222-9833.

Schmitz M, Wübbena G and Boettcher G (2002) Tests of phase center variations of various GPS antennas, and some results. *GPS Solutions*, 6(1-2):18–27. URL `https://doi.org/10.1007/s10291-002-0008-4`.

Schröer K (1999) Precision and Calibration. In Nof SY (ed.) *Handbook of Industrial Robotics*, pp. 795–810. John Wiley & Sons, Inc., Hoboken, NJ, USA. ISBN 978-0-470-17250-6. URL `https://doi.org/10.1002/9780470172506.ch39`.

Schröer K, Albright SL and Grethlein M (1997) Complete, minimal and model-continuous kinematic models for robot calibration. *Robotics and Computer-Integrated Manufacturing*, 13(1):73–85. URL `https://doi.org/10.1016/S0736-5845(96)00025-7`.

Schupler BR, Allshouse RL and Clark TA (1994) Signal characteristics of GPS user antennas. *Navigation*, 41(3):276–296. URL `https://doi.org/10.1002/j.2161-4296.1994.tb01881.x`.

Sims ML (1985) Phase center variation in the geodetic TI4100 GPS receiver system's conical spiral antenna. In *Proceedings of the first International Symposium on Precise Positioning with the Global Positioning System*, pp. 227–244. Rockville, MD, US.

Teunissen PJG (1995) The least-squares ambiguity decorrelation adjustment: a method for fast GPS integer ambiguity estimation. *Journal of Geodesy*, 70(1-2):65–82. URL `https://doi.org/10.1007/BF00863419`.

Teunissen PJG (2010) Integer least-squares theory for the GNSS compass. *Journal of Geodesy*, 84(7):433–447. URL `https://doi.org/10.1007/s00190-010-0380-8`.

Teunissen PJG (2017) Carrier Phase Integer Ambiguity Resolution. In Teunissen PJG and Montenbruck O (eds.) *Springer Handbook of Global Navigation Satellite Systems*, pp. 661–685. Springer International Publishing, Cham, Germany. ISBN 978-3-319-42928-1. URL `https://doi.org/10.1007/978-3-319-42928-1_23`.

Teunissen PJG and Montenbruck O (eds.) (2017) *Springer Handbook of Global Navigation Satellite Systems.* Springer International Publishing, Cham, Germany. ISBN 978-3-319-42928-1. URL `https://doi.org/10.1007/978-3-319-42928-1`.

Teunissen PJG, Giorgi G and Buist PJ (2011) Testing of a new single-frequency GNSS carrier phase attitude determination method: land, ship and aircraft experiments. *GPS Solutions*, 15(1):15–28. URL `https://doi.org/10.1007/s10291-010-0164-x`.

Tranquilla JM and Colpitts BG (1989) GPS Antenna Design Characteristics for High-Precision Applications. *Journal of Surveying Engineering*, 115(1):2–14. URL `https://doi.org/10.1061/(ASCE)0733-9453(1989)115:1(2)`.

u-blox (2014) u-blox M8 Receiver Description. *Tech. rep.*, u-blox AG, Thalwil, Switzerland.

Um J and Lightsey EG (2001) GPS Attitude Determination for the SOAR Experiment. *Navigation*, 48(3):180–194. URL `https://doi.org/10.1002/j.2161-4296.2001.tb00241.x`.

Van Graas F and Braasch M (1991) GPS Interferometric Attitude and Heading Determination: Initial Flight Test Results. *Navigation*, 38(4):297–316. URL `https://doi.org/10.1002/j.2161-4296.1991.tb01864.x`.

Welch G and Bishop G (2006) An Introduction to the Kalman Filter. 2006. *Tech. rep.*, University of North Carolina, Chapel Hill, NC, USA.

Willi D and Guillaume S (2019) Calibration of a Six-Axis Robot for GNSS Antenna Phase Center Estimation. *Journal of Surveying Engineering*. ISSN 1943-5428. In review.

Willi D and Rothacher M (2017) GNSS attitude determination with non-synchronized receivers and short baselines onboard a spacecraft. *GPS Solutions*, 21(4):1605–1617. URL `https://doi.org/10.1007/s10291-017-0639-0`.

Willi D, Meindl M, Xu H and Rothacher M (2017) GNSS Antenna Phase Center Variation Calibration for Attitude Determination on Short Baselines. In *30th International Technical Meeting of The Satellite Division of the Institute of Navigation (ION GNSS+ 2017)*, pp. 3997–4010. Portland, OR, USA. URL `https://www.ion.org/publications/abstract.cfm?articleID=15411`.

Willi D, Koch D, Meindl M and Rothacher M (2018a) Absolute GNSS Antenna Phase Center Calibration with a Robot. In *Proceedings of the 31st International Technical Meeting*

of The Satellite Division of the Institute of Navigation (ION GNSS+ 2018), pp. 3909 – 3926. Miami, FL, USA. URL `https://www.ion.org/publications/abstract.cfm?articleID=16040`.

Willi D, Meindl M, Xu H and Rothacher M (2018b) GNSS Antenna Phase Center Variation Calibration for Attitude Determination on Short Baselines. *Navigation*. URL `https://doi.org/10.1002/navi.273`.

Wu J, Wu S, Hajj G, Bertiger W and Lichten S (1993) Effects of antenna orientation on GPS carrier phase. *Manuscripta geodaetica*, 18:91–98.

Wübbena G, Schmitz M, Menge F, Seeber G and Völksen C (1997) A New Approach for Field Calibration of Absolute GPS Antenna Phase Center Variations. *Navigation*, 44(2):247–255. URL `https://doi.org/10.1002/j.2161-4296.1997.tb02346.x`.

Wübbena G, Schmitz M, Menge F, Böder V and Seeber G (2000) Automated absolute field calibration of GPS antennas in real-time. In *Proceedings of the 13th International Technical Meeting of the Satellite Division of The Institute of Navigation (ION GPS 2000)*, pp. 2512–2522. Salt Lake City, UT, USA. URL `https://www.ion.org/publications/abstract.cfm?articleID=1675`.

Wübbena G, Schmitz M and Boettcher G (2003) Analyse umfangreicher Messreihen von GPS Antennen PCV aus absoluten Roboter-Feldkalibrierungen seit Januar 2000 (oral presentation). In *5th GPS Antenna Workshop*. Frankfurt am Main, Germany.

Wübbena G, Schmitz M, Boettcher G and Schumann C (2006) Absolute GNSS antenna calibration with a robot: repeatability of phase variations, calibration of GLONASS and determination of carrier-to-noise pattern (oral presentation). In Springer T, Gendt G and Dow J (eds.) *The International GNSS Service (IGS): Perspectives and Visions for 2010 and Beyond. Proceedings of the IGS Workshop 2006*. Darmstadt, Germany. URL `ftp://igs.org/pub/resource/pubs/06_darmstadt/IGS%20Presentations%20PDF/10_1_Schmitz.pdf`.

Zeimetz P (2010) *Zur Entwicklung und Bewertung der absoluten GNSS-Antennenkalibrierung im HF-Labor*. Doctoral Thesis, University Bonn, Bonn, Germany. URL `hss.ulb.uni-bonn.de/2010/2212/2212.pdf`.

Zeimetz P and Kuhlmann H (2008) On the accuracy of absolute GNSS antenna calibration and the conception of a new anechoic chamber. In *Proceedings of the FIG Working Week 2008*. Stockholm, Sweden. URL `http://fig.net/resources/proceedings/fig_proceedings/fig2008/papers/ts05g/ts05g_01_zeimetz_kuhlmann_2901.pdf`.

Zhang J, Zhang K, Grenfell R and Deakin R (2006) GPS Satellite Velocity and Acceleration Determination using the Broadcast Ephemeris. *Journal of Navigation*, 59(02):293. URL `https://doi.org/10.1017/S0373463306003638`.

Ziebart M and Cross P (2003) LEO GPS attitude determination algorithm for a micro-satellite using boom-arm deployed antennas. *GPS Solutions*, 6(4):242–256. URL `https://doi.org/10.1007/s10291-002-0023-5`.